Prototype development for a new readout of the CB/A2 setup and Analysis of the relative branching fraction of the $\eta' \to \omega\gamma$ decay

Dissertation
zur Erlangung des Grades
„Doktor der Naturwissenschaften“

am Fachbereich Physik, Mathematik und Informatik
der Johanndes Gutenberg-Universität
in Mainz

Andreas Neiser
geboren in Boppard

Mainz, August 2017

Erster Berichterstatter:

Zweiter Berichterstatter:

Datum der mündlichen Prüfung: 9. November 2018

Abstract

The A2 collaboration at the electron accelerator MAMI in Mainz uses an energy-tagged photon beam to produce light mesons off the nucleon to study quantum chromodynamics, the underlying theory of the strong interaction, in the low-energy regime below 1 GeV. The A2 detector system mainly consists of the 4π calorimeter Crystal Ball (CB) and the TAPS calorimeter in forward direction, which are ideally suited to detect final state photons in the given energy range. In 2014, three dedicated beam-times for the production of η' mesons off unpolarized protons yielded a data sample of $(5.12 \pm 0.19) \times 10^6$ η' mesons within an incident photon energy range of $E_\gamma = 1.42 \ldots 1.58\,\mathrm{GeV}$.

This thesis consists of two parts: First, the prototype development to assess possible upgrades of the existing data acquisition system and, second, the analysis of the branching fraction of the decay $\eta' \to \omega\gamma$ relative to the reference channel $\eta' \to \gamma\gamma$. To achieve the results, numerous improvements and innovations related to deployed hardware and software were developed and implemented.

The prototype development for the CB/A2 experiment setup is based on the GSI TRB3 platform, primarily consisting of a multi-purpose $4 + 1$ FPGA printed circuit board. In this thesis, a feature extraction firmware for an already existing sampling analog-to-digital converter extension board is developed and successfully tested at the CB calorimeter, showing a sufficiently precise time and energy measurement at the limit of the given analog signal quality. Additionally, the applicability of a charge-to-time conversion front-end is investigated for other components of the A2 detector system.

The pseudoscalar-vector-gamma decay $\eta' \to \omega\gamma$ serves as an input to effective field theories of the strong interaction, in particular concerning η-η'-mixing and the consistent inclusion of vector mesons. In this thesis, a new analysis framework has been developed providing advanced calibration and tuning methods including kinematic fitting for photo-production experiments. The final result $\mathrm{BR}(\eta' \to \omega\gamma) = (1.82 \pm 0.19_{\mathrm{stat}}) \times 10^{-2}$ is inconsistent with the current PDG world average at $4.3\sigma_{\mathrm{stat}}$. Systematic studies for this deviation are discussed and future work is outlined.

Kurzzusammenfassung

Die A2 Kollaboration am Elektronenbeschleuniger MAMI in Mainz nutzt einen energiemarkierten Photonenstrahl zur Produktion leichter Mesonen an Nukleonen, um die Theorie der starken Wechselwirkung, genannt Quantenchromodynamik, im Niedrigenergiebereich unterhalb von 1 GeV zu untersuchen. Das A2 Detektorsystem besteht hauptsächlich aus dem 4π Kalorimeter Crystal Ball (CB) und dem TAPS Kalorimeter in Vorwärtsrichtung, die ideal dazu geeignet sind, Photonen im gegebenen Energiebereich zu detektieren. Im Jahr 2014 lieferten drei dedizierte Strahlzeiten für die Produktion von η' Mesonen an unpolarisierten Protonen einen Datensatz von $(5.12 \pm 0.19) \times 10^6$ η' Mesonen im Energiebereich von $E_\gamma = 1.42 \ldots 1.58\,\mathrm{GeV}$ der eingehenden Photonen.

Diese Arbeit besteht aus zwei Teilen: Erstens, eine Prototypentwicklung um mögliche Verbesserungen der existierenden Datenerfassung zu beurteilen und, zweitens, die Analyse des Verzweigungsverhältnisses des Zerfalls $\eta' \to \omega\gamma$ relativ zum Referenzkanal $\eta' \to \gamma\gamma$. Um diese Ergebnisse zu erhalten, wurden zahlreiche Verbesserungen und Innovationen im Zusammenhang mit der eingesetzten Hardware und Software entwickelt und umgesetzt.

Die Protoypentwicklung für den CB/A2 Experimentaufbau basiert auf der GSI TRB3 Plattform, die im Wesentlichen aus einer vielseitig einsetzbaren $4 + 1$ FPGA Elektronikplatine besteht. In dieser Arbeit wurde eine Firmware zur Merkmalextraktion für eine bereits existierende Erweiterungsplatine mit einem abtastenden Analog-Digital-Umsetzer entwickelt und erfolgreich am CB Kalorimeter getestet. Es wurde eine ausreichende Energie- und Zeitauflösung begrenzt durch die vorgegebene Analogsignalqualität bestimmt. Zusätzlich wurde die Anwendbarkeit einer weiteren Ladungs-Zeit-Umsetzer-Vorplatine auch für andere Teile des A2 Detektorsystems untersucht.

Der Pseudoskalar-Vektor-Gamma-Zerfall $\eta' \to \omega\gamma$ dient als Test von effektiven Feldtheorien der starken Wechselwirkung, insbesondere die η-η'-Mischung und die konsistente Integration von Vektormesonen betreffend. In dieser Arbeit wurde eine neue Analyseumgebung entwickelt, die fortschrittliche Kalibrations- und Feinabstimmungsmethoden sowie kinematisches Fitten für Photoproduktionsexperimente bereitstellt. Das Endergebnis $\mathrm{BR}(\eta' \to \omega\gamma) = (1.82 \pm 0.19_{\mathrm{stat}}) \times 10^{-2}$ ist um $4.3\sigma_{\mathrm{stat}}$ inkonsistent mit dem aktuellen weltweiten Durchschnitt laut PDG. Systematische Studien für diese Abweichung werden diskutiert und zukünftige Arbeiten werden dargestellt.

Contents

List of Figures

List of Tables

1. Introduction

1.1. Motivation and overview

The strong interaction is one of the four fundamental forces in physics, besides gravitation, electromagnetism and the weak interaction. A huge spectrum of strongly interacting particles has been discovered since the 1950s in cosmic rays and at accelerator facilities all over the world. The properties of those unstable particles are mainly determined by the investigation of their decay into stable particles, for example, photons, electrons or protons, allowing the reconstruction of Lorentz-invariant quantities. To this end, detectors and read-out systems are built to measure the kinetic energy, momentum and the direction of flight, possibly including particle type identification. This modern era of experimental particle physics began in 1952 with the invention of the bubble chamber [1] as an improvement of the cloud chamber, and the most recent highlight was reached with the detection of the Higgs boson in 2012 measured with state-of-the-art detector systems consisting of many million channels [2, 3]. Over this timespan, particle accelerator technology increased the maximum available energies from MeV to TeV and integrated luminosities from 1/μb to 1/fb, both improvements of many orders of magnitude. Detector technology advanced accordingly to distinguish interesting reactions from already known backgrounds with segmented calorimeters and particle tracking on the micrometer scale inside magnetic fields of a few Teslas. Moreover, computer technology crucially supported the recording and subsequent analysis of huge amounts of event data. Thus, experimental particle physics and, on the other side, technology and society mutually benefit from efforts to answer fundamental questions about nature, such as what is matter made of.

Nowadays, the strong interaction is excellently described by quantum chromodynamics (QCD), establishing quarks as the elementary constituents and gluons as force carriers. However, those degrees of freedom do not exist freely in nature due to the so-called confinement, but only their complex bound states are observed, such as protons or pions. Furthermore, QCD in the low-energy regime can neither be solved analytically nor perturbatively, but only ab-initio numerical approaches on the lattice or chiral effective field theories are available. A perturbative treatment of QCD becomes feasible for energies beyond

a few GeV owing to the decreasing coupling constant of the strong interaction, a phenomenon called asymptotic freedom. Despite those complex features, the underlying symmetries of the theory help to organize qualitatively the rich "particle zoo" as observed today and even have led to the prediction and subsequent discovery of missing particles to complete the expected symmetry-degenerate multiplets. The correct description of experimental observations by QCD with sub-percent precision is still a current topic of research, which is presented in greater detail in section 1.2.

Photo-production experiments with bremsstrahlung from an electron beam were first conducted in the early 1950s [4], but became valuable for nuclear and particle physics only after the construction of reliable and high energy electron accelerators, such as the Mainzer Mikrotron (MAMI). A photon beam represents a well-defined quantum state of point-like particles interacting electromagnetically, which is well-understood in terms of quantum electrodynamics (QED). Since they impinge on fixed targets, the initial state of the particle reaction is precisely known, including the polarization of the photon and the target nucleus if desired. Furthermore, owing to the bremsstrahlung spectrum, a range of photon energies is available concurrently within the experiment, which are determined statistically via so-called photon-tagging. This makes such experiments ideally suited to study nucleon resonances, to probe the internal structure of nucleons, and to produce a clean sample of various mesons and their subsequent decays. All those different topics have been covered in the past decade within the A2 collaboration at the MAMI electron accelerator leading to an improved understanding of QCD in the low-energy regime, together with similar experiments at Jefferson Lab, Virginia, U. S. and at ELSA in Bonn, Germany. Complimentary experiments using Compton backscattering of optical laser photons from electrons in storage rings are LEGS at BNL, New York, U. S. and GRAAL at ESRF in Grenoble, France. These combined efforts eventually contribute to a consistent test of QCD predictions over a large energy scale, which is the key to reduce systematic uncertainties in precision measurements probing the limits of QCD and the Standard Model of particle physics.

A main component of the current A2 detector setup is the well-known Crystal Ball (CB) calorimeter, which was built in the 1970s to precisely study the charmonium excitation spectrum, leading to the discovery of the η_c meson. After it was moved to Mainz in 2003, a read-out system was installed from already existing electronics components. In order to reach future physics goals, a prototype development for the CB has been successfully finished within the scope of this thesis, as well as possible upgrades of other detector components of the A2 setup. Based on this knowledge, the existing data acquisition system

(DAQ) has been improved significantly before the high-statistics run in 2014 with the end-point tagger (EPT). Furthermore, many diagnosis tools were established in order to detect problems during beam-time and enhance data quality. The acquired data are analyzed to extract the relative branching fraction of the $\eta' \to \omega\gamma$ decay, which serves as a valuable input to models describing low-energy QCD, as detailed in section 1.3.

This thesis is structured as follows: The experimental setup of the A2 collaboration is presented in chapter 2 including a detailed description of the substantially upgraded data acquisition. Further hardware upgrade feasibility studies are described in chapter 3. In chapter 4, the analysis of the relative branching fraction of $\eta' \to \omega\gamma$ is presented.

Throughout this thesis, natural units in powers of eV are used, that means $\hbar = c = 1$. A glossary with abbreviations used here and henceforth is given on page 127.

1.2. Theory of the strong interaction

The strong interaction is described by the $\mathrm{SU(3)_c}$ color-charge gauge theory QCD, where the degrees of freedom are massive quarks interacting via massless gluons. To understand this statement in detail, the simpler construction of the QED Lagrangian describing the interaction of electrons[1] with photons is presented first. This section is loosely based on [6–10], as it is merely a suitably adapted summary of textbook knowledge.

Quantum electrodynamics (QED)

The Lagrangian yielding the Dirac equation of a free fermion with mass m, such as the electron, is given by[2]

$$\mathcal{L}_0 = \bar{\psi}(i\gamma^\mu \partial_\mu - m)\psi \,, \tag{1.1}$$

where $\psi(x)$ is a complex four-component bispinor field with its adjoint $\bar{\psi} = \psi^\dagger \gamma_0$ and where $\gamma_\mu, \mu = 0 \ldots 3$, are the 4×4 gamma matrices satisfying the defining anti-commutation relation

$$\{\gamma_\mu, \gamma_\nu\} \equiv \gamma_\mu\gamma_\nu + \gamma_\nu\gamma_\mu = 2g_{\mu\nu} \equiv 2\,\mathrm{diag}(1, -1, -1, -1)\,. \tag{1.2}$$

Equation (1.1) is clearly invariant under the *global* transformation

$$\psi \to \exp(-ie\xi)\psi \,, \quad \bar{\psi} \to \exp(ie\xi)\bar{\psi} \,, \tag{1.3}$$

[1] Including their anti-particles positrons, which were predicted by Dirac [5].

[2] The sum over repeated indices, such as μ in equation (1.1), is implied in the following.

where the electric charge e has been introduced as part of the real transformation parameter ξ. The field transformation (1.3) can also be seen as a realization of the group $\mathrm{U}(1) = \{e^{i\phi}, \phi \in \mathbb{R}\}$ acting as a phase rotation of the complex fields $(\psi, \bar{\psi})$ by an angle $(e\xi, -e\xi)$ in the complex plane. As the result of applying two of those rotations successively does not depend on their order, U(1) is called "abelian" or "commutative".

Elevating the global invariance to a *local* U(1) transformation,

$$\psi \to \exp\bigl(-ie\xi(x)\bigr)\psi\,, \quad \bar{\psi} \to \exp\bigl(ie\xi(x)\bigr)\bar{\psi}\,, \tag{1.4}$$

where $\xi(x)$ now depends on the space-time coordinate x^μ, yields for the free Lagrangian in equation (1.1)

$$\mathcal{L}_0 = \bar{\psi}(i\gamma^\mu\partial_\mu - m)\psi \quad \to \quad \mathcal{L}_0' = \bar{\psi}(i\gamma^\mu\partial_\mu + e\gamma^\mu\partial_\mu\xi - m)\psi\,. \tag{1.5}$$

Since the extra term $e\gamma^\mu\partial_\mu\xi$ looks surprisingly similar to a so-called gauge transformation of the four-vector potential,

$$A_\mu \to A_\mu + \partial_\mu\xi\,, \tag{1.6}$$

known from classical electrodynamics, a *locally* U(1) invariant Lagrangian is found as

$$\mathcal{L} = \bar{\psi}\Bigl(i\gamma^\mu(\partial_\mu - ieA_\mu) - m\Bigr)\psi\,, \tag{1.7}$$

which is indeed invariant under the transformations (1.4) and (1.6) for ψ and A_μ, respectively. Adding the dynamics of the field A_μ, which is identified as the photon field after quantization, the complete QED Lagrangian is eventually found as

$$\mathcal{L}_{\mathrm{QED}} = \bar{\psi}(i\gamma^\mu D_\mu - m)\psi - \frac{1}{4}F^{\mu\nu}F_{\mu\nu}\,, \tag{1.8}$$

where the field strength tensor $F_{\mu\nu} = \partial_\mu A_\nu - \partial_\nu A_\mu$ and the so-called covariant derivative $D_\mu \equiv \partial_\mu - ieA_\mu$ are introduced. As already known from classical electrodynamics, $F_{\mu\nu}$ is invariant under transformation (1.6).

Quantization of a classical Lagrangian, referring to the transition from a field to a particle interpretation, can be carried out within the so-called path integral formalism. By assigning each term in the Lagrangian a corresponding Feynman rule, the quantization has a compelling graphical interpretation. For QED, besides propagators for the electron (or positron as interpreted traveling backwards in time) and the photon,

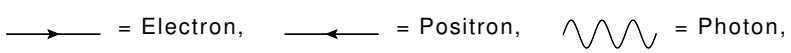

there is only one fundamental vertex given by the local gauge coupling,

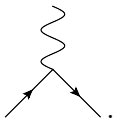

From those graphical building blocks, electron-positron scattering is described by an infinite series of all possible diagrams matching the initial and final state topology:

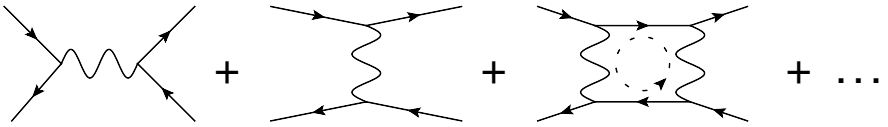

Fortunately, each vertex introduces a small factor of $\sqrt{\alpha}$, where $\alpha = e^2/(4\pi) \approx 1/137$ is the so-called fine structure or electromagnetic coupling constant, such that terms with more vertices are suppressed and the infinite number of diagrams can be seen as a series converging to the scattering process as realized in nature.

The loop diagrams represent an integration $\int d^4k$ over the complete four-momentum space of the "unfixed" momentum k^μ, as indicated by a dashed circle in the last diagram above. In general, this causes logarithmic divergences to appear. It can be shown for local gauge theories that those divergences can always be absorbed by appropriately redefining the finite number of fields and coupling parameters in the "bare" Lagrangian, a technique called renormalization, but to this end an arbitrarily chosen energy scale μ must be introduced at which the renormalization is carried out. The resulting dependence of the coupling constant α on the scale μ is described by the so-called β-function as

$$\beta(\alpha) = \frac{\partial \alpha}{\partial(\log \mu)} \,. \tag{1.9}$$

It can be shown that β does not depend explicitly on the energy scale μ, but only implicitly through the "running" coupling constant $\alpha(\mu)$. For QED, the β-function is positive, which means that the effective coupling increases with the scale μ. Similarly, as distance scales inversely with energy, the effective charge decreases if measured from larger distances. This can be interpreted qualitatively as a screening of charge by virtually created electron-positron pairs and is studied rigorously within renormalization group theory. In order to achieve a fast convergence of the perturbative series, the scale μ is typically chosen to match experimental energy scales, such as the four-momentum transfer q^μ in scattering experiments, so $q^2 \approx \mu^2$. This sometimes leads to the wrong conclusion that the scale μ has some experimentally relevant

interpretation or would somehow influence experimental observables, such as cross sections. In other words, if one could calculate physical quantities in QED non-perturbatively by some other means than path integral formalism, the "hidden" scale μ would have never been introduced, and thus remains a merely theoretical quantity.

In conclusion, the coupling of the electrons to photons mediated by the electric charge e is uniquely determined by requiring local U(1) gauge invariance, and, as this coupling turns out to be small, a perturbative treatment after quantization is meaningful and feasible. However, as U(1) is an abelian group, the mathematical structure of transformation (1.3) and equation (1.8) is rather simple. In the following, this recipe is extended to the non-abelian gauge theory QCD, which leads to important consequences for its perturbative treatment.

Quantum chromodynamics (QCD)

As an example for a non-abelian group, the "special unitary group in three dimensions" is defined as the following set of complex 3×3 matrices,

$$\mathrm{SU}(3) = \left\{ U \,\middle|\, U^\dagger U = \mathbb{1}_{3\times 3},\, \det U = 1 \right\}, \tag{1.10}$$

where the term "special" refers to the condition $\det U = 1$. As it is well-known from Lie group theory, the elements of SU(3) can be parametrized by $3^2 - 1 = 8$ real numbers Θ_a,

$$U = \exp\!\left(-i\Theta_a \lambda_a / 2\right), \tag{1.11}$$

where the Hermitian, traceless generators λ_a are the so-called Gell-Mann matrices. The Gell-Mann matrices satisfy the Lie algebra given by

$$[\lambda_a, \lambda_b] \equiv \lambda_a \lambda_b - \lambda_b \lambda_a = 2i f_{abc} \lambda_c \,, \tag{1.12}$$

where the so-called structure constants f_{abc} uniquely encode the mathematical properties of SU(3).

In formal analogy to the QED Lagrangian in equation (1.8), the complete QCD Lagrangian is therefore constructed as an $\mathrm{SU}(3)_\mathrm{c}$ color-charge gauge theory [11, 12],

$$\mathcal{L}_\mathrm{QCD} = \sum_{f=1}^{6} \bar{q}_f (i\gamma^\mu D_\mu - m_f) q_f - \frac{1}{2} \mathrm{Tr}_\mathrm{c}(\mathcal{G}_{\mu\nu} \mathcal{G}^{\mu\nu}) \,, \tag{1.13}$$

where

$$q_f = \begin{pmatrix} q_{f,\mathrm{r}} \\ q_{f,\mathrm{g}} \\ q_{f,\mathrm{b}} \end{pmatrix}, \quad \bar{q}_f = q_f^\dagger \gamma_0 = \begin{pmatrix} q_{f,\mathrm{r}}^\dagger \gamma_0 & q_{f,\mathrm{g}}^\dagger \gamma_0 & q_{f,\mathrm{b}}^\dagger \gamma_0 \end{pmatrix}, \tag{1.14}$$

is the Dirac bispinor quark field and its adjoint, respectively, written down explicitly as a $\mathrm{SU(3)_c}$ "rgb" color triplet for each of the six quark flavors f, usually denoted up (u), down (d), strange (s), charm (c), bottom (b) and top (t). In analogy to transformation (1.4), the fields are required to *locally* transform using the parametrization in equation (1.11), again introducing the flavor-independent color-charge g by replacing the parameters Θ_a with $g\Theta_a(x)$. In addition, the quantity

$$\mathcal{A}_\mu \equiv \mathcal{A}_\mu^a \frac{\lambda^a}{2} \tag{1.15}$$

represents the $3^2 - 1 = 8$ gluon fields decomposed in the so-called adjoint representation of SU(3). In analogy to equation (1.8), the covariant derivative is given as

$$D_\mu q_f \equiv (\partial_\mu - ig\mathcal{A}_\mu) q_f \,, \tag{1.16}$$

which transforms as the object it acts on by definition. According to equation (1.16), the basis vectors of the decomposition in equation (1.15), in this case the Gell-Mann matrices, should match the potentially arbitrary choice for the representation of the matter fields, which are the quarks in this case. In contrast, the basis vectors of the gluon fields $(\mathcal{A}_\mu^a)_{a=1\ldots8}$ is always of dimensionality $N_\mathrm{c}^2 - 1 = 8$ due to the underlying $\mathrm{SU}(N_\mathrm{c} = 3)$ gauge group. Finally, the gluon field strength tensor is given by

$$\begin{aligned} \mathcal{G}_{\mu\nu} \equiv \mathcal{G}_{\mu\nu}^a \frac{\lambda^a}{2} &= \partial_\mu \mathcal{A}_\nu - \partial_\nu \mathcal{A}_\mu - ig[\mathcal{A}_\mu, \mathcal{A}_\nu] \\ &= \left(\partial_\mu \mathcal{A}_\nu^a - \partial_\nu \mathcal{A}_\mu^a + g f^{abc} \mathcal{A}_\mu^b \mathcal{A}_\nu^c\right) \frac{\lambda^a}{2} \,, \end{aligned} \tag{1.17}$$

where f^{abc} are the SU(3) structure constants as defined in equation (1.12). In contrast to QED, there are additional three- and four-vertex interactions of the gluon fields $\mathcal{A}_\mu^a$ due to the non-vanishing structure constants f^{abc} in equation (1.17), which stem from the non-abelian nature of the gauge group $\mathrm{SU(3)_c}$. This key feature dramatically changes the asymptotic behavior of QCD, as the QCD β-function describing the scaling of the strong coupling constant $\alpha_\mathrm{s} = g^2/(4\pi)$ analogously to equation (1.9) becomes negative. Thus, the coupling α_s decreases with higher energy scales, which is known as "asymptotic freedom". Moreover, below energy scales of $\mu \approx 1\,\mathrm{GeV}$, the coupling becomes larger than 1, which renders a perturbative treatment in powers of g in the low-energy regime impossible, as higher order diagrams with more vertices cannot be neglected as it was the case for QED. The diverging coupling constant manifests itself experimentally by the fact that no free gluons or quarks but only "color-neutral" bound states called hadrons are observed, which is denoted as confinement [13, 14].

Light flavors / MeV	Heavy flavors / GeV
$m_{\mathrm{u}} = 2.2^{+0.6}_{-0.4}$	$m_{\mathrm{c}} = 1.27 \pm 0.03$
$m_{\mathrm{d}} = 4.7^{+0.5}_{-0.4}$	$m_{\mathrm{b}} = 4.18^{+0.04}_{-0.03}$
$m_{\mathrm{s}} = 96^{+8}_{-4}$	$m_{\mathrm{t}} = 160^{+5}_{-4}$

Table 1.1.: The "current-quark" masses for the light flavors u, d, s and the "running" masses for the heavy flavors c, b, t from [17], all given in the mass-independent $\overline{\mathrm{MS}}$ subtraction scheme at scale $\mu \approx 2\,\mathrm{GeV}$. As quarks are confined, their masses should be interpreted as parameters within certain theoretical frameworks, see the review in [17] for details.

Still, non-perturbative approaches to QCD exist, such as ab-initio numerical calculations on the lattice [15, 16] or effective field theories. The latter are presented in more detail in the following to explore the rich physics of the strong interaction in the low-energy regime.

Chiral effective field theories

Since the experimental values of the quark masses given in table 1.1 accidentally divide them into "light" and "heavy" flavors, the limit $m_{\mathrm{u,\,d,\,s}} \to 0$ and $m_{\mathrm{c,\,b,\,t}} \to \infty$ should be a good approximation of QCD in the low-energy regime. In this so-called chiral limit, the Lagrangian reads

$$\begin{aligned} \mathcal{L}^0_{\mathrm{QCD}} &= \sum_{f=u,d,s} \bar{q}_f i\gamma^\mu D_\mu q_f - \frac{1}{2}\,\mathrm{Tr}(\mathcal{G}_{\mu\nu}\mathcal{G}^{\mu\nu}) \\ &= \sum_{f=u,d,s} \left(\bar{q}^R_f i\gamma^\mu D_\mu q^R_f + \bar{q}^L_f i\gamma^\mu D_\mu q^L_f\right) - \frac{1}{2}\,\mathrm{Tr_c}(\mathcal{G}_{\mu\nu}\mathcal{G}^{\mu\nu})\,, \end{aligned} \tag{1.18}$$

where the left- and right-handed quark fields $q_f^{\mathrm{R/L}} = \frac{1}{2}(1 \pm \gamma_5)q_f$ with $\gamma_5 = i\gamma_0\gamma_1\gamma_2\gamma_3$ are introduced. Thus, in this chiral, or "handedness", representation, it is easily seen that $\mathcal{L}^0_{\mathrm{QCD}}$ is invariant under a $\mathrm{U(3)_R} \times \mathrm{U(3)_L} \cong \mathrm{SU(3)_R} \times \mathrm{SU(3)_L} \times \mathrm{U(1)_{V=R+L}} \times \mathrm{U(1)_{A=R-L}}$ symmetry group in flavor space. According to Noether's theorem [18], $(3^2-1)+(3^2-1)+1+1 = 18$ currents j^μ with vanishing total divergence, $\partial_\mu j^\mu = 0$, are expected, each associated to a conserved quantity $Q(t) = \int j^0(\vec{x},t)d^3x$.

However, it is not trivial that the symmetries present in the classical Lagrangian as given by equation (1.18) are still realized after quantization. In

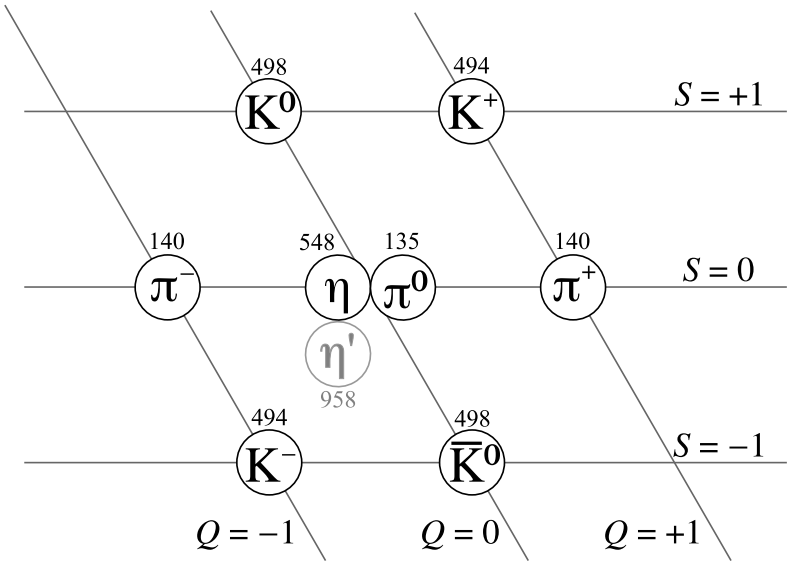

Figure 1.1.: The pseudo-scalar meson octet $J^P = 0^-$ amended by the η' and arranged by the quantum numbers Q (electric charge) and S (strangeness). The approximate masses in MeV are taken from [17] and indicate that SU(3) flavor symmetry for flavors $f = \mathrm{u}, \mathrm{d}, \mathrm{s}$ is not as well realized as the embedded SU(2) symmetry for flavors $f = \mathrm{u}, \mathrm{d}$. This is related to the non-vanishing current masses of the light quarks in table 1.1. See section 1.3 for mixing of the η and η' mesons.

fact, as first shown in [19–21], the axial singlet current associated with $\mathrm{U(1)_A}$ is not conserved and hence its divergence is given in the chiral limit by [7]

$$\partial_\mu j^\mu_{\substack{\text{axial}\\\text{singlet}}} = \frac{3g^2}{32\pi^2}\epsilon^{\mu\nu\rho\sigma}\mathcal{G}^a_{\mu\nu}\mathcal{G}^a_{\rho\sigma} \neq 0\,, \tag{1.19}$$

which is called the chiral quantum anomaly. Thus, QCD in the chiral limit possesses the symmetry

$$\underbrace{\mathrm{SU(3)_R} \times \mathrm{SU(3)_L}}_{\text{chiral symmetry}} \times \mathrm{U(1)_V}\,, \tag{1.20}$$

where the $\mathrm{U(1)_V}$ is associated with the conservation of baryon number B, giving rise to the classification of hadrons into mesons with $B = 0$ and baryons with $B = 1$.

Moreover, according to the chiral symmetry in (1.20), one naively expects an approximate arrangement of hadrons in irreducible multiplets of SU(3) with positive, $V = R + L$, *and* negative parity, $A = R - L$. However, as the experimentally observed low-energy baryons can be arranged in approximately degenerate multiplets of positive parity only, the chiral symmetry is assumed to be spontaneously broken to $\mathrm{SU}(3)_{V=R+L}$. This gives rise to $3^2 - 1 = 8$ Goldstone bosons identified as the pseudo-scalar meson octet consisting of $\pi^{\pm}$, π^0, $K^{\pm}$, K^0, $\bar{K}^0$ and the η, see figure 1.1. In the chiral limit, the mass of the Goldstone bosons vanishes. Their experimentally observed small mass, compared to a typical QCD mass scale of 1 GeV, is thus attributed to the explicit breaking of the chiral symmetry by the non-vanishing mass of the light quarks, see table 1.1.

As already mentioned, QCD cannot be solved perturbatively as a quantum field theory of quarks and gluons in the low-energy regime since the coupling diverges at this energy scale. Fortunately, a solution to this problem is given by Steven Weinberg as a so-far unproven "theorem" [22]:

> The "theorem" says that although individual quantum field theories have of course a good deal of content, quantum field theory itself has no content beyond analyticity, unitarity, cluster decomposition, and symmetry. This can be put more precisely in the context of perturbation theory: if one writes down the most general possible Lagrangian, including all terms consistent with assumed symmetry principles, and then calculates matrix elements with this Lagrangian to any given order of perturbation theory, the result will simply be the most general possible S-matrix consistent with analyticity, perturbative unitarity, cluster decomposition and the assumed symmetry principles.

In this sense, so-called effective field theories use the experimentally observed hadrons as degrees of freedom and construct the most general Lagrangian consistent with the underlying symmetries. In particular, the so-called chiral perturbation theory describes Goldstone bosons ϕ_a as a non-linear realization[3] of SU(3),

$$U(x) = \exp\Big(i\frac{\phi(x)}{F_0}\Big)\,, \tag{1.21}$$

[3]It is non-linear as the unitary elements $U(x)$ in equation (1.21) do not form a vector space.

with the explicit representation of the pseudo-scalar mesons from figure 1.1,

$$\phi = \sum_{a=1}^{8} \phi_a \lambda_a = \begin{pmatrix} \pi^0 + \frac{1}{\sqrt{3}}\eta & \sqrt{2}\pi^+ & \sqrt{2}K^+ \\ \sqrt{2}\pi^- & -\pi^0 + \frac{1}{\sqrt{3}}\eta & \sqrt{2}K^0 \\ \sqrt{2}K^- & \sqrt{2}\bar{K}^0 & -\frac{2}{\sqrt{3}}\eta \end{pmatrix}, \tag{1.22}$$

to implement the spontaneously broken chiral symmetry as [7, 22]

$$\mathcal{L}_{\text{eff}} = \frac{F_0^2}{4}\langle \partial_\mu U \partial^\mu U^\dagger \rangle + \cdots, \tag{1.23}$$

where $\langle \ldots \rangle$ denotes the trace over flavor indices and only the lowest order term with a minimal number of derivatives and without any external currents is given. The effective Lagrangian in equation (1.23) contains an infinite number of terms with a-priori unknown low-energy constants (LECs) as coefficients, such as the pion decay constant F_0. To restore predictive power of the theory, each term in the effective Lagrangian—leading to a Feynman rule to construct corresponding Feynman diagrams—is given an order according to the power of a small expansion parameter δ, which is the Goldstone boson momentum in this case. This procedure is known as Weinberg's power counting. Still, the remaining finite number of LECs, whose numerical values depend also on the employed renormalization scheme, need to be determined from experimental values. The theory can be extended to include the proton and neutron as isospin partners of the nucleon as well as vector mesons, such as the ρ and the ω mesons [23, 24], and the coupling to photons is realized as external vector currents. However, establishing a consistent power counting scheme for this extended case is non-trivial due to the separate mass scales introduced by the nucleon or the vector mesons. Furthermore, the number of LECs contributing to a specific process increases rapidly, which renders one-loop calculations already challenging and deteriorates the predictive power and the accuracy of chiral effective field theories (χEFTs).

1.3. Physics of the $\eta' \to \omega\gamma$ decay

This section highlights the physics of the $\eta' \to \omega\gamma$ decay in terms of χEFTs as well as previous measurements investigating this decay. The η' is a pseudo-scalar meson, $J^{PC} = 0^{-+}$, with a mass of $m_{\eta'} = (957.78 \pm 0.06)\,\text{MeV}$ [17]. The ω is a vector meson, $J^{PC} = 1^{--}$, with a mass of $m_\omega = (782.65 \pm 0.12)\,\text{MeV}$ [17]. Hence, $\eta' \to \omega\gamma$ belongs to the group of so-called pseudoscalar-vector-gamma ($PV\gamma$) decays. As a two body process, the only physically interesting

quantity of this decay is the branching fraction $\mathrm{BR}(\eta' \to \omega\gamma) = \Gamma/\Gamma_{\mathrm{tot}}$, where Γ is the partial width for this particular decay and $\Gamma_{\mathrm{tot}} = (0.197 \pm 0.009)\,\mathrm{MeV}$ [17] the total width of the η' meson.

As the mass of the η' meson does not vanish in the chiral limit since it cannot be identified as a Goldstone boson, it could be treated just as any other massive degree of freedom, such as the vector mesons, within conventional χEFTs. However, it is instructive to regard the η' meson in terms of the $\mathrm{U}(1)_{\mathrm{A}}$ anomaly in the so-called large-N_{c} limit, where QCD is generalized to an $\mathrm{SU}(N_{\mathrm{c}})$ gauge theory [25]. Hence, $1/N_{\mathrm{c}}$ is treated as another small expansion parameter δ similar to the Goldstone boson momentum. As it can be argued from renormalization group theory, the coupling g behaves as $1/\sqrt{N_{\mathrm{c}}}$, which makes the anomaly in equation (1.19) disappear in the large-N_{c} limit. Thus, in large-N_{c} chiral perturbation theory (LN_{c}ChPT), the η' meson is interpreted as a ninth Goldstone boson in the limit $N_{\mathrm{c}} \to \infty$. This is implemented by amending equation (1.22) as follows,

$$\begin{aligned}\phi &= \sum_{a=0}^{8} \phi_a \lambda_a = \sum_{a=1}^{8} \phi_a \lambda_a + \lambda_0 \eta_1 \\ &= \begin{pmatrix} \pi^0 + \frac{1}{\sqrt{3}}\eta_8 + \sqrt{\frac{2}{3}}\eta_1 & \sqrt{2}\pi^+ & \sqrt{2}K^+ \\ \sqrt{2}\pi^- & -\pi^0 + \frac{1}{\sqrt{3}}\eta_8 + \sqrt{\frac{2}{3}}\eta_1 & \sqrt{2}K^0 \\ \sqrt{2}K^- & \sqrt{2}\bar{K}^0 & -\frac{2}{\sqrt{3}}\eta_8 + \sqrt{\frac{2}{3}}\eta_1 \end{pmatrix},\end{aligned} \tag{1.24}$$

where $\lambda_0 = \sqrt{2/3}\,\mathbb{1}$. Since $\mathrm{Tr}\,\lambda_0 \neq 0$, the chiral symmetry in (1.20) is promoted to $\mathrm{U}(3)_{\mathrm{R}} \times \mathrm{U}(3)_{\mathrm{L}}$, as the unitarian Goldstone fields in equation (1.21) do not have a unit determinant anymore, $\det U = \exp(i\phi_0/F_0\,\mathrm{Tr}\,\lambda_0) \neq 1$.

The physically observed pseudo-scalars π^0, η and η' all possess the same quantum numbers, such as vanishing strangeness, as depicted in figure 1.1. Already the simple question how those mesons are composed in terms of their quark flavor contents $\mathrm{u\bar{u}}, \mathrm{d\bar{d}}, \mathrm{s\bar{s}}$ is non-trivial, as in this case QCD induces transitions between quarks of different flavors via annihilations to gluons [26]. In particular, the so-called mixing of the η and η' states as a linear combination from the flavor singlet η_1 and octet η_8, see equation (1.24), has been investigated since the late 1970s using a parametrization with a single mixing angle θ_P. However, phenomenology yielded largely inconsistent values for θ_P ranging from $-10°$ to $-20°$. This has been resolved around the year 2000 as rigorous considerations in LN_{c}ChPT [26] showed that a parametrization using two mixing angles is more appropriate. Nevertheless, the correct implementation of η-η' mixing beyond leading order is a subject of current research, see for example [27], and the phenomenon involves answering fundamental questions

concerning explicit and spontaneous symmetry breaking in QCD and the non-perturbative nature of the $\mathrm{U(1)_A}$ anomaly.

The vector meson ω is usually implemented as a four-vector V^μ to conveniently formulate a Lorentz-invariant effective Lagrangian in the sense of Weinberg's "theorem". However, within the Hamiltonian formalism, introducing four fields V^μ and canonically conjugated momenta to describe a massive spin-1 particle with $2S + 1 = 3$ degrees of freedom leads to the appearance of so-called primary constraints during canonical quantization, from which the velocities $\dot{V}$ are not solvable to construct the conjugated momenta. This is resolved by the physical requirement that such constraints shall be conserved in time, which in general leads to additionally consistency equations involving the LECs. This improves the predictive power of χEFTs and relations known from phenomenology can be shown rigorously [28]. Employing the same constraint analysis to the usually favored description of massive vector mesons as antisymmetric tensors representing 6 degrees of freedom is a topic of current research, see for example [9].

In summary, $PV\gamma$ interactions such as the $\eta' \to \omega\gamma$ decay provide a challenging subject for effective field theories, probing the correct implementation and understanding of explicitly and spontaneously broken symmetries as well as the proper treatment of massive vector particles in terms of necessary constraints. Due to the large number of LECs, many different hadrons and their decay channels need to be studied experimentally, and this thesis contributes to this endeavor in chapter 4 with the analysis of the relative branching fraction of the $\eta' \to \omega\gamma$ decay. For example, in [29] a LN_cChPT including vector mesons is constructed and applied to explain the phenomenology. Depending on which experimental values are used to determine the LECs, other values can be predicted and thus serve as a test of this model. In particular, the value for the decay width extracted from fit reads

$$\Gamma(\eta' \to \omega\gamma) = (7.4 \pm 1.0)\,\mathrm{keV}\,, \tag{1.25}$$

which is in reasonable agreement with the experimental value of $(6.2 \pm 1.1)\,\mathrm{keV}$.

The current global fit for the relative partial decay width is [17]

$$\Gamma(\eta' \to \omega\gamma)/\Gamma_\mathrm{tot} = (2.62 \pm 0.13) \times 10^{-2}\,, \tag{1.26}$$

which is dominated by the most recent measurement from the BESIII collaboration [30] given as

$$\mathrm{BR}(\eta' \to \omega\gamma) = (2.55 \pm 0.03_\mathrm{stat} \pm 0.16_\mathrm{syst}) \times 10^{-2}\,. \tag{1.27}$$

The BESIII collaboration uses the electron-positron collider BEPCII in Beijing to resonantly produce a huge amount of J/ψ mesons within the BESIII detector

system. The radiative decay $J/\psi \to \eta'\gamma$ serves as a source of about 6.8×10^6 η' mesons, giving a signal yield of 33.2×10^3 events. As further discussed in chapter 4, the A2 collaboration produced an equally large sample of η' mesons and thus the A2 measurement can serve as a valuable cross-check for the global fit in equation (1.26).

2. Experimental setup

This chapter describes the apparatus needed to carry out experiments with energy-tagged photons. It focuses on the mechanical and technical aspects of the components and the currently deployed read-out system, including the improvements for the measurement campaign from July to December 2014. Since the key objective of this campaign is to measure the η' photo-production at the high energy photon end of the specifically designed EPT, the campaign is commonly referred to as "EPT 2014 measurements" or "η' 2014 measurements" in the following. Finally, this builds the foundations for the efforts described in chapter 4.

The A2 detector system is located in the Tagger experimental hall at the Institut für Kernphysik, Mainz, Germany. A schematic overview of the relevant components along the electron and photon beam-line is shown in figure 2.1 on the following page. The electron beam from the MAMI accelerator produces bremsstrahlung photons on a radiator, which are tagged by magnetic analysis and subsequent detection of the time-correlated electrons. Next, the photon beam is collimated and impinges on the liquid hydrogen target. The reaction products are subsequently detected in the CB and TAPS detector systems.

The right-handed Cartesian coordinate system in the lab frame originates in the center-of-mass of the ideally positioned liquid hydrogen target cell coinciding with the center-of-mass of the CB icosahedron. The z-axis is pointing towards the ideal direction of flight of the photons, and the xy plane is rotated such that the x-axis points to the left in the horizontal plane.

2.1. The electron accelerator MAMI

The MAMI facility provides a continuous-wave electron beam with energies of up to 1604 MeV and unpolarized currents of up to 100 µA [32].

Unpolarized electrons are conventionally extracted from a heated metal wire using a Wehnelt cylinder. Next, a linear accelerator (LINAC) stage of microwave cavities increases the electron energy to about 4 MeV and thus to 99 % speed of light, which is required for the injection into the so-called race track microtron (RTM) stages as shown in figure 2.2: Bending magnets re-utilize a dedicated LINAC stage in multiple turns, until the accelerated

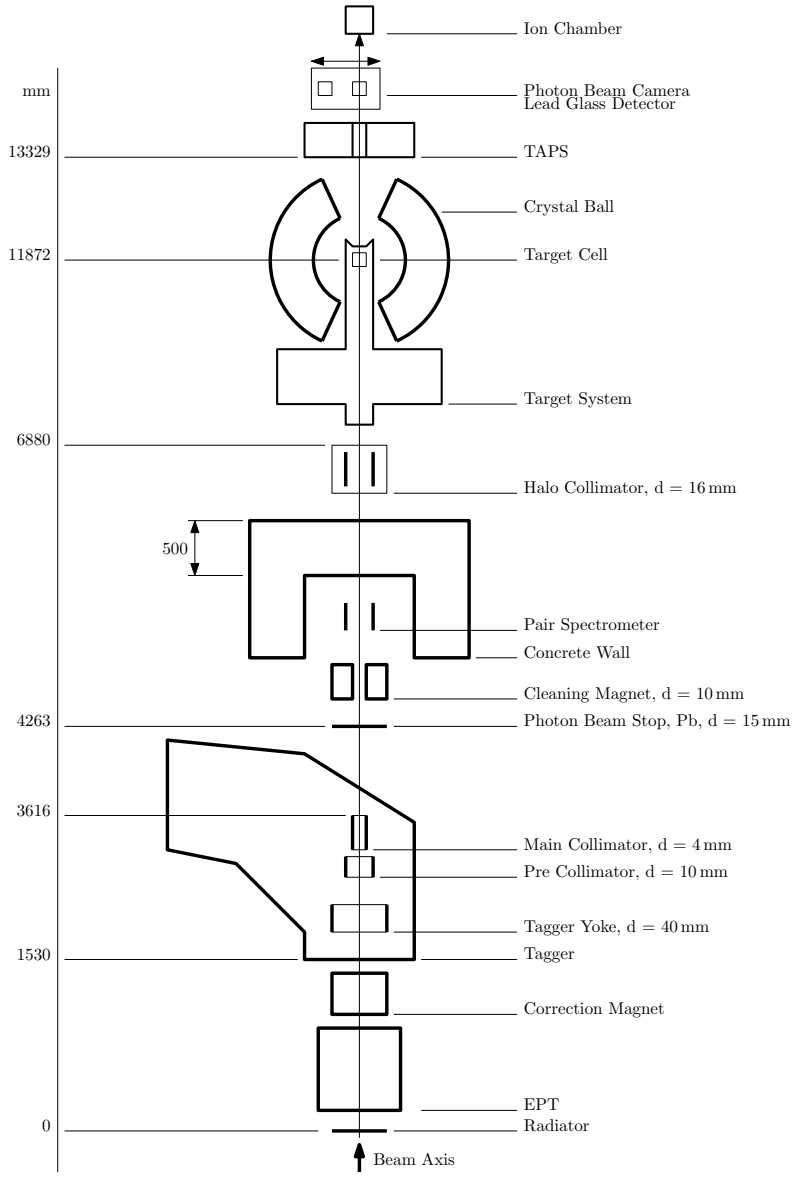

Figure 2.1.: A2 experiment hall overview, adapted from [31] (not to scale). The MAMI electron beam enters from the bottom and is converted into a photon beam at Radiator 1. This secondary beam impinges on the target after collimation and the mostly unscattered photons finally reach the Ion Chamber.

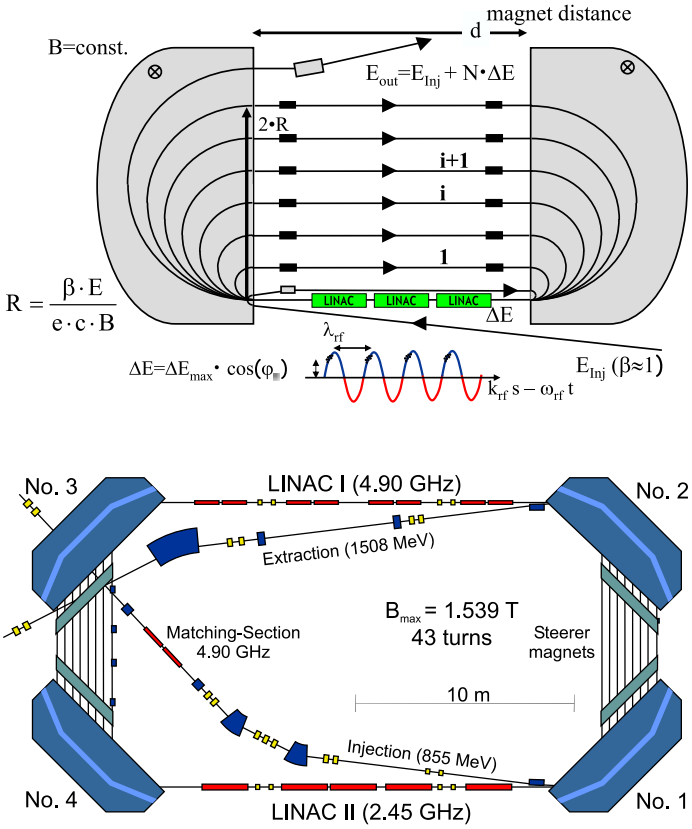

Figure 2.2.: The RTM in the top panel consists of two bending magnets re-utilizing the same linear accelerator multiple times. The HDSM design in the bottom panel keeps the size of the magnets for higher energies technically achievable. Adapted from [32, 33].

beam is extracted by a kicker magnet. This keeps the overall size and thus construction costs reasonable while still providing excellent beam emittance and stability. Using this construction principle, the first three RTM stages, called MAMI-B, achieve 855 MeV nominal energy, see figure 2.3.

The last and largest RTM stage of MAMI-B needs already magnetic fields close to the ≈ 2 T saturation field of the iron yokes and hence the energy can only be increased by scaling up the physical dimensions allowing larger radii of the electron flight paths. Furthermore, the relatively low energy gain per turn is compromised by the increasing losses due to synchrotron radiation of the bent electrons. Those considerations gave rise to the construction of the HDSM [32], enabling nominal beam energies of up to 1508 MeV. The key

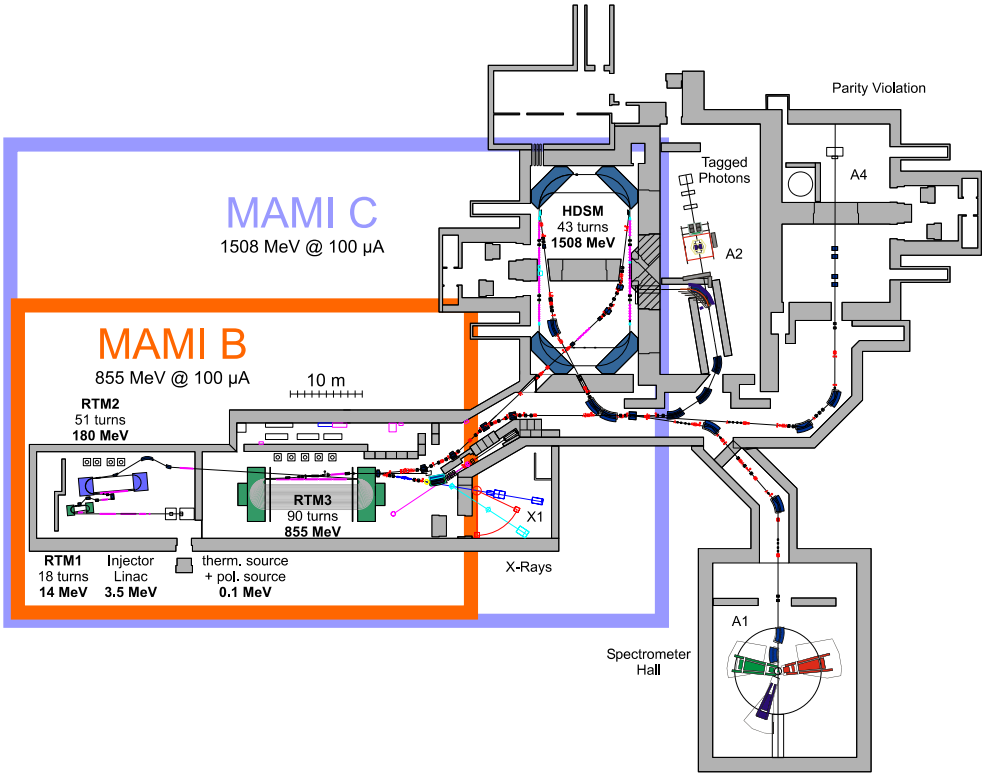

Figure 2.3.: A MAMI accelerator facility floorplan at the Institute für Kernphysik in Mainz from [32]. Either the 855 MeV MAMI-B beam or the 1508 MeV MAMI-C beam can be utilized by the experiments A1 and A2. The MESA accelerator is currently under construction at the former A4 experiment site.

design idea is to split both bending magnets into two separate parts and to use two LINAC sections where one is operated with twice the standard MAMI microwave frequency of 2.45 GHz to achieve phase stability.

By pushing all stages and their auxiliary components of the accelerator system to their operation limits, a maximum beam energy of 1604 MeV for the so-called MAMI-C stage, consisting of MAMI-B and the HDSM, is achieved, with an energy stabilization of about 10 keV over a timespan of one week [32]. As the minimum photon energy to produce the η' meson off the proton is roughly 1450 MeV, operating at the maximum instead of nominal beam energy triples the theoretically accessible kinematic range for the photo-production of η' mesons.

2.2. The end-point tagger (EPT)

As shown in figure 2.4, the MAMI electron beam impinges on a radiator, which is a folded copper (Cu) foil with thicknesses of 5 µm, 10 µm or 15 µm. About 0.1 % of the electrons[1] emit bremsstrahlung photons in the vicinity of a Cu nucleus,

$$e^- + \mathrm{Cu} \rightarrow \mathrm{Cu} + e^- + \gamma\,,$$

and since the recoil energy of the heavy Cu nucleus can be neglected, the energy of the emitted photon is determined by

$$E_\gamma = E^{e^-}_{\mathrm{beam}} - E^{e^-}_{\mathrm{tagged}}\,. \tag{2.1}$$

The chosen radiator thickness of 10 µm provides a sufficient rate of bremsstrahlung photons with a negligible probability of multiple electron scattering within the foil. The radiator can be set using a remotely controlled motor and is removed completely from the electron beam-line during MAMI beam optimization to prevent any radiation damage to the detector system.

The energy and angular dependence of the bremsstrahlung cross section is approximated by [34–37]

$$\frac{d\sigma}{dE_\gamma} \sim 1/E_\gamma\,, \qquad\qquad \frac{d\sigma}{d\theta} \sim \frac{\theta}{(\theta^2 - \theta_\mathrm{c}^2)^2}\,,$$

respectively, with the critical angle $\theta_\mathrm{c} \approx m_e/E^{e^-}_{\mathrm{beam}}$, which is in the order of mrad for typical MAMI beam energies. Since over 50 % of the photons are emitted within an deflection angle below θ_c, the notion "photon beam" is indeed justified. Furthermore, the beam is collimated by lead pinholes with a final diameter of 4 mm to provide a well-defined photon beam spot on the target, which is monitored by a luminescent screen in front of the ionization chamber, see also figure 2.1.

The EPT determines the scattered electron energy $E^{e^-}_{\mathrm{tagged}}$ in equation (2.1) with a spectrometer magnet and 47 detectors close to its focal plane, see figure 2.4. Each detector module consists of a 12.5 mm wide and 8 mm thick scintillator piece, a light guide and a photomultiplier tube (PMT). This yields a clean waveform with high signal to noise ratio for impinging electrons, which are

[1] The fraction can be estimated from d/X_0, where $d \ll X_0$ is the foil thickness and $X_0 \approx 1.4\,\mathrm{cm}$ the radiation length of Cu.

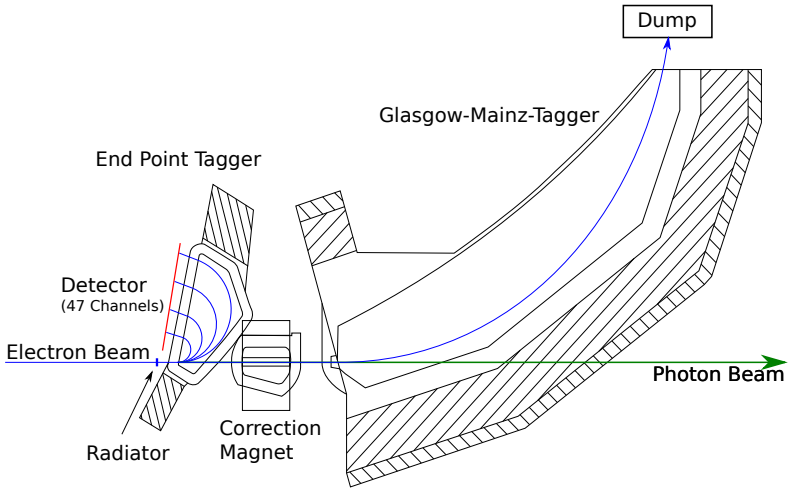

Figure 2.4.: The EPT is installed before the Glasgow tagger and a correction magnet to ensure the correct flight path for unscattered electrons into the beam dump. It covers the low energetic end of the scattered electrons and thus allows studying events with highest photon energies, from [37].

clearly visible in integral measurements[2] carried out for high voltage (HV) and discriminator threshold tuning, see figure 2.5. The photon energy resolution of $\sigma_{E_\gamma} \approx 1.5\,\mathrm{MeV}$ is dominated by the width of the detector elements. The energy calibration for each detector element is based on the simulated flight path of electrons with constant momentum through the measured magnetic field map of the dipole [37]. The field strength is monitored during the experiment with a Hall probe located between the pole shoes. In order to bend the unscattered electrons into the beam dump with the help of the Glasgow-Mainz tagger, a correction dipole with opposite field direction is installed after the EPT magnet.

At the end of the photon beam-line, an ionization chamber is installed to detect the flux of unscattered photons. Its ratio to the total rate of electrons detected in the EPT, called the "LadderP2Ratio", is an indication for the alignment of the electron beam on the radiator. During beam position opti-

[2]The EPT integral measurements are carried out with LeCroy 1885F FASTBUS modules using a Versa Module Europa bus (VMEbus) controller, which are only activated for such measurements due to performance reasons. Their readout timing is only working correctly if the whole FASTBUS crate is readout due to timing issues although only one module is needed for the 47 EPT channels.

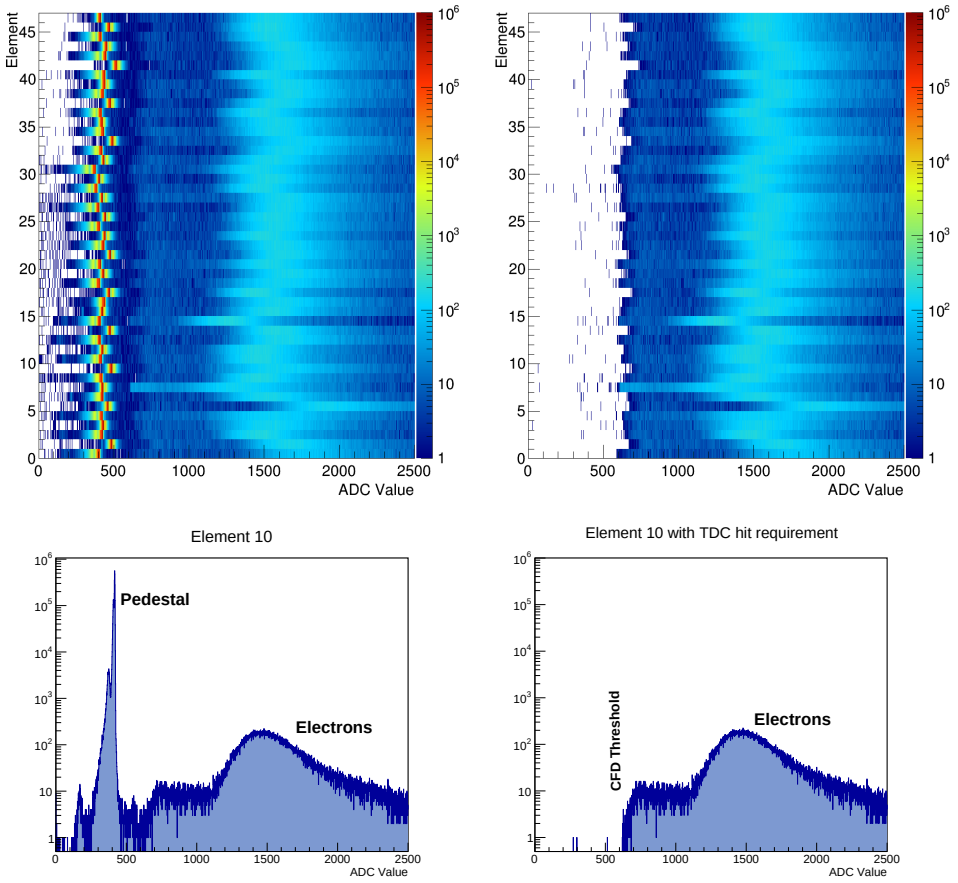

Figure 2.5.: For all 47 EPT elements, the integral output of the analog signal is shown as the raw ADC value. In the left upper panel, energy depositions from electrons around 1500 ADC counts are clearly separated from the pedestal needles at 400. The right upper panel requires a TDC hit, which makes the configured CFD threshold visible for each channel. It shows that the HV voltages and the thresholds are tuned such that no electron hits are rejected but pedestals properly suppressed, as it is exemplified for element 10 in the lower row.

mization, the "LadderP2Ratio" is minimized in order to maximize the photon flux under constant beam current. The MAMI beam current is monitored with a Faraday cup installed in the beam dump.

2.3. The liquid hydrogen target system

The produced photons impinge on hydrogen molecules, interacting predominantly with the contained protons at typical energies of a few hundred MeV. In order to increase the proton density and thus the luminosity by a factor of 50, the gaseous hydrogen is liquefied by a compressor system from the DAPHNE experiment [38] providing a stable temperature of 20 K, which is the condensation point of hydrogen at atmospheric pressure. The temperature is stabilized by either adding liquefied hydrogen to the cell or heating the cell electrically, which results in a typical pressure of gaseous phase in the target cell of 1080 mbar. This light excess pressure compared to atmosphere ensures a reliable leak detection for safety reasons. The target apparatus is monitored and controlled by a dedicated computer system [39].

The target cell in figure 2.6 is (10.0 ± 0.1) cm long and has a diameter of 4.0 cm under cold conditions [39]. The chosen length of the target is a trade-off between a sufficient number of protons as interaction targets and the precise knowledge of the vertex position. In order to keep the amount of other material around the liquid hydrogen as low as possible but still achieve sufficient thermal insulation, the inner target cell is made of 125 µm thick Kapton foil, isolated by eight layers of 8 µm Mylar and 2 µm aluminum compound foil and protected by 1 mm CFK tube. In addition, 25 µm Kapton foil is attached to prevent ice formation close to the target cell.

2.4. The Crystal Ball (CB) detector system

As shown in figure 2.7, the CB detector system consists of the electromagnetic NaI calorimeter itself and two inner detectors, the particle identification detector (PID) and two coaxial cylindrical multi-wire proportional chambers (MWPCs). As test measurements in July 2014 have shown, the MWPCs could not cope with the three times higher photon fluxes now available due to the upgraded read-out system described in section 2.6, and hence, they are not used but left installed during the EPT measurement campaign.

The PID is a barrel detector of 24 scintillators with 50 mm length and 4 mm thickness, each element covering 15° of azimuthal ϕ-angle. The detector was constructed in 2007 and replaces the first version from 2004 [40–42]. It

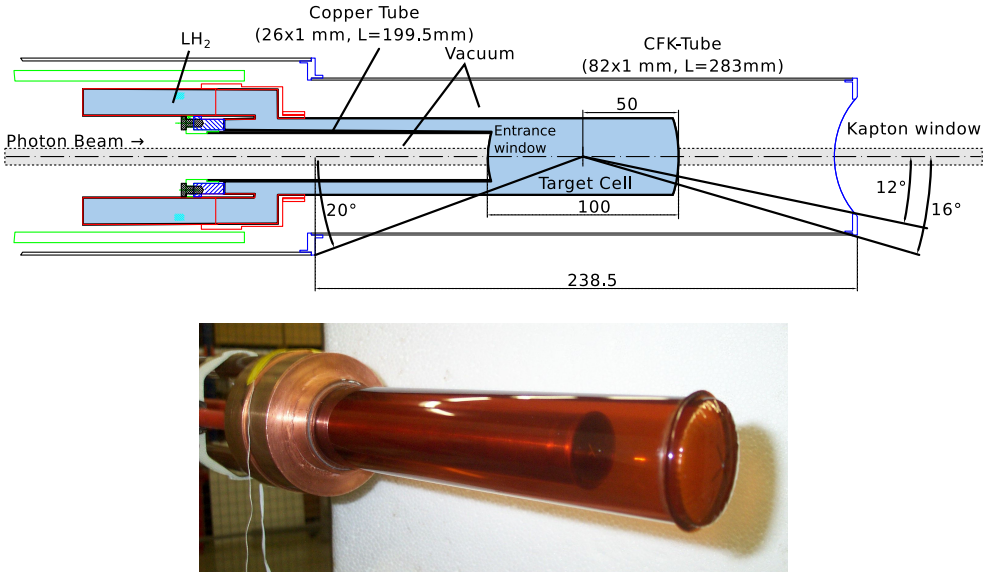

Figure 2.6.: The liquid hydrogen target geometry with 10 cm long inner target cell, adapted from [39, 40]. Its length is measured under cold conditions with the photon beam as an x-ray source and Polaroids as photo plates. It can be changed to 5 cm and 15 cm by different entrance window adapters. The photo shows the target cell with the beam exit window and the semi-transparent Kapton foil to the right.

measures the small energy deposition ΔE of charged particles, such as protons or electrons, and thus allows for the discrimination of different particle types using the $\Delta E/E$ technique if the deposition can be successfully matched to a cluster with energy E in the calorimeter.

The CB NaI calorimeter was constructed in the mid-1970s [43] and, after being deployed at different experiments, moved to Mainz in 2003 [44]. The 672 truncated pyramid crystals are arranged in an icosahedron geometry divided in two hemispheres separated by an equator gap of 10 mm, as shown in figure 2.8. They cover the full azimuthal angle and a polar angle of $22° \lesssim \theta \lesssim 158°$ corresponding to 94 % of 4π sr solid angle in the lab frame. The crystals are optically isolated from each other and thus the detector is ideally suited to determine the location and energy of electromagnetic showers.

Since the scintillation light of NaI has a typical rise-time of 30 ns and is converted to electrical signals with fast PMTs, an analog sum of all inputs can be used to trigger the read-out, called the CB energy sum trigger. To this

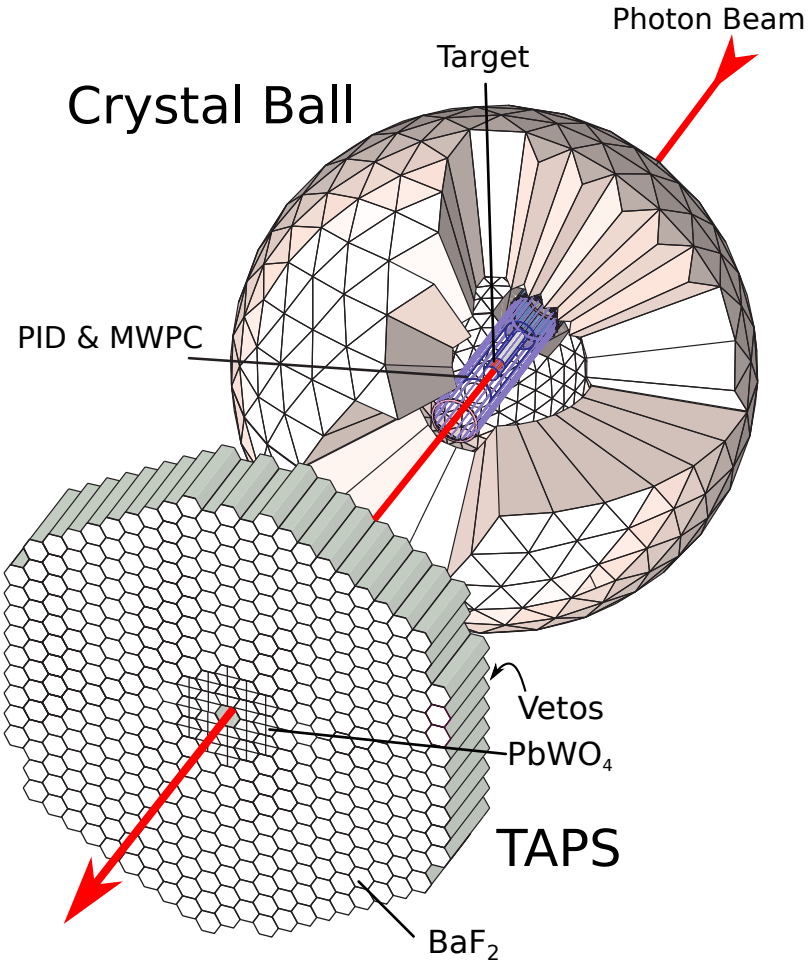

Figure 2.7.: The A2 detector system. The CB apparatus consists of the inner detectors surrounding the target, PID and MWPC, and NaI calorimeter array, which consists of 672 NaI crystals (some not drawn), excluding $720 - 672 = 2 \times 24$ crystal positions around the entrance and exit of the photon beam. The TAPS apparatus in forward direction consists of 384 BaF_2 modules and 72 $PbWO_4$ crystals close to the beam axis. In addition, 402 hexagonal plastic scintillator "Vetos" are installed in front of the crystals.

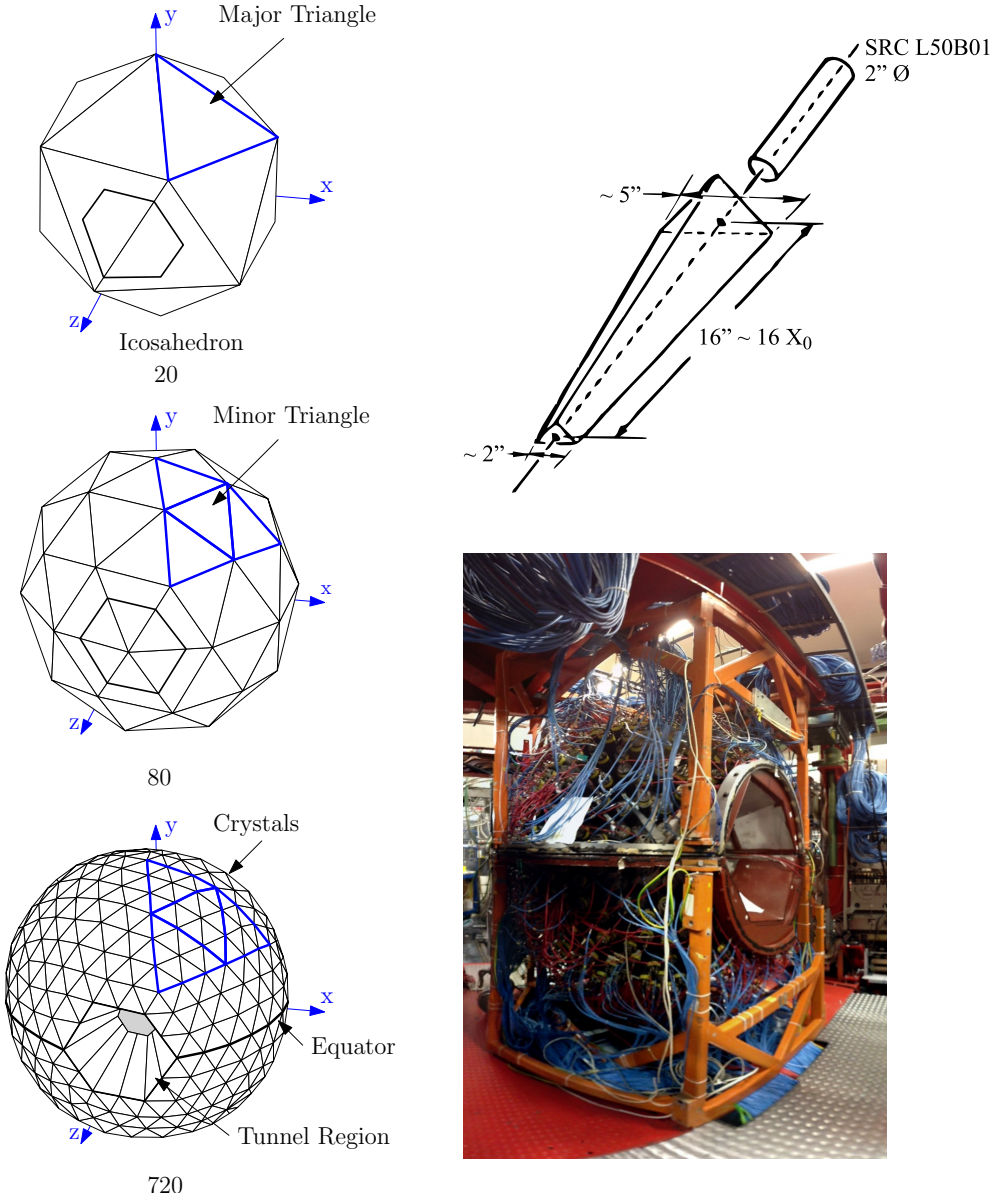

Figure 2.8.: CB icosahedron geometry. The twenty major triangles are divided into four minor triangles, each consisting of 9 truncated pyramids as crystal positions. On the right, one truncated pyramid crystal including the attached PMT is shown, and a picture of the CB detector as currently installed in Mainz, viewed from the downstream side of the photon beam, where TAPS is positioned during experiment. See also figure 2.7.

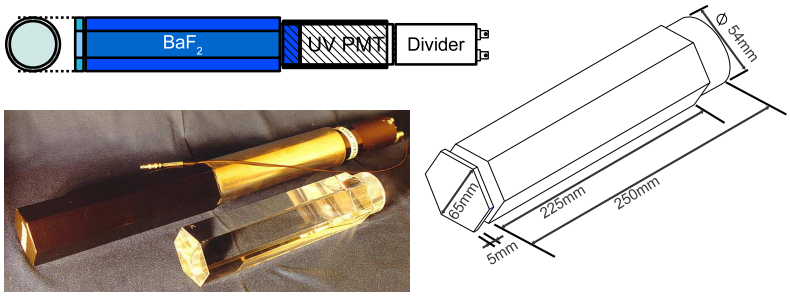

Figure 2.9.: The optically isolated BaF_2 crystal is directly read-out by a PMT. The Veto scintillator light is transferred via fibers to MCP PMTs. From [40].

end, the HV of each PMT must be tuned to obtain a homogeneous trigger response [45–47]. This calibration is carried out with a radioactive americium-beryllium source emitting 4.438 MeV photons, which corresponds to roughly 1 % of typical energy depositions during beam times.

2.5. The two-arm photon spectrometer (TAPS)

Due to the fixed target geometry of the experiment, the final state particles are scattered predominantly in the forward direction. Hence, a part of the modular TAPS detector system [48, 49] is installed as a forward wall calorimeter to cover the polar angle region of $4° \lesssim \theta \lesssim 20°$. The 384 hexagonally shaped BaF_2 detector modules, as shown in figure 2.9, are arranged in six sectors around the beam axis. Additionally, in order to handle the higher particle fluxes close to the beam axis, 72 $PbWO_4$ crystals have been installed as a replacement for the two inner BaF_2 rings [50], as shown in figure 2.7.

In front of each BaF_2 module (or a group of four $PbWO_4$ crystals), a hexagonally shaped plastic scintillator with 5 mm thickness is installed [51]. Those 402 so-called Veto elements measure the small energy loss of charged particles and facilitate $\Delta E/E$ particle identification, similar to the PID elements in the CB detector.

Since the distance of the TAPS front face from the target center is 145.7 cm and the timing resolution is about 1 ns, the time-of-flight (ToF) distinguishes photons and highly relativistic electrons from neutrons and protons. In addition, the ratio of the slow and fast component of the BaF_2 scintillation light varies for hadronic and electromagnetic showers. Based on this effect, the pulse shape analysis (PSA) technique is available for the identification of particles. As

discussed in more detail in section 4.1, the scattered protons from η' photoproduction at EPT incident photon energies have a maximum polar angle of $\theta_{\max} \approx 22°$, which renders TAPS a well-suited proton detection device.

2.6. Upgrade and improvements in October 2013

This section describes the various improvements undertaken before the EPT measurement campaign and discusses details of the DAQ related to those efforts. Within the scope of this thesis, the stability and performance of the DAQ has been improved significantly, rendering the subsequent beam-times less error-prone and thus more efficient. Those efforts also contributed to the hardware feasibility studies for new DAQ components presented in chapter 3, as a sound examination of the status quo is a prerequisite both for potential hardware replacements and incremental upgrades. In the following, the term "performance" is used to describe the speed of the data acquisition, which is quantified by the mean read-out time for typical events. Obviously, this depends on the experimental conditions: For example, the higher the beam energy, the more reaction products are scattered in forward direction leading to more data to be read-out in the corresponding solid angle. In contrast, the term "stability" is used to describe improvements for the maintainability and reliability of the system. This is quantified by the percentage of provided beam-time actually used to record data flawlessly. For example, up to 10 % of the beam time in October 2012 was exclusively used to restart the DAQ. The upgrade took place from October 2013 until the beam time in December 2013 and consists of several parts, which all together are necessary to achieve the desired performance and stability improvement. Extensive technical documentation of this upgrade is available as a DokuWiki [52], which has been specifically commissioned for this upgrade and later expanded to a collaboration-wide source of practical information.

Accompanying the move of the CB calorimeter to Mainz in 2003, a new data acquisition was installed to digitize analog signals from the electron tagger ladder, the CB calorimeter, the PID and the MWPCs. The COMPASS experiment provided the majority of hardware components [53]. For example, the COMPASS Accumulate Transfer and Cache Hardware (CATCH) with 9U VMEbus form factor is used with $\mathcal{F}1$ TDC Application-Specific Integrated Circuit (ASIC) mezzanine cards to measure the timings of all detectors except for the TAPS apparatus. A simplified overview of the DAQ components as of 2014 is shown in figure 2.10. Usually, auxiliary analog circuits split the signal path to measure the integral of signals in parallel to the timing. For

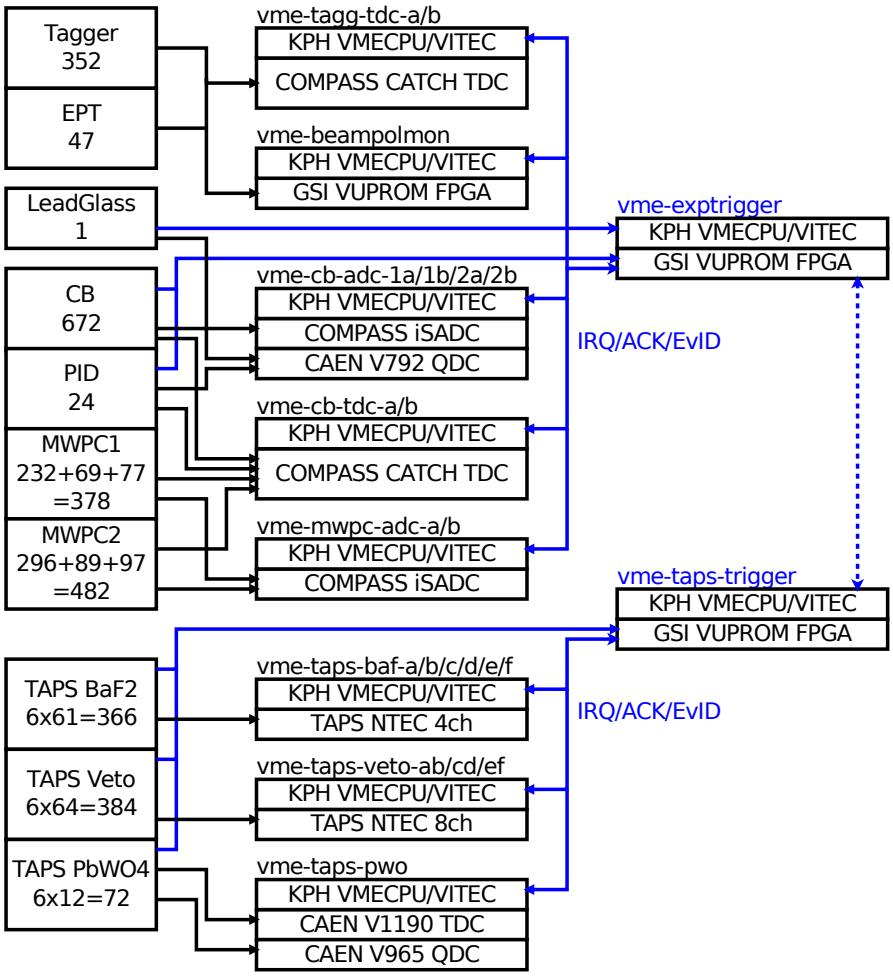

Figure 2.10.: A simplified layout of detector and associated DAQ components as of 2014. On the left of the diagram, the detectors and their physical number of channels are shown (for example, CB has 720 logical channels, but the beam entrance and exit region are left out). Their connection to the VMEbus crates are shown which usually handle the digitization of timings (TDC) and integral measurements (ADC/QDC). Furthermore, the trigger system, which is mainly based on VUPROM FPGA boards, is displayed very simplistically in blue, handling the read-out with interrupt (IRQ), acknowledge (ACK) and event number (EvID) distribution.

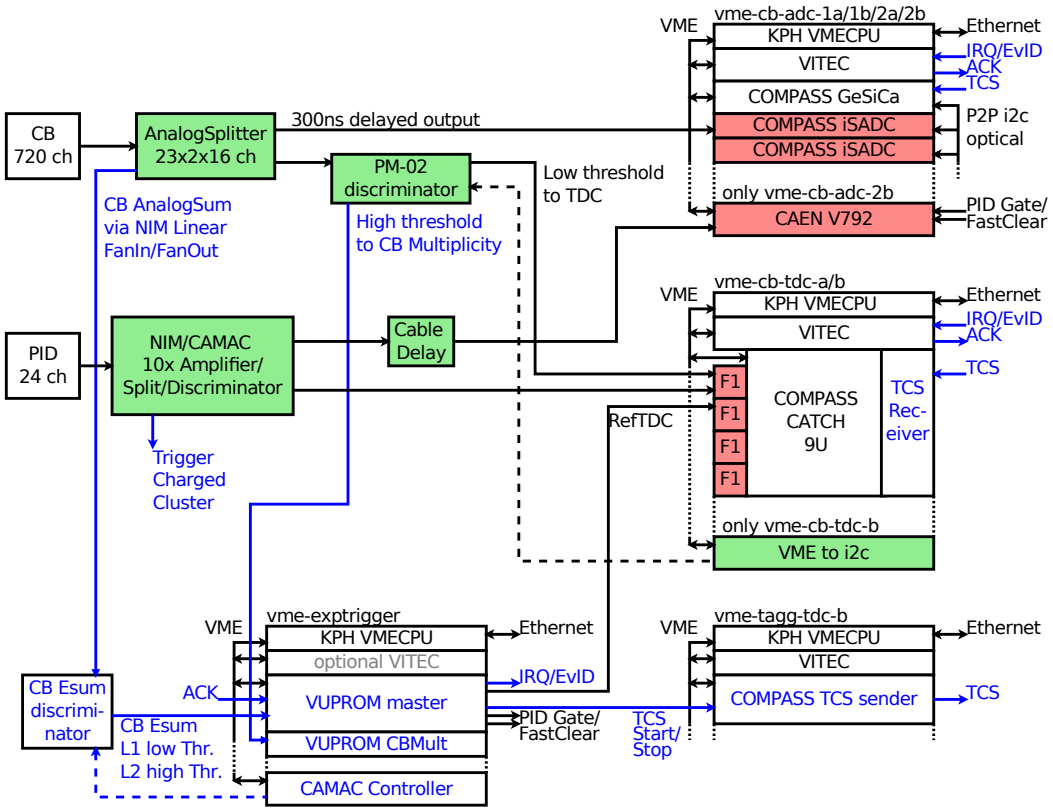

Figure 2.11.: Components of the COMPASS-based DAQ for the CB and PID detectors. Blue indicates trigger components, green indicates FEE components, red indicates TDC or ADC components. Most parts are located in VMEbus crates, denoted with their corresponding host names `vme-*` assigned to the KPH VMECPU, see also section 2.6.1. The analog signals from CB are split, delayed and discriminated with specialized hardware to serve the trigger system with fast event information such as hit patterns and the CB energy sum (Esum) trigger signal. The 24 PID channels are handled with standard NIM and CAMAC parts. The 720 CB channels account for the full icosahedron geometry, of which only 672 are in use due to beam entrance and exit holes. Due to historical reasons, the COMPASS TCS sender is still located in a tagger-related crate. Note that for simplicity, not all trigger connections and level converters are shown and the MWPCs and the tagger, which are also read-out by COMPASS CATCH and iSADC hardware components, are omitted.

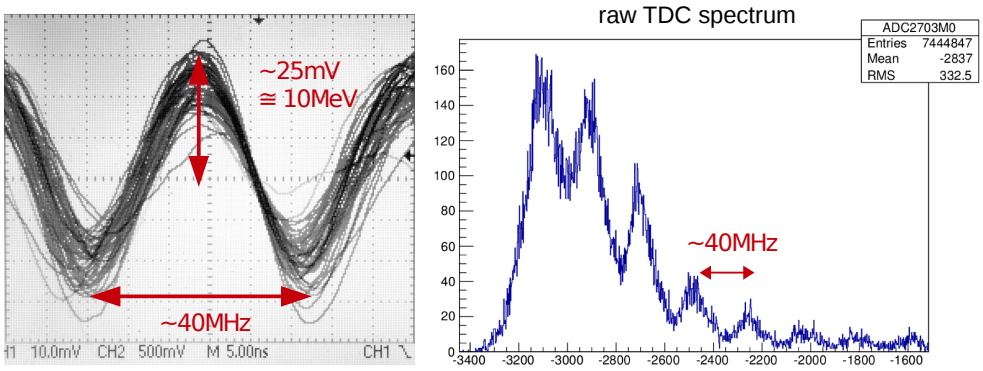

Figure 2.12.: The CB analog sum signal shows a humming structure of about 40 MHz as measured directly with a oscilloscope (left panel). This hum is also visible in the TDC raw spectrum of some channels (right panel). Several mitigations, such as better shielding, have been tried unsuccessfully. From [54].

example, the CB and MWPC signals are digitized with COMPASS sampling ADC boards, called iSADC, in combination with GEM Silicon Control and Acquisition (GeSiCa) VMEbus boards. This is depicted in more detail in figure 2.11 for the current realization after the upgrade.

The COMPASS read-out is designed to work with the bunched structure of particle beam spills lasting 5.1 s and repeating every 16.8 s [55], which is not present in the A2 experiment using quasi-continuous photon beams. The COMPASS TCS distributes corresponding "begin-of-spill" and "end-of-spill" signals via serial optical connections to the CATCH and GeSiCa boards besides the actual internal read-out trigger. The TCS controller itself is managed by the A2 experiment trigger system, and the whole TCS subsystem is reset by a stop and start sequence issued every 10^5 events, which corresponds to roughly one minute at typical event rates. Furthermore, the various COMPASS components such as the CATCH and GeSiCa modules need a specific sequence of "begin-of-spill" and "end-of-spill" to properly initialize the FPGAs with the corresponding firmwares and register settings. For example, the firmware of the COMPASS iSADC modules is transmitted via optical links from the GeSiCa module under the precondition that the COMPASS TCS sender indicates an "end-of-spill". Before the upgrade in 2014, the system was maintained by simplistic shell scripts with long wait periods due to sequential processing and lacking state validation, which summed up to restart times on the order of 10 minutes. The initialization of the TCS was carried out manually by experts

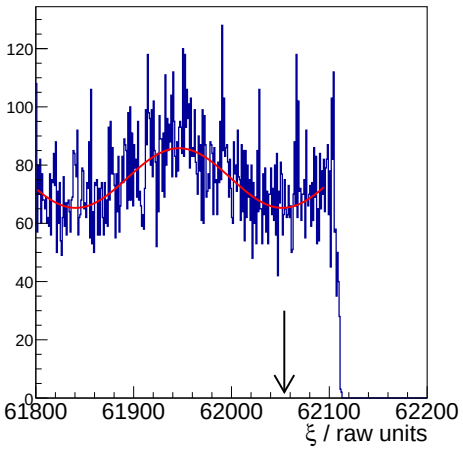

Figure 2.13.: The CATCH TDC raw value distribution is shown for the channel measuring the trigger reference timing. The black arrow indicates the wrap-around value of 62054. The fitted sine wave modulation is close to the COMPASS TCS frequency of 38.88 MHz using the conversion factor of 0.1171 ns per raw unit.

with a high probability of intermittent mistakes and retries. Accordingly, the procedures for properly handling the COMPASS system have been improved and are now fully automated by a script called "AcquManager", taking care of many failure states and properly reporting them to the user. During the development of dedicated read-out software for the GeSiCa system independent of the standard Acqu DAQ software, a readout bug in the system was discovered for high buffer occupancies in the GeSiCa module and was fixed in January 2014, see [40] for a detailed investigation. Furthermore, the whole COMPASS system is synchronized to a clock with a frequency of 38.88 MHz, which is probably the source of the still unresolved hum on the CB analog sum, deteriorating its use as a trigger signal as shown in figure 2.12. Another strange behavior is observed in the distribution of raw values read-out from the CATCH modules shown in figure 2.13. Although the correct wrap-around value is 62054 [36, 53] leading to double-peak free timing spectra, see also section 4.4 on page 73, larger raw values up to 62112 are observed. Again, the aforementioned hum is seen as a sine wave modulation yielding more evidence that the TCS clock is the source. Those shortcomings of the experimental setup, in particular concerning the COMPASS components, still exist as of now although mitigations on the software and hardware level have been tried.

Since the BaF_2 scintillation light consists of a fast and slow component, the New TAPS Electronics Card (NTEC) add-on has been developed to digitize four BaF_2 signals [56] as a mezzanine card for the CAEN V874A VMEbus board. Besides the integration over a short and a long gate each with a high- and low-sensitivity gain, a CFD for timing and two leading-edge discriminators (LEdDs) are implemented, whose outputs are also provided to the trigger system for multiplicity-based event discrimination. Moreover, a simplified version of the NTEC add-on digitizes eight TAPS Veto signals. The TAPS calorimeter was used at different experimental facilities with customized geometrical configurations. Thus, TAPS had its own stand-alone DAQ until 2013, and the remaining Acqu DAQ was coupled to it. This "coupled mode" was a permanent source of errors and decreased the efficiency of beam times tremendously. For example, restarting the coupled DAQ required manually executed commands taking up several minutes to complete with a considerable chance of failure. This makes a unified and automated readout system highly desirable. Nevertheless, since the TAPS HV is calibrated before every beam time using minimum ionizing cosmic radiation to ensure homogeneous trigger responses, at least a stand-alone run mode and analysis of calibration data is required. The installation of an FPGA based trigger system in 2012 [40, 57] played a pivotal role in order to properly integrate the TAPS system into the remaining experimental apparatus, which was finally achieved in the 2013/2014 upgrade.

In principle, most of the signal digitization is done with a variety of VMEbus modules, as shown in figures 2.10 and 2.11. The bus is controlled by a master module running a 32-bit Linux-based system, which sends the acquired data as Transmission Control Protocol (TCP) streams to the event merger. In order to improve the performance without modifying the master module, the crucial quantity to reduce is the number of VMEbus cycles needed to read out the whole system. This has been achieved for the CB and tagger section of the DAQ by splitting the backplane of each VMEbus crate into two parts, doubling the number of VMEbus master modules. Besides several other technical improvements to the DAQ, such as the introduction of Experimental Physics and Industrial Control System (EPICS) and virtualization of crucial computer systems, two key developments are presented in sections 2.6.1 and 2.6.2, which improve the stability and the performance of the whole system, respectively. Eventually, the whole DAQ is twice as fast after the upgrade, which is a substantial contribution to the η' measurement campaign leading to the analysis presented in chapter 4.

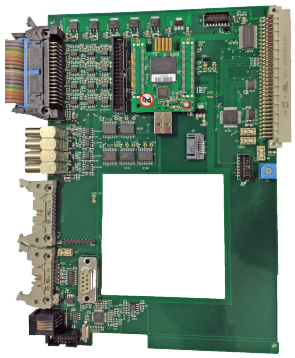

Figure 2.14.: An image of the VITEC PCB designed by Klaus Weindel, KPH electronics workshop. The FPGA is realized as a commercially available mezzanine card. The prominent hole in the PCB makes the VITEC a perfect fit for the heat-sink of the "KPH VMECPU", a simple VMEbus master module. This frees a previously blocked slot in densely packed VMEbus crates.

2.6.1. Streamlined VME readout scheme

Besides performance improvements, the upgrade also streamlined the overall readout scheme of the DAQ as follows: Each VMEbus crate including TAPS is controlled by the KPH VMECPU, which is a VMEbus master module developed by the KPH electronics workshop, in conjunction with the KPH VITEC module in figure 2.14, which is a multi-purpose input/output VMEbus slave module.

The VITEC uses a complex programmable logic device (CPLD) to communicate over VMEbus and thus provides access to an FPGA handling the NIM and Emitter-coupled logic (ECL) input/output connections. Both firmwares for the VITEC have been developed in VHSIC hardware description language (VHDL) as part of this thesis [58] including auxiliary programs and VHDL simulation test benches rendering future modifications verifiable. Furthermore, the outsourcing of the VMEbus communication to the CPLD enables the programming of the FPGA with newly developed firmwares without risking a cumbersome manual recovery via the Joint Test Action Group (JTAG) standard pin header due to malfunctioning firmware, as it is the case for the commonly used VUPROM VMEbus modules. The VITEC FPGA mainly handles the NIM communication to the trigger system via the interrupt (IRQ), acknowledge (ACK) and serial event number (EvID) NIM signals, see also figure 2.10. It indicates a rising edge on the IRQ signal via a status register

bit, which is constantly polled by the AcquDAQ instance over the VMEbus interface to start the read-out of the attached modules. The AcquDAQ instance acknowledges the IRQ signal to the trigger system by setting the ACK signal high. During read-out, the event serial number is received from the trigger system and stored by the VITEC. After all modules have been read-out by the AcquDAQ instance, the ACK is set to low, the serial event number is attached to the event and eventually transmitted to the AcquRoot event merger via Ethernet. The correct behavior of the VITEC is thoroughly scrutinized with the aforementioned test benches and described in detail in [52]. Moreover, the VITEC features an additional Arduino-compatible microprocessor to independently monitor the voltages supplied to the VMEbus modules, indicating imminent crate power supply failures.

In total, $12 + 11 = 23$ "KPH VMECPU and VITEC" compounds are responsible for the complete read-out of the CB and TAPS system, respectively, all containing a disk-less 32bit x86 single board computer (SBC) running an identical Debian GNU/Linux system, see also figure 2.10. This homogeneous computer infrastructure design enabled the development of the AcquManager script, which reduces the whole DAQ restart time from about 10 minutes to 5 seconds. Thus, the whole DAQ software is restarted completely before each run to increase stability. Restarting a run internally via the Acqu system without killing all processes is not properly distributed to all AcquDAQ instances most likely due to an incorrect implementation of the inter-process communication. This leads to inconsistent states and potential data corruption such as unsynchronized periodic slow control reads, known as scaler reads, or the loss of data from COMPASS components due to improper setup of the TCS. Although several attempts to improve this internal restart behavior of the DAQ have been made, its multi-threaded network-distributed master-slave "design" likely requires a rewrite from scratch to realize a proper fix.

2.6.2. TAPS efficient readout scheme

As already mentioned, the TAPS detector was handled until 2013 as a standalone system with its own data-acquisition software, including slow control tasks, such as HV and threshold settings. Since the existing VMEbus master modules were single-core computers, a performance gain was expected by replacing them with dual-core CPUs. However, as dedicated tests and measurements of the VMEbus readout cycle time with an oscilloscope have revealed afterwards, the performance is solely limited by the VMEbus communication cycle as shown in figure 2.15 and not by other factors, such as the CPU processing power or the Ethernet network bandwidth. Thus, the

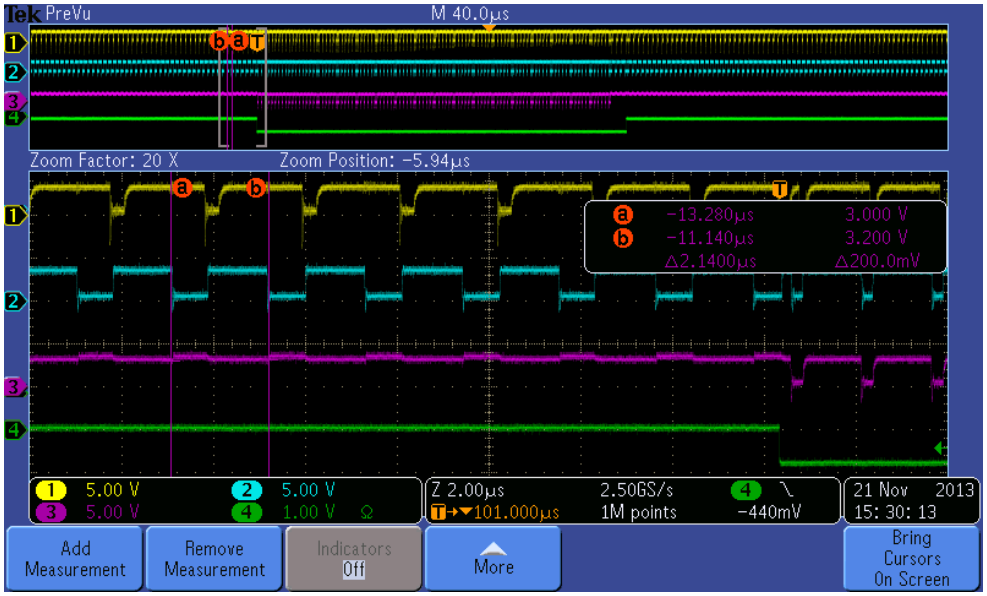

Figure 2.15.: VME timing measurement during the polling of the VITEC status registers. Channel 1 (yellow) shows the DTACK (data acknowledge) signal, channel 2 (cyan) shows the AS (address strobe) signal, channel 3 and 4 are irrelevant here. As indicated by the a/b cursors, one read cycle of the status register takes 2.14 µs. During that cycle, DTACK and AS are both high for about 40 % of the cycle time, which means that the VMEbus master spends a significant percentage with internal PCI communication during one VMEbus cycle. The length of VMEbus cycle time is currently the limiting factor for the DAQ performance.

previous employed TAPS DAQ is unexpectedly faster than the "upgraded" system with dual-core KPH VMECPUs. In fact, the KPH VMECPU consists of a single-board computer connected via the PCI 32 bit bus to a CPLD interfacing the VMEbus. The advantage of this approach is that inside the Linux operating system, the VMEbus is directly accessible via memory access within the PCI address space without any additional kernel driver module. However, the CPLD does not support block address accesses to the VMEbus and thus is rather slow in particular with NTEC modules as slaves. Furthermore, the firmware for the CPLD is rather undocumented and written in the hardware description language ABEL, hampering the reduction of the single address VMEbus access cycle time of 2 µs, of which at least 0.8 µs are spent in the

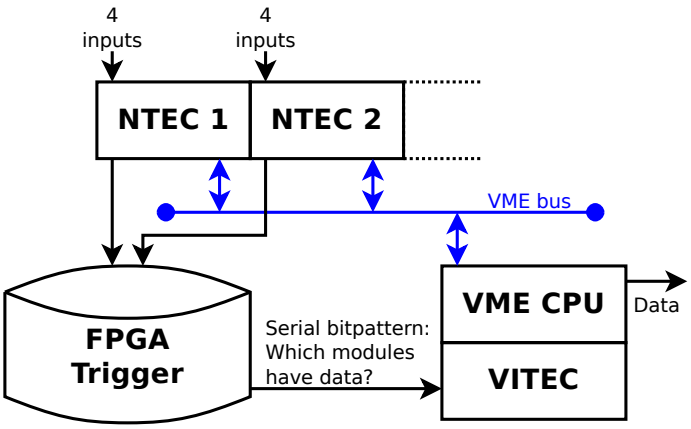

Figure 2.16.: The elements of an efficient readout scheme for the TAPS data-acquisition, called "SpeedTAPS". The NTEC transmits its hit pattern to the trigger system for multiplicity-based triggering. This information is passed on to the read-out, skipping "empty" modules and thus increasing speed.

PCI communication, as shown in figure 2.15.

Since the TAPS subsystem turned out to be the slowest part of the DAQ under typical beam conditions, the so-called SpeedTAPS technique is crucial to eventually gain a performance improvement from the whole upgrade. The basic idea is that the trigger system already knows after about 100 ns the hit pattern of each detector module, since the NTEC cards send their discriminated outputs immediately to the corresponding FPGA trigger module. This information is additionally transmitted to the KPH VMECPU as a serial bit pattern in order to reduce the number of VMEbuss accesses when reading out the modules sequentially, as depicted in figure 2.16. To this end, the FPGA firmware for the TAPS trigger system is modified to send out the occupancy for each NTEC module as a serial bit pattern to the VITEC via an additionally installed signal cable. Furthermore, the VITEC firmware is modified to provide this bit pattern to the Acqu DAQ instance, which accordingly skips the NTEC modules indicated as empty. This reduces the mean number of necessary VMEbus accesses significantly and thus the mean readout time of the TAPS system is improved from 176 µs to 56 µs. The correctness of this readout scheme has been tested in detail [52] yielding a negligible probability of less than 10^{-5} per event that some data is found in the NTEC although the corresponding bit pattern indicated an empty module. This is attributed to an incorrectly working NTEC board and is most pronounced in case of the 8 channel version for the TAPS Veto signals.

3. Hardware upgrade design studies

The existing electronics for the tagger and CB apparatus were installed in 2004 and are mostly based on hardware from the COMPASS collaboration [53], as presented in chapter 2. After over ten years in operation, a sufficient number of spare modules is not available anymore and documentation or support for those devices from the COMPASS collaboration becomes harder to obtain. Furthermore, most of the modules need firmwares for which no source code is directly available to the collaboration, which renders fixes or improvements impossible. Thus, to ensure the maintainability for the next decade of the whole DAQ system including TAPS, the replacement of existing hardware by new components fulfilling the detector requirements has become mandatory.

One important prerequisite of the feasibility studies is that an extensive custom electronics development is not feasible within the A2 collaboration, so as in 2004, existing electronics from other experiments or institutions needed to be triaged and tested. The initial search focused on a modular system with well-developed software and firmware environments due to the experiences with the existing system, which suffers from the complexity of manifold hardware components and closed-source firmwares. Of course, the anticipated system should at least meet the timing resolutions as well as linearity and dynamic ranges for energy measurements as further discussed in section 3.1, such that solely the physical properties of the detectors limit the achievable performance for A2 experiments. Eventually, the TDC readout board revision 3 (TRB3) platform fulfilled all those requirements as presented in section 3.2.

Within the scope of this thesis, the integration of the TRB3 platform into the existing A2 DAQ system and tests of different read-out approaches mostly targeted at the CB calorimeter were achieved, as presented in sections 3.3 and 3.4. In section 3.5, the future upgraded system is discussed including possible alternatives and intermediate upgrade milestones.

3.1. Experimental requirements

In total, the current A2 detector system consists of roughly 3000 channels, from which timing and integral information is digitized after typical read-out times of 150 µs, see also section 2.6. The analog signal properties of the detectors,

which crucially determine the choice of the FEE components, are summarized in table 3.1.

For a simple hit detection, as it is required for example for the tagger, a single-channel time resolution of about 1 ns is sufficient to properly correlate events. For ToF measurements, which can help to identify nucleons, a timing resolution of at least 100 ps in TAPS is desirable. The trigger signal serves as the reference for all timing measurements and is usually inferred from the analog CB sum using a low threshold close to the noise level to avoid a timing shift depending on the amplitude, the so-called time-walk. Still, this reference typically limits the achievable resolution but can be compensated by an off-line calculation of timing differences between detectors, such that the implicit trigger reference cancels. See chapter 4 for further discussion of the relevance of timing resolutions with respect to analysis.

In case of the calorimeters CB and TAPS, a linear conversion of the scintillation light output is of paramount importance to ensure a proper energy measurement of the electromagnetic shower. Of course, the linearity should cover the whole range of energy depositions, which is typically from about 1 MeV up to 400 MeV for a single crystal, which corresponds to a large dynamic range of 400. For CB, the response of the integral digitization hardware has been verified using a signal generator in figure 3.1. As the summation and pedestal subtraction is carried out digitally over a 40 MHz sampled waveform using a properly configured integration gate derived from the trigger, the non-linearity is exceptionally small. In comparison, the PID has a much lower dynamic range of about 50 and thus an analog integration becomes more feasible for this detector. For TAPS, the slow and fast component of the BaF_2 scintillation light is currently integrated over a short and long gate in parallel using dedicated analog circuits, which can be exploited to differentiate hadronic from electromagnetic showers.

In summary, modern readout hardware can easily cope with the experimental requirements for timing and integral measurements. However, the adaption of already available solutions to each of the detector requires detailed investigations and careful planning.

3.2. The TRB3 platform

The TRB3 is a $4 + 1$ FPGA multi-purpose digital electronics PCB, which was originally developed by the GSI Helmholtzzentrum für Schwerionenforschung GmbH (GSI) in Darmstadt for the high-acceptance dielectron spectrometer (HADES) collaboration [59]. Via additional mezzanine cards, so-called add-

Detector/Scintillator	Channels	t_{rise}/ns	t_{fall}/ns	Pile-up/‰
Tagger/EPT, Organic	352/47	2	10	1
CB, NaI(Tl)	672	30	400	0.4
PID, Organic	24	2	10	0.01
TAPS, BaF_2	366	2/620	20/2700	3
TAPS Veto, Organic	384	2	10	0.01
TAPS, $PbWO_4$	72	6	30	0.03

Table 3.1.: Signal properties of the main A2 detectors. The typical signal shapes are characterized by their rise- and fall-times, and usually determined by the scintillating material. The Poisson-distributed pile-up probability $1-\exp(-r(t_{\text{rise}}+t_{\text{fall}}))$ was calculated for event rates r of 1 kHz and 100 kHz for usual detectors and tagger, respectively. The MWPCs are omitted here, as their suitability for high rate experiments is questionable. Anyhow, they have similar properties as the TAPS Veto detectors.

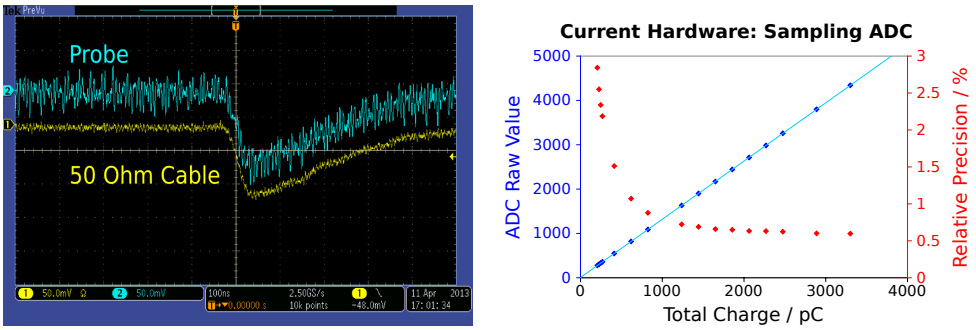

Figure 3.1.: In the left panel, a single channel CB analog signal generated by a random cosmic event is measured at the non-delayed TDC output of the analog splitter. With 100 ns/div, the typical rise- and fall-time of 30 ns and 400 ns is determined. Measuring parasitically using a high-impedance probe is difficult due to the omnipresent hum at the CB frame, see also section 2.6. The right panel shows a signal generator test measurement of the raw ADC output value using triangularly shaped pulses with different amplitudes, see also equation (3.1) on page 46. The relative precision is given by RMS over the mean.

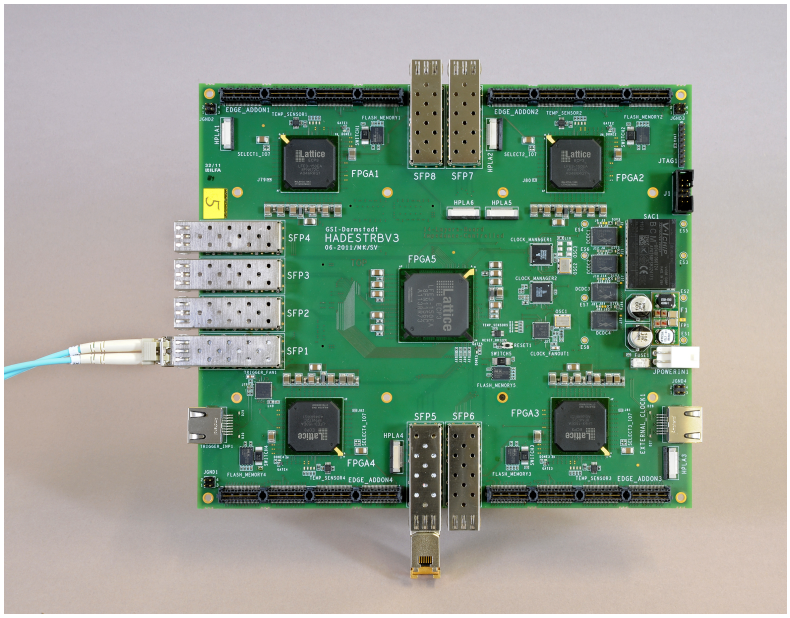

Figure 3.2.: An image of the TRB3 PCB. The central FPGA is connected to the eight on-board SFPs, and the four peripheral FPGAs communicate with customizable add-on boards via high-density connectors.

on boards, the four peripheral FPGAs are connected to various front-end electronics boards, see figure 3.2. The central FPGA acts as a data concentrator and transmits the event data stream via standard Gigabit Ethernet connection. The TRB3 user community has substantially grown beyond HADES and the board is for example one crucial component of the readout system envisaged for the anti-proton annihilations at Darmstadt (PANDA) experiment. It ships with extensive documentation [60] and was tested in several beam-times and larger setups with various front-ends [61–63].

More complex TRB3-based DAQ systems are realized by connecting multiple TRB3s with optical serial links either via the on-board SFP transceivers or via hub add-on boards providing six additional SFPs. Each FPGA is uniquely identified via hard-coded 64 bit provided by the attached one-wire temperature sensor. Using this identification, the so-called TrbNet models the FPGAs as logical endpoints within a network hierarchy. TrbNet provides convenient distribution of different trigger types, the transport of acquired data from the FPGAs and access to registers for monitoring, slow control and debugging [64–66]. It is implemented as well-structured VHDL entities and enables

external users, such as the A2 collaboration, to develop customized firmwares efficiently [61].

To access the TrbNet, one TRB3 is connected to a off-the-shelf computer via standard Gigabit Ethernet. The Internet Protocol (IP) configuration of the TRB3 is setup by Dynamic Host Configuration Protocol (DHCP) and accessed via already provided TrbNet low-level user tools, providing basic register access and in-field firmware programming. The read-out data is concentrated into one Uniform Datagram Protocol (UDP) packet per event with a maximum size of 64 kB. Furthermore, the TRB3 ships with a Central Trigger System (CTS) component implemented on the central FPGA, which controls the triggered read-out of all front-ends and can be conveniently configured via a responsive web-based graphical user interface (GUI) [67]. This makes the TRB3 suitable for table-top experiments such as front-end test environments as well as for large-scale production detector systems.

Typically, the peripheral FPGAs are used as TDCs for discriminated digital signals, as the acronym TRB3 already indicates. The TDCs are realized using the tapped delay-line method [68], which exploits the physical propagation time of the electrical signals inside the FPGA. Up to $64 + 1$ TDC channels are implemented with channel-to-channel resolutions in the order of 10 ps [69]. This is two orders of magnitude better than the coarse counting resolution of $5\,\text{ns}/\sqrt{12} \approx 1.4\,\text{ns}$ RMS using a simple 200 MHz digital clock counter. The currently provided firmware is adaptable to different user requirements, such as leading and trailing edge measurements in one channel or internal stretching of very short signals, and thus ready-to-use for many applications [70]. However, the asynchronous delay-lines are realized as digital adder carry-chains inside FPGA slices and hence need a temperature-dependent calibration, which assigns to each segment of the delay line a physical propagation time. To obtain this calibration, each TDC channel needs to be fed with uncorrelated signals with respect to the coarse counting clock. Otherwise, the likelihood that the incoming hit stops in a certain delay bin is not uniformly distributed, which spoils the statistical treatment of this problem. If those uncorrelated hits are not provided directly by the attached detector system, which is in particular the case for reference timings needed to synchronize channels across FPGAs, the insertion of hits from an uncorrelated clock source is required. This is already realized by artificial TDC calibration events within the TRB3 CTS.

The last component of the TRB3 platform is the versatile event builder called Data-Acquisition Backbone Core (DABC) [71–74] amended by the flexible ROOT-based analysis framework Go4 [75]. DABC merges the data streams from multiple input sources, such as TRB3s or EPICS slow control, into one

HADES list mode data (HLD) stream [76, 77], which is eventually written to disk or transported to on-line processing Go4 instances. Additionally, it provides low-level analysis routines such as the TDC delay-line calibration. Within the scope of this thesis, a simple stand-alone unpacker has been developed [78] using the conventional HADES event builder "hadaq" but was later replaced by the DABC/Go4 system. Furthermore, specific analysis components for the TRB3 ADC add-on presented in section 3.4 have been integrated into the so-called Stream library as part of the Go4 framework.

To integrate a TRB3 subsystem into the AcquRoot-based A2 DAQ as shown figure 3.3, two goals were successfully achieved: First, the experiment reference timing and a 16 bit serial ID provided by the A2 trigger system [40] as NIM signals are fed into the TRB3 event stream. This led to the development of an additional module for the TRB3 CTS, which is already merged into the TRB3 VHDL source repository. Second, the TRB3 UDP packets are processed by a customized AcquDAQ instance with TRB3 software modules and subsequently transmitted to the A2 event merger. The necessary modifications to the A2 Acqu ecosystem are available in the "trb" branch of the author's repository [79]. Other possible integration schemes will be discussed in section 3.5.

3.3. Charge-to-time conversion front-end PaDiWa AMPS

Since the TRB3 is equipped with a mature TDC firmware for the peripheral FPGAs, it appears convenient to convert any relevant detector information, such as integrals or timings, into logical signals which are then digitized by the TDC. The PANDA DIRC WASA (PaDiWa) front-end family was developed by GSI following the COME&KISS concept [80], which promotes the usage of readily available commercial elements (COME), such as FPGAs, and keeping the remaining parts simple and sound, or stupid (KISS). For example, the LVDS input buffers of a Lattice MachXO FPGA are mis-used as a leading-edge discriminator as follows: The (possibly amplified) analog input V_{in} is applied to the positive input of the differential buffer and a variable threshold voltage V_{thr} generated by the FPGA with PWM to the corresponding negative input. If the difference $V_{\mathrm{thr}} - V_{\mathrm{in}}$ reaches the transition region of the input buffer, the digital output signal becomes metastable. The resulting noise causes hit rates in the order of 10 MHz in the corresponding TDC channel. Assuming that no detector hits arrive and thus V_{in} stays at the constant baseline voltage, the threshold reference value $V_{\mathrm{thr}}^{\mathrm{ref}}$ to which the input signals are relatively discriminated is thus determined by searching the maximum

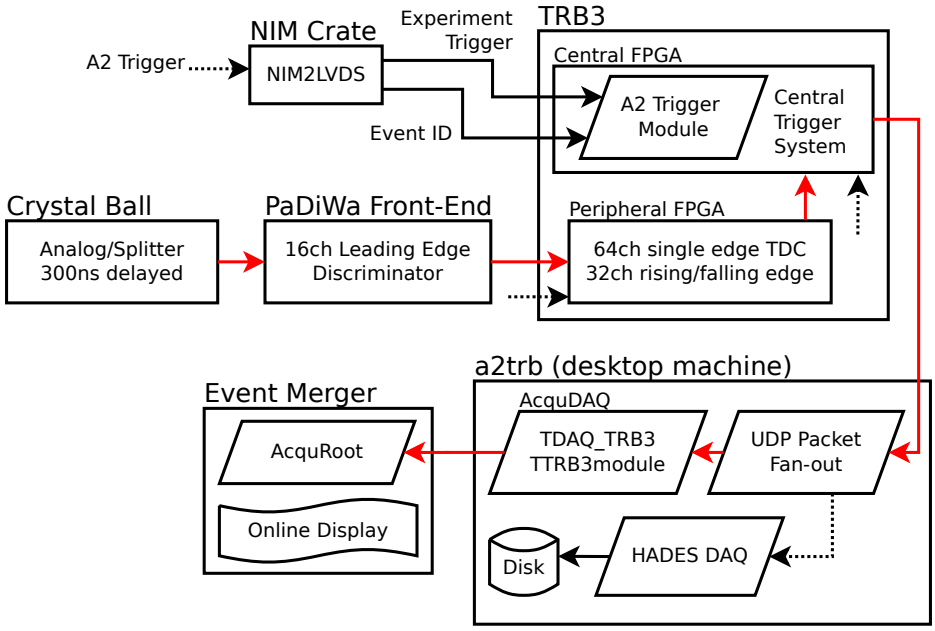

Figure 3.3.: TRB3 DAQ integration as used for test measurements, here shown for a PaDiWa board attached to the CB analog-splitter, see section 3.3 and figure 2.11 on page 29. The A2 trigger system provides the reference timing and the Event ID for each event. The signal data flow, as shown by red arrows, is eventually sent via network to the AcquRoot event merger.

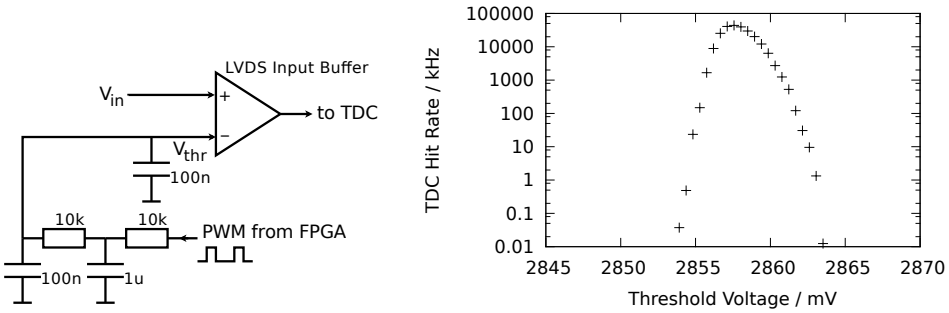

Figure 3.4.: The left panel shows how the FPGA LVDS input buffer is used as a discriminator for the signal V_{in}. The threshold voltage V_{thr} is generated by the FPGA as well using a low-pass filtered PWM signal. The right panel shows a scanning measurement of the TDC hit rate for different settings of V_{thr}. The maximum hit rate is found at $V_{\mathrm{thr}} \approx 2858\,\mathrm{mV}$, which is then used as the reference $V_{\mathrm{thr}}^{\mathrm{ref}}$.

TDC hit rate with respect to V_{thr}. This is depicted in figure 3.4. Since the exact value of $V_{\mathrm{thr}}^{\mathrm{ref}}$ depends on the FPGA input buffer and the input baseline voltage, this procedure is automated by auxiliary scripts. Temperature drifts of those relative thresholds can be reduced to negligible extent within the FPGA firmware. For example, time-over-threshold (ToT) measurements vary with roughly 10 ps/K after compensation [81], which is on the order of the timing resolution and thus negligible with respect to ToT lengths of about 10 ns. Typically, the 16 channel PaDiWa leading edge discriminator achieves channel-to-channel timing resolutions of 23 ps RMS in conjunction with TRB3 TDCs [82], which is a remarkable achievement regarding the "unspecified use" of FPGA resources.

Due to the good performance and cost-effectiveness of the PaDiWa discriminator board, an 8 channel integrator board PaDiWa AMPS was developed by Wolfgang Koenig, GSI, for the HADES electromagnetic calorimeter using the COME&KISS concept [83–85]. It is based on a modified Wilkinson ADC circuit with active discharge to achieve high hit rate capability. The functional principle is also discussed in [86] as dual-slope integration. Similar to Wilkinson's original idea, the charge information of the input signal is converted into a time interval by using an integration capacitor, which is subsequently measured by the TRB3 TDC. The leading edge timing of the input signal is obtained similarly to the PaDiWa discriminator board. Again, the Lattice MachXO FPGA discriminates the SLOW and FAST output signals from the

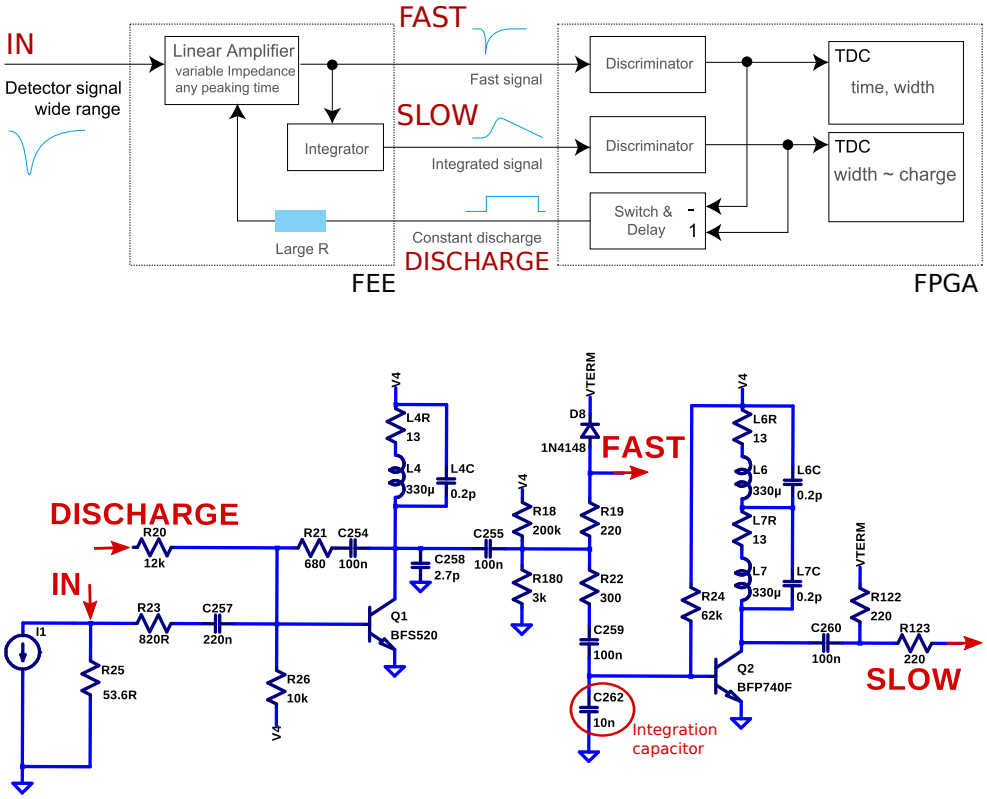

Figure 3.5.: PaDiWa AMPS building blocks, adapted from [83], and the FEE schematic developed by Wolfgang Koenig, GSI, as implemented in LTSpice. The integration time is mainly determined by the indicated capacitor `C262`. The two TDC channels to measure the FAST and SLOW signal timings are implemented on the peripheral TRB3 FPGA.

analog circuit, and generates an asynchronously delayed DISCHARGE signal from FAST, as shown in figure 3.5.

Since the integration capacitor[1] is discharged with a constant current, the ToT of the SLOW output is proportional to the input charge. However, as the leading edge of SLOW arrives slightly earlier for higher input amplitudes, an effect commonly referred to as time-walk, the ToT linearity is improved by measuring the leading edge of the FAST signal as well. Furthermore, an active DISCHARGE is generated by the FPGA from an asynchronously delayed FAST by charging an external capacitor and discriminating its voltage via an input buffer with constant reference voltage. The length of the delay is adjusted by the drive strength of the output pin, which can be specified during firmware building. Due to this DISCHARGE feedback from the FAST, $V_{\text{thr}}^{\text{ref}}$ is first determined for SLOW while FAST is disabled and, after setting the relative threshold for SLOW, $V_{\text{thr}}^{\text{ref}}$ is determined for FAST and its relative threshold can be set.

The PaDiWa AMPS FEE is designed for input signals with 10 %-90 % rise- and fall-times of roughly 5 ns and 15 ns, respectively. The voltage range of the input signal is designed as 25 mV to 5000 mV. The corresponding input charges reads, using the approximation of a triangular pulse shape with voltage amplitude A,

$$Q = \int I dt = \frac{A}{50\,\Omega} \frac{1}{90\,\% - 10\,\%} \frac{5\,\text{ns} + 15\,\text{ns}}{2} = 0.25\,\text{pC/mV} \cdot A\,, \tag{3.1}$$

with the input termination of 50 Ω. Thus, the dynamic range is designed as 6.25 pC to 1250 pC. This design was successfully tested with a lead glass prototype of the HADES ECAL detector [83, 85] and different PMT types at the A2 photon beam line.

Within the scope of this thesis, a LTspice IV [87] simulation was developed [79] and validated using a signal generator test setup, see figure 3.6. Typical timings and amplitudes were reproduced with 10 % accuracy, supposedly limited by nominal value variations of certain components, such as capacitors, and the increased PCB temperature of about 50 °C during test. This served as a model to explore the possible modifications needed for the signal properties of CB NaI crystals, which are characterized by typical 10 %-90 % rise- and fall-times of 30 ns and 400 ns, respectively, and thus an order of magnitude slower than suitable pulses for the current PaDiWa AMPS design. Furthermore, the dynamic range of the current A2 readout system based on a 40 MHz sampling ADC is roughly twice as large with an excellent linearity due to the different

[1] `C262` in figure 3.5.

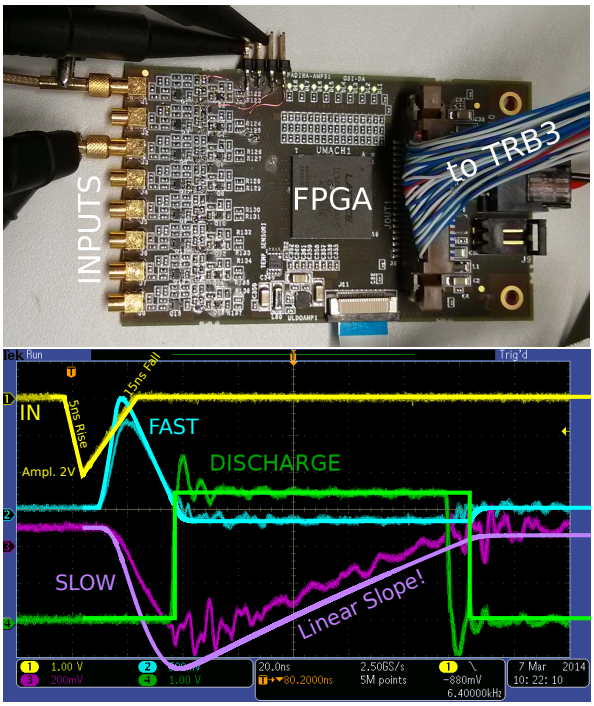

Figure 3.6.: PaDiWa AMPS LTspice simulation verification. The photography on top shows the 8-channel PCB under test including custom modification to tap different analog signal lines. The bottom panel shows a screen-shot from the oscilloscope with simulated signals scaled in xy according to the input signal only. The DISCHARGE is simulated as too long since the SLOW signal is estimated too high. The distortions are caused by the stray capacitance of the attached oscilloscope probe if the DISCHARGE signal is measured. Horizontal scale is 20 ns/div, vertical scales differ for each signal.

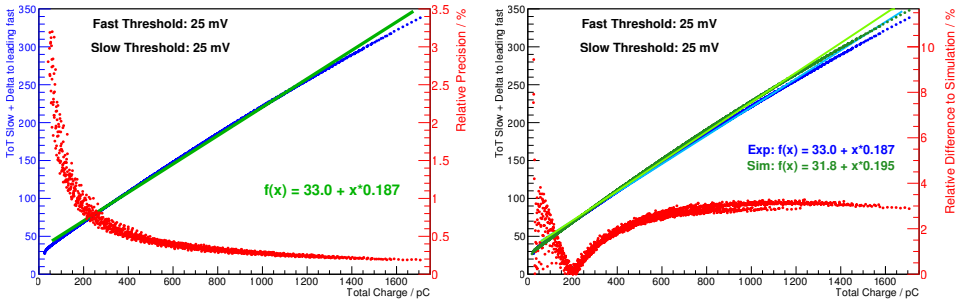

Figure 3.7.: The PaDiWa AMPS circuit time interval output against the total input charge. The rise- and fall-times were varied from 5 ns to 14 ns and from 10 ns to 25 ns, respectively, and the amplitude from 0.1 V to 3.5 V. For each measurement, the mean of the total charge according to equation (3.1) on page 46 and the RMS over the mean as the relative precision are shown in the left panel. Those measurements are then compared to the LTspice simulations in the right panel. Furthermore, a linear fit is shown to asses the non-linearity of the charge measurement. Compared to the measurement of the existing system in figure 3.1, the linearity is insufficient.

measurement technique. Figure 3.7 shows that without major modifications of the analog circuit design, the linearity and the dynamic range of the current system as given in section 3.1 cannot be achieved. Moreover, a new sampling ADC add-on became available at the same time which conceptually does not suffer from such non-linearities, as shown in section 3.4. Thus, the PaDiWa AMPS was discarded as a possible upgrade option for the CB calorimeter. Nevertheless, it is still an attractive component for other parts of the A2 detector system, as further explained in section 3.5.

3.4. Sampling ADC firmware development and measurements

In 2014, the GSI electronics workshop designed a 48 channel sampling ADC add-on on behalf of a Portuguese group for the readout of resistive plate chambers (RPCs) [88, 89]. Concerning the firmware, this required a configurable finite impulse response filter with baseline subtraction and triggered readout. The add-on is based on 12 quad-channel AD9219 integrated circuits (ICs) with 10 bit resolution and up to 65 MHz sampling rate. To simplify firmware development,

the sampling rate was set to 40 MHz since for this choice the double-data-rate (DDR) serializer-deserializer (SERDES) output matches the 100 MHz system-wide TrbNet clock avoiding clock domain crossing (CDC) issues. This can be seen as follows: At 40 MHz sampling rate, the AD9219 outputs 4 channel bit streams (DCO) and 1 common frame bit stream (FCO) with a DDR rate of 200 MHz. Those $(4 + 1) \cdot 2 \cdot 200 = 2000$ Mbit/s are output by the SERDES as 20 bit parallel at 100 MHz, which matches the standard TrbNet system clock domain. If there is a clock mismatch, additional FPGA resources such as first-in first-out buffers (FIFOs) are typically required to transfer parallel buses from one clock domain to the other. This usually results in a complete redesign of the firmware if CDCs have not been adequately anticipated during development.

Initially, the write-only Serial Peripheral Interface (SPI) communication to the ADC and clock distribution ICs was successfully established to setup the correct phase alignments using the test pattern mode of the ADC. To this end, the auxiliary MachXO FPGA was programmed as a SPI multiplexer and scripts to automate the startup have been developed within the scope of this thesis. Subsequently, the work focused on the development of a feature extraction firmware as additional VHDL entities, providing timing and integral information. First, modifications to the existing firmware were made in order to test if a timing accuracy of a few hundred picoseconds can be achieved with a sampling period of 25 ns. Although the digital constant fraction discriminator technique with linear interpolation is already employed successfully in many read-out systems, see for example [90], it was unclear if the 2 or 3 digitized samples of the 30 ns CB signal leading edge are sufficient to achieve a satisfactory timing resolution, assuming a minimum specified sampling period of $T_{\text{sampling}} = (65\,\text{MHz})^{-1} \approx 15\,\text{ns}$.

Signal generator tests of the modified firmware eventually showed a sufficient channel-to-channel resolution of about 300 ps RMS and motivated within the scope of this thesis the development of a fully customizable feature extraction firmware for the ADC add-on, see figure 3.8. The key component is a free-running digital CFD extracting the timing information of signals above threshold. The various TrbNet slow control registers, such as the constant fraction given by the two multipliers or the delay in number of samples, are modeled in extensible markup language (XML) and are conveniently configured via an interface inside a web-browser. However, the FPGA firmware does not calculate the linear interpolation but rather sends the sample before and after the detected zero-crossing of the CFD signal to the unpacker, which subsequently calculates the fine timing by linear interpolation. This circumvents the demanding implementation of pipelined non-integer arith-

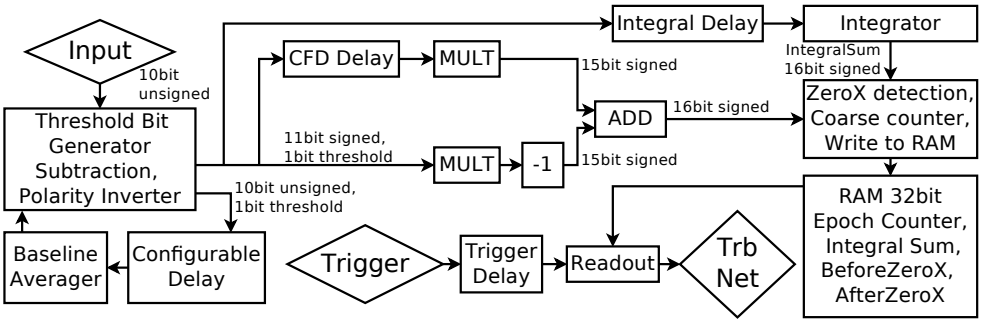

Figure 3.8.: The TRB3 ADC feature extraction firmware receives the 10 bit ADC samples from the SERDES and removes the offset with a digital baseline follower. Next, the signals are split, one path is delayed and then both are multiplied and subtracted from each other to obtain the CFD signal. If a zero-crossing is detected, an event consisting of the CFD sample before and after the zero-crossing, the integral and the epoch counter is queued into the buffer and passed to TrbNet if a readout trigger was received.

metics in an FPGA. With the addition of a coarse counter, this approach already provides a channel-to-channel timing measurement with sub-sampling resolution of about $1\,\mathrm{ns} \ll 15\,\mathrm{ns} = T_{\mathrm{sampling}}$ within the same phase-locked loop (PLL) clock domain, for example one TRB3. Moreover, a baseline follower constantly averages over the delayed input samples unless the input is not above a user-configured threshold. This average is subsequently subtracted from the input values in order to make the threshold relative to the input baseline.

At this stage of the project, systematic test measurements with a signal generator revealed a double-peak structure in the relative timings between two channels with $f_{\mathrm{sampling}} = 64\,\mathrm{MHz}$ sampling frequency and $t_{\mathrm{rise}} = 30\,\mathrm{ns}$ rise-time of the input signal, as shown in the upper panel of figure 3.9. This double-peak was most pronounced if the delay between the two identical input signals was a half-integer multiple of the sampling period and vanished for full-integer multiples. This effect is explained qualitatively with the Nyquist criterion, limiting the maximum resolvable sinusoidal frequency component to $f_{\mathrm{sampling}}/2$. Apparently, the criterion is not met for the input signal with frequency components of roughly $t_{\mathrm{rise}}^{-1} \approx 33\,\mathrm{MHz}$. The double-peak structure was subsequently confirmed by simulations taking into account the jitter between the sampling clock and the input signal besides the digitization noise. This led to the choice of $f_{\mathrm{sampling}} = 80\,\mathrm{MHz}$ for further measurements, which

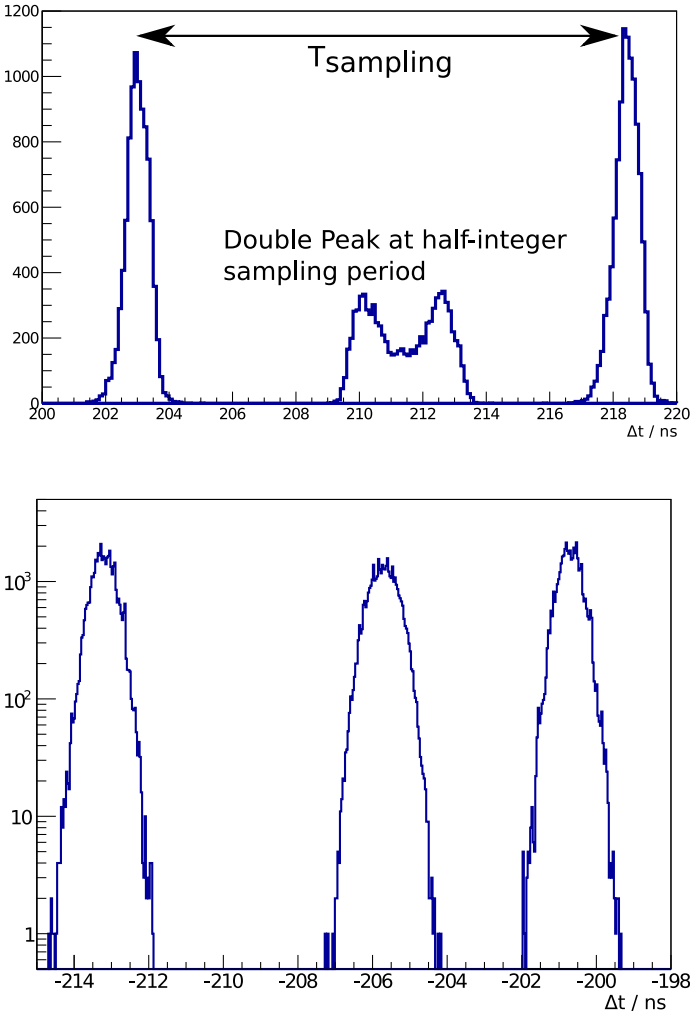

Figure 3.9.: The measured timing difference Δt between two ADC channels is shown for three different delays set by a signal generator (amplitude, rise- and fall-time chosen to match CB signal shape). In the upper panel, the two undistorted Gaussian peaks with $\sigma \approx 0.3\,\mathrm{ns}$ are separated by $T_{\mathrm{sampling}} = f_{\mathrm{sampling}}^{-1} = (64\,\mathrm{MHz})^{-1} \approx 16\,\mathrm{ns}$ delay difference. In between those two undistorted peak, with about $8\,\mathrm{ns} \approx T_{\mathrm{sampling}}/2$ change in delay, a double-peak structure is observed which spoils a proper timing measurement for typical CB signals. In the lower panel, the same measurement is repeated with a different firmware running at $T_{\mathrm{sampling}} = f_{\mathrm{sampling}}^{-1} = (80\,\mathrm{MHz})^{-1} = 12.5\,\mathrm{ns}$, where no double-peak structure is present.

shows no double-peak, see the lower panel of figure 3.9. This setting for the sampling frequency is above the AD9219 maximum specification of 65 MHz but fulfills the Nyquist criterion and additionally simplifies static timing analysis issues due to CDC in the SERDES.

To measure timings relative to an external trigger as required by the A2 detector system, its phase to the TRB3 clock is measured by a TDC in the central FPGA, which has been already implemented for the PaDiWa (AMPS) tests in section 3.3. The synchronous trigger is then sent to the peripheral FPGA, where it is synchronized to the ADC sampling frequency clock. Again, its phase is measured by a TDC in the peripheral FPGA. This procedure is depicted in figure 3.10.

The finally developed firmware including a 1-channel TDC required carefully chosen placement constraints and occupied already 60 % of the available FPGA resources. Furthermore, 3 of 12 ADC ICs could not be used at all, since some of the SERDES pins were deprecated in Lattice software revisions newer than 2.1 due to noise issues, which has not been foreseen during the PCB design of the TRB3, and the necessary TDC implementation is incompatible with the Lattice software revision 2.1. To overcome this limitation of 36 usable ADC channels per add-on, the so-called TRB3sc could be used, see section 3.5.

Eventually, a TRB3 setup with one ADC add-on connected to an off-the-shelf personal computer has been tested under beam time conditions during the Compton production run in June 2015. To carry-out a non-invasive parallel measurement during beam time, one half of a 32 channel CB analog splitter is modified by the KPH electronics workshop. The 16 differential inputs, directly connected to the 124 Ω transmission lines of the CB PMTs, are tapped and provided as suitable differential outputs to the TRB3 ADC add-on board. Due the aforementioned TRB3 PCB design bug, only 36 channels on the ADC add-on are usable, which finally results in 12 available channels for this measurement. All those 12 channels are configured identically and the data from the TRB3 is not directly merged into the Acqu DAQ to avoid affecting the normal data-taking.

Since the measurement is carried out in parallel with the existing Acqu DAQ, the timing and integral information from both DAQs is compared event-by-event using the event serial number. To this end, the 12 logical channels under test are mapped to Acqu's ADC and TDC numbering scheme using cosmic events for low hit rates and comparing hit outputs manually, see table 3.2. Using this fixed mapping, the data from typical beam time conditions with about 1.5 kHz event rate are analyzed. Under those conditions, the read-out of the TRB3 has worked flawlessly for over 6 hours with average read-out times of 10 µs per event, which is 10 times faster than the average read-out time of

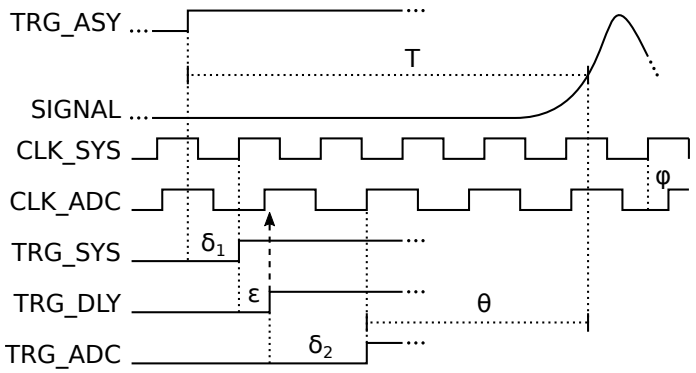

Figure 3.10.: TRB3 ADC timing measurement $T' = T - \epsilon = \delta_1 + \delta_2 + \theta$ of `SIGNAL` to an external asynchronous trigger `TRG_ASY`. The system clock and the ADC clock domain are denoted by `CLK_SYS` and `CLK_ADC`, respectively, whose phase ϕ is fixed by a PLL. `TRG_ASY` is synchronized as `TRG_SYS`, then propagated to the peripheral FPGA as `TRG_DLY`, and again synchronized as `TRG_ADC`. The necessary phases δ_1 and δ_2 measured by TDCs in the CTS and in the peripheral ADC firmware, respectively. θ is determined by interpolation. Since the propagation delay ϵ from the central to the peripheral FPGA is unknown but constant, measuring T' is equivalent to T up to an offset, which can be accounted for by calibration.

TRB3		Acqu		CB Element
Logical	Input	ADC	TDC	
0 – 3	8 – 11	3379 – 3376	2404 – 2407	372 – 375
4 – 7	24 – 27	3371 – 3368	2412 – 2415	380 – 383
8 – 11	28 – 31	3375 – 3372	2408 – 2411	376 – 379

Table 3.2.: TRB3 ADC Acqu channel mapping manually determined from cosmics data via event-by-event correlation. The Acqu ADC and TDC numbers are the channels in raw "Mk2" data format, the CB element number refers to the standard numbering scheme of logical channels.

the Acqu system. Thus, since adding more add-on boards to the TRB3 system does not increase the read-out time significantly due to its parallelized event building concept, the expected performance of a TRB3-based system is an order of magnitude better than the current DAQ. Using the experience from the signal generator tests, the constant fraction is set to 2/3 and the delay to 2 samples. The integration window is 60 samples, which corresponds to 750 ns at 12.5 ns sampling period. The input threshold is reduced from the rather conservative 15 ADC units, corresponding to roughly 30 mV, to 3 and 5 units, corresponding to 6 mV and 10 mV, respectively, after a feedback-lock issue in the baseline follower has been fixed and its average length was set to $2^{14} \approx 16000$ input samples.

The promising results are shown for one selected channel in figure 3.11. For each event, the timing and integral information from the Acqu and the TRB3 system is available and shown as correlation plots. The timing resolution is apparently determined by the analog signal quality, since additional measurements with a signal generator and typical pulse shapes showed resolutions of 200 ps RMS for the TRB3 setup. The COMPASS $\mathcal{F}1$ TDC ASICs of the existing system have a fixed bin width of 117.1 ps, yielding potential timing resolutions well below 100 ps under ideal conditions with sufficiently fast leading edges of the analog signal. This measurement here showed single channel timing resolutions of 4 ns RMS for both systems, see figure 3.12. This is significantly worse than the expected rule-of-thumb resolution of $t_{\text{rise}}/100 = 300$ ps but still sufficient to correlate the Poisson-distributed events with an average event distance of 100 µs. Concerning the integral measurements, the performance of the existing system based on 40 MHz sampling ADCs has been nicely reproduced as expected. The negligible deviation from a perfect event-by-event correlation of the two systems for the integral measurements has two causes: First, the threshold settings were hard to match exactly, which determine what actually is recorded as a timing and/or an integral measurement according to the two systems. For example, the Acqu system discards the triggered integral measurement if the pedestal subtracted integration is less than 15 raw units, which corresponds to an energy of 1 MeV, and a basically un-triggered timing measurement is recorded if the leading-edge discrimination threshold of 25 mV is passed, whereas the free-running TRB3 system stores a combined integral and timing measurement in its event buffer if the leading edge crosses the configured threshold. Second, the read-out for the integral values is explicitly triggered in the Acqu system but self-triggered in the TRB3 system, which can lead to multiple integral values in the TRB3 without corresponding values from the Acqu system. Similar results were obtained for the other 11 channels, but are not shown here for brevity. Further steps in the development for the

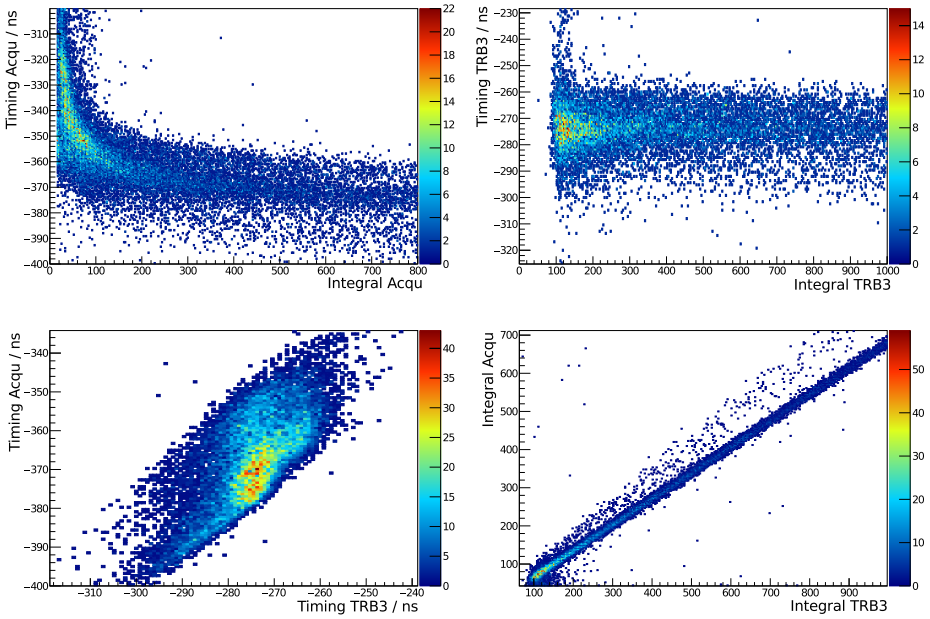

Figure 3.11.: The top row shows the timing versus their integral measured by the existing Acqu system and the TRB3 system, respectively. Since the Acqu system has a LEdD, a shift towards later timings for lower integrals is observed, the so-called time-walk. This effect is not present for the CFD based TRB3 system. The bottom row shows the timing and integral event-by-event correlation, respectively. As expected, the timing correlation is distorted due to time-walk. See text for discussion of deviations from perfect correlation for the integral measurement.

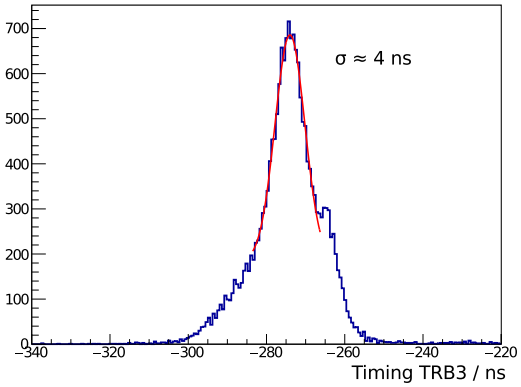

Figure 3.12.: The TRB3 timing hits as a projection from figure 3.11. The shown Gaussian plus constant fit obtained a resolution of $\sigma \approx 4\,\mathrm{ns}$. The peak distortion can probably attributed to the non-ideal analog signal quality. Note that typical analysis timing resolution would be better as they are usually taken from properly reconstructed events.

sampling ADC firmware are discussed in section 3.5.

3.5. Summary and outlook

The test beam time in June 2015 has successfully shown that the ADC add-on is well-suited for an upgrade of the CB calorimeter readout, in contrast to the PaDiWa AMPS FEE. Many technical issues have been resolved, a highly configurable and flexible firmware has been designed and a complete software tool-chain is available to investigate the TRB3 ADC add-on as well as the PaDiWa discriminator boards. Furthermore, based on the LTspice simulations, the adaptations for PaDiWa AMPS to suit A2 detectors can be easily tested.

In the following, reasonable follow-up work based on the already achieved feasibility studies is presented. Possible alternatives are also highlighted, which are complementary to the currently available solutions. Due to lack of manpower, the issues mentioned in the following have not been resolved to date and thus statements should be taken with a grain of salt, as hardware development efforts are particularly good for a surprise, as shown in figure 3.9 on page 51.

The TRB3 has been successfully evaluated as a future-proof platform for

Detector	FEE	TRB3 firmware
CB	Splitter/ADC	ADC feature extraction
PID	PaDiWa AMPS	TDC
MWPCs	PaDiWa AMPS	TDC
Tagger	PaDiWa discriminator	TDC
TAPS	Improved VME?	

Table 3.3.: The possible TRB3 upgrade options for different parts of the A2 detector system. For all detectors except TAPS, the TRB3 platform already provides ready-to-use solutions.

the A2 experiment. As summarized in table 3.3, many already developed components from the TRB3 community can be directly deployed at the various detectors, leaving only TAPS as the major challenge. For TAPS, the already installed NTEC modules are actually well-fitted for the BaF_2 crystals including the Vetos, whereas the read-out for the $PbWO_4$ is still an ad-hoc solution based on CAEN VMEbus modules, limiting their current usefulness in subsequent analysis. Since the currently deployed VMEbus master module developed by KPH supports only single address access reads but not the faster block transfer modes, a custom developed VMEbus master module with an FPGA connected directly to all VMEbus signals could achieve an optimal control over all timings and thus maximum read-out performance. Furthermore, the FPGA could run VMEbus machine code to execute loops and conditional reads or writes to directly build data packets of each event. Such a development could also profit from the TRB3 VHDL code base, for example by the Gigabit Ethernet components providing a minimalistic DHCP client implementation.

However, a reasonable upgrade project plan should considerably take into account the limited manpower for such an undertaking. One could be tempted to upgrade only parts of the system, but this might quickly lead to the undesirable situation of having to maintain a inhomogeneous system consisting of Acqu and TRB3 parts coupled to each other. Unfortunately, the current Acqu system exhibits a rather monolithic design and, additionally, takes over a lot of slow control tasks, such as threshold settings, which must be separated more cleanly before a proper integration of the TRB3 can be initiated. Otherwise, the problems solved with the streamlined upgrade in October 2013, as explained in section 2.6, will most likely appear again, eventually leading to extended beam-time losses and increased maintenance requirements, as there is no expert person knowing all parts of a certainly more complicated coupled

system with sufficient detail. One primary goal should be to replace the existing COMPASS components, affecting the CB, PID, Tagger and MWPC detectors. This would remove the remaining hassles of the rather complicated and unreliable initialization of the COMPASS TCS optical trigger distribution system. Moreover, if the read-out was changed from the current strongly coupled AcquDAQ/AcquRoot with manual handshake TCP streams to a system simply transmitting UDP packets for each interrupt signal, this could ease incremental upgrades of the system.

The development for the ADC add-on has concentrated on the a highly configurable firmware, which serves as a proof-of-principle under the specific circumstances at the CB calorimeter. However, deploying the current firmware as-is with a sufficient number of TRB3s as an replacement for the existing COMPASS GeSiCa system would be premature. For example, the time measurement showed a so-far unexplained glitch of the epoch counter, which has been fixed later in the analysis by manually adding one sampling period depending on δ_2 defined in figure 3.10. Additionally, the SPI communication and the related automatic phase adjustment of the serial LVDS transmission should be implemented directly in the peripheral FPGA, which is a prerequisite for seamless operation after power-loss or reboot of the DAQ. An alternative approach for the timing measurement sends the external trigger asynchronously to the peripheral FPGA and measures its phase with a TDC running at the ADC sampling clock. However, this requires larger modifications to the currently available TDC design, in particular a longer delay chain, which needs careful placement inside the FPGA and might even be impossible to realize due to size constraints.

Over the last years of A2-focused hardware development, the TRB3 community provided valuable support in bug-fixing and helpful auxiliary components. For example, a wrong supply voltage for the ADC ICs has been identified recently. This aspect should not be underestimated in a collaboration suffering from lack of manpower for such tasks. In particular, the so-called TRB3sc, a crate-compatible single-FPGA version of the TRB3, has been developed supporting existing add-ons. This board should be preferred over the TRB3 especially for the ADC add-on in order to leverage all 48 channels.

In conclusion, a successful upgrade is still a long-term challenge taking into account the constraints given by the planned beam-times and existing hardware. Within the scope of this thesis, the momentum of the presented proof-of-principle developments have not finally led to relevant changes in the current DAQ, although they are certainly needed for a reliable and high-performance system prepared for challenges of the next decade.

4. Analysis of the $\eta' \to \omega\gamma$ branching fraction

This chapter presents the analysis of the branching fraction of the $\eta' \to \omega\gamma$ decay relative to the reference channel $\eta' \to \gamma\gamma$. The analyzed dataset has been taken with the A2 experimental setup as described in chapter 2 from end of July 2014 until end of December 2014. As this dataset is also used in [91–94], common efforts such as the reconstruction and calibration presented in sections 4.3 and 4.4 are shared among those theses.

The branching fraction of the $PV\gamma$ decay $\eta' \to \omega\gamma$ serves as an input and verification for chiral effective field theories. As detailed in section 1.3, the implementation of heavier degrees of freedom, such as the ω vector meson, and the mixing of the singlet and octet states η_1 and η_8 into the physical states η and η' are covered by this decay. In particular, the understanding of such non-perturbative effects on the level of a few percent is a topic of current research, which motivates the analysis of $\eta' \to \omega\gamma$ and other related decays such as $\omega \to \eta\gamma$ [91] or $\eta' \to \eta\pi^0\pi^0$ [95] with similar or better precision.

4.1. Introduction to photo-production experiments

The photon beam generated by electrons radiating bremsstrahlung impinges on the liquid hydrogen target and produces strongly interacting particles, whose subsequent decays are analyzed with the A2 detector system. The total photo-production cross section off the proton is depicted in figure 4.1, including the contribution of relevant single meson channels. As shown, the EPT covers photon energies E_γ ideally suited to study the η' meson at its production threshold, given by

$$E_\gamma^{\text{threshold } \eta'} = \frac{m_{\eta'}(m_{\eta'} + 2m_\text{p})}{2m_\text{p}} \approx 1447\,\text{MeV}\,, \tag{4.1}$$

where $m_{\eta'} \approx 958\,\text{MeV}$ and $m_\text{p} \approx 938\,\text{MeV}$ are the rest mass of the η' and proton, respectively. The η' production threshold is close to but still sufficiently below the MAMI C maximum electron beam energy of 1604 MeV.

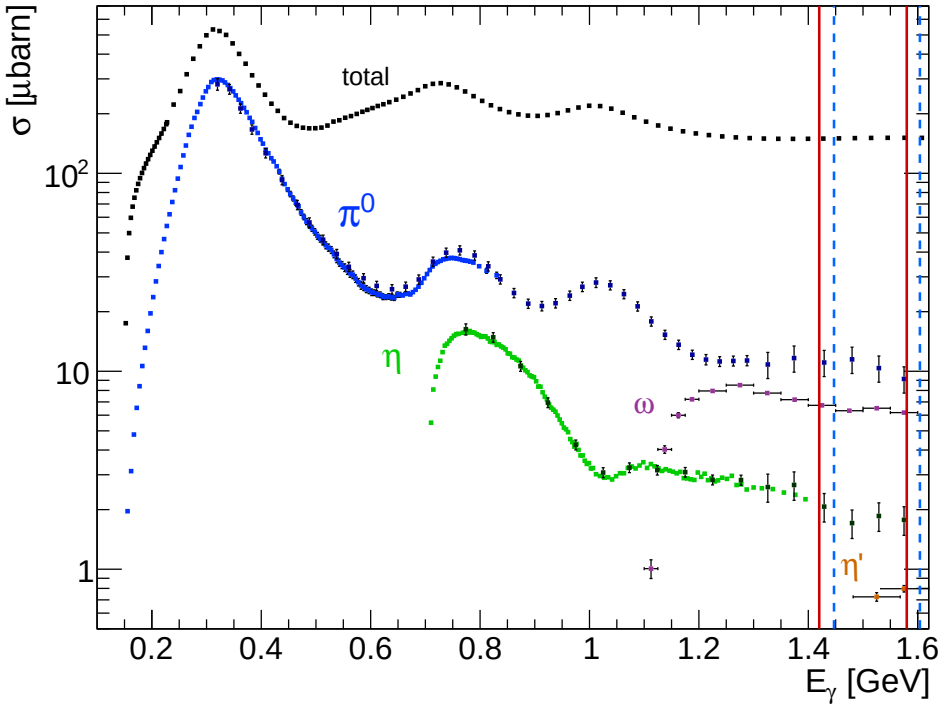

Figure 4.1.: The total photo-production cross-section off the proton is shown including some single meson production channels, from [96]. The data points from previous experiments, carried out mostly at A2 in Mainz and CB/ELSA in Bonn, are amended by model predictions shown in color. The solid red vertical lines indicate the photon energy range covered by the EPT, whereas the blue dashed lines show the η' production from threshold to maximum MAMI C electron energy.

In general, the photo-production of the η' meson off the proton is described by the reaction

$$\gamma p \to \eta' p \to X p \,, \tag{4.2}$$

where X denotes an arbitrary decay of the η', for example $X = 2\gamma$. The initial state four-momentum of the reaction is known by detecting the bremsstrahlung-emitting electron in time coincidence with the detected final state particles, assuming the target proton is at rest.[1] The statistical treatment of those "prompt" electrons opposed to randomly detected electrons is the well-established "prompt-random" subtraction technique of photon-tagging [97]. To this end, each detected electron with timing t in the EPT is assigned a weight,

$$w = \begin{cases} 1 & \text{if} \quad t \in [-3\,\text{ns}, 3\,\text{ns}] \\ -\frac{6\,\text{ns}}{2\cdot(50\,\text{ns}-5\,\text{ns})} & \text{if} \quad |t| \in [5\,\text{ns}, 50\,\text{ns}] \end{cases} , \tag{4.3}$$

or ignored if it is outside of any timing window, as depicted in figure 4.2. The width of the prompt, where $w = 1$, and the two random timing windows, where $w < 0$, are chosen such in equation (4.3) to include the full prompt peak and to make the statistical error due to the random event subtraction negligible while maintaining an acceptable analysis performance of a few hundred events per second. In each event, the analysis is carried out for each tagger hit and subsequent quantities are then weighted with the weight w yielding prompt-random subtracted results. As the statistical errors are smaller the narrower the prompt window is chosen, it is beneficial to improve the timing resolution of the detected EPT electrons, which are implicitly measured relative to the global trigger timing derived from the CB analog sum signal, see also figure 2.11 on page 29. To this end, the trigger timing information for each event is recovered by the energy-weighted sum over reconstructed cluster timings in CB as follows:

$$\bar{t}_{\text{CB}} = \frac{\sum_{\text{CB}} E_i^{\text{cl}} t_i^{\text{cl}}}{\sum_{\text{CB}} E_i^{\text{cl}}} \,, \tag{4.4}$$

where E_i^{cl} denotes the total energy of cluster i and t_i^{cl} the corresponding timing given by the highest energy crystal. Eventually, the electron timing t in equation (4.3) is improved by subtracting the trigger timing given by equation (4.4) as the implicitly involved TDC read-out reference timing cancels,

$$t - \bar{t}_{\text{CB}} = (t' - t_{\text{TDC ref.}}) - (\bar{t}'_{\text{CB}} - t_{\text{TDC ref.}}) \,. \tag{4.5}$$

[1] This assumption is well-justified, as at $T \approx 20\,\text{K}$ the mean kinetic energy of the proton is negligible, $k_{\text{B}}T \approx 1 \times 10^{-3}\,\text{eV} \lll 1\,\text{MeV}$.

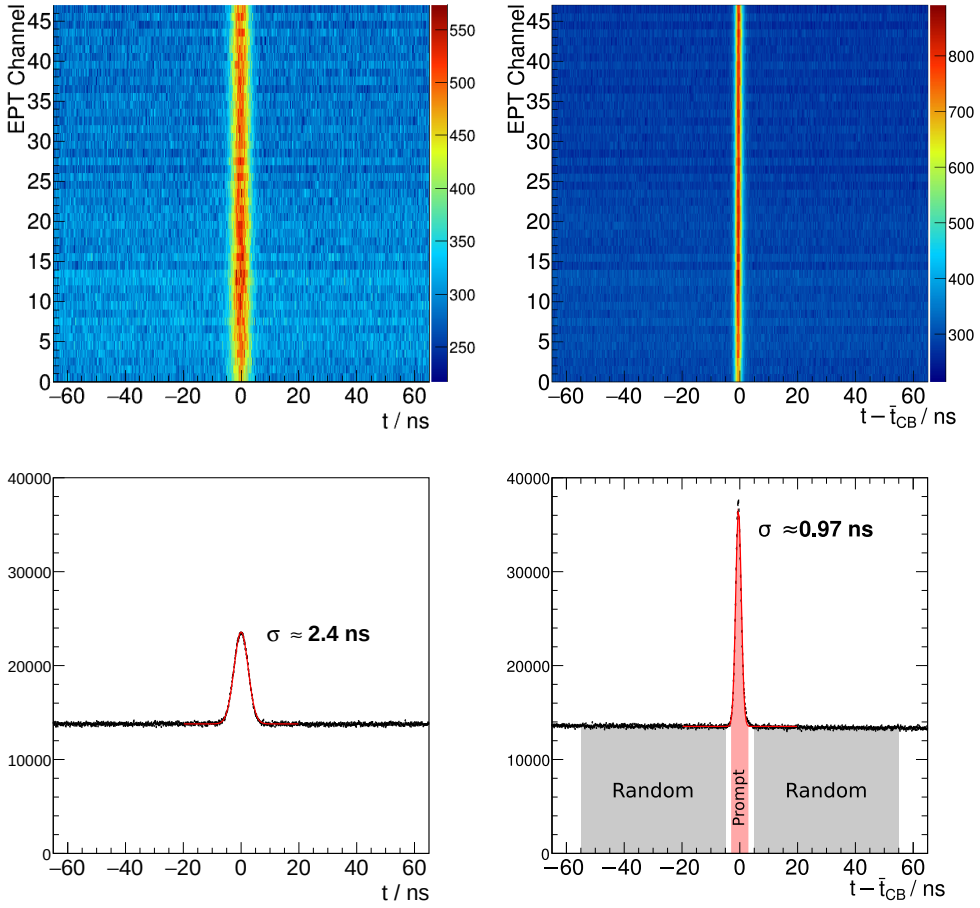

Figure 4.2.: The timing of the hits detected in the EPT shows a coincidence peak after an offset calibration as they are measured relative to the trigger timing, as shown in the left column. As shown in the right column, the timing resolution σ is improved significantly by subtracting the energy-weighted timing of CB clusters given by equation (4.4). The prompt and random intervals used in equation (4.3) are also shown in the bottom right panel.

The analysis of the $\eta' \to \omega\gamma$ decay is carried out relatively to the $\eta' \to \gamma\gamma$ decay as a reference channel, which reduces the influence of systematics related to the production of the η'. Alternatively, the photon flux and thus the luminosity can be determined via a so-called tagging efficiency measurement[2] to achieve an absolute number of produced η' mesons using the known production cross-section and hence eliminate the need for a reference channel [92]. However, as this requires a careful understanding of the systematics of an absolute measurement, the first approach with a reference channel is chosen for this thesis.

The branching fraction of the $\eta' \to \omega\gamma$ decay is given as

$$\begin{aligned} \mathrm{BR}(\eta' \to \omega\gamma) &= \mathrm{BR}(\eta' \to \gamma\gamma) \cdot \frac{\#(\eta' \to \omega\gamma)}{\#(\eta' \to \gamma\gamma)} \\ &= \mathrm{BR}(\eta' \to \gamma\gamma) \cdot \frac{N(\eta' \to \omega\gamma) \cdot \varepsilon(\eta' \to \gamma\gamma)}{N(\eta' \to \gamma\gamma) \cdot \varepsilon(\eta' \to \omega\gamma)} \,, \end{aligned} \tag{4.6}$$

where N denotes the number of the reconstructed events associated with the channel and ε the corresponding reconstruction efficiency of the whole analysis chain determined by Monte Carlo (MC) detector simulation. The branching fraction of the $\eta' \to \gamma\gamma$ decay is used as a reference input and is given as [17]

$$\mathrm{BR}(\eta' \to \gamma\gamma) = (2.20 \pm 0.08) \times 10^{-2} \,. \tag{4.7}$$

This decay channel of the η' is chosen since it has a comparatively large and well-known branching fraction and its final state consists of photons only, which nicely fits to the capabilities of the calorimeters CB and TAPS. The alternative channel $\eta' \to 2\pi^0\eta \to 6\gamma$ offers a three times larger total branching fraction, but is more difficult to analyze due to the higher multiplicity in the final state, such that the reconstruction efficiency does not compensate the larger branching fraction.

Furthermore, the polar angle θ of the scattered proton in equation (4.2) is limited kinematically to $\theta \lesssim 20°$, as shown in figure 4.3 owing to the relation

$$\cos\theta = \frac{1}{2E_\gamma p}\left(m_{\eta'}^2 + 2\Big(E_\gamma + m_\mathrm{p}\Big)\Big(\sqrt{m_\mathrm{p}^2 + p^2} - m_\mathrm{p}\Big)\right), \tag{4.8}$$

where $m_{\eta'} \approx 958\,\mathrm{MeV}$ is the rest mass of the η', $E_\gamma = 1420\,\mathrm{MeV} \ldots 1580\,\mathrm{MeV}$ is the incident photon energy and $m_\mathrm{p} \approx 938\,\mathrm{MeV}, p, \theta$ are the rest mass,

[2] The term "efficiency" is commonly used in A2 but misleading, as it is actually the probability that an electron hit in the EPT generated a photon impinging the target by passing the photon beam collimation, which does not depend on the EPT electron detection efficiency.

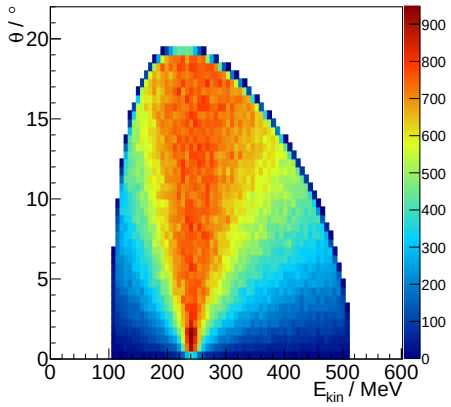

Figure 4.3.: The kinetic energy against the polar angle θ of the scattered proton is shown for incident photon energies between 1447 MeV (production threshold) and 1580 MeV (EPT highest photon energy), generated from $\gamma p \to \eta' p$ according to phase space. The maximum polar angle θ_{max} of the scattered proton for η' meson production is roughly 20°. See also equation (4.8).

momentum and angle of the proton, respectively. This makes TAPS an ideal proton detection device for η' production regarding its particle identification techniques such as ToF or PSA, see section 2.5.

A high luminosity, defined as the product of photon flux times the target cross section area density, is required to compensate for the low photo-production cross-section of the η' mesons near threshold, see figure 4.1. Owing to the substantial improvements to the DAQ as described in section 2.6, an unprecedented high electron beam current of 60 nA and thus photon flux on the liquid hydrogen target has been achieved at acceptable DAQ live-times, see table 4.1 for an overview and [92] for a detailed investigation of the luminosity. In comparison to a pilot EPT beam-time in 2012, the beam current is three times larger. The trigger condition requires a total energy deposition in CB of $\sum_{\text{CB}} E \gtrsim 550\,\text{MeV}$, which has been optimized for η' decay channels.

4.2. Software environment

An easily usable and well-tested software environment is a crucial component for any successful analysis. Historically, the A2 collaboration entirely relied on the so-called Acqu framework, taking care of the whole experiment software

Beam current	60 nA
Luminosity	5.9/(μb s)
Radiator thickness	10 μm
Collimator	4 mm
Target length	10 cm
Tagger rate	0.8 MHz per-channel
Trigger condition	$\sum_{\mathrm{CB}} E \gtrsim 550\,\mathrm{MeV}$
Trigger rate	2.5 kHz
DAQ live-time	≈ 60 %
Used detectors	CB, PID, TAPS, EPT

Table 4.1.: Nominal beam time conditions during the EPT production runs. They have been optimized during a test beam time in July 2014 to record as many η' events as possible under the given constraints of the system, which is eventually the maximum rate of 1 MHz per EPT detector element. The maximum beam current the MWPCs could stand is 20 nA, despite substantial Ethanol doping decreasing its detection efficiency to hardly acceptable levels below 80 %.

tasks from data acquisition to physics analysis. Its origins can be traced back to the early 1990s and was later based on the common analysis framework ROOT [98]. For many years, the analysis part of the Acqu framework has been inhomogeneously distributed among the users, leading to tedious discussions on technical issues and the re-implementation of identical functionality at different places within the collaboration. At the beginning of this thesis, an attempt [99] to synchronize those development efforts and to quickly share fixes and improvements was initiated using the version control system git [100]. In particular, each beam time needs slightly adapted setup files reflecting configuration changes in the DAQ and detector setup, some of them only known to a few experts of the system. Furthermore, deploying and debugging the Acqu framework has been improved by introducing a cmake-based [101] build system and thus enabling support for Qt Creator [102] as the preferred integrated development environment (IDE), which is an excellent tool for C++, even for non-GUI projects despite its name. Moreover, after basic analysis steps have been carried out for the η' beam time data, a modern clustering algorithm has been developed and subsequently tested on MC and data input. The key improvement is the topological aggregation of energy depositions with an arbitrarily large number of crystals and the subsequent search for local energy maxima, exploiting the natural segmentation of the calorimeter, see

section 4.3 for details. Although this algorithm performs better [103] than several old algorithms, which for example aggregated only the energy of the nearest neighbors, the corresponding patch to the Acqu framework was not accepted within the collaboration employing a single clustering algorithm due to concerns about backwards compatibility of energy calibration parameters and reproducibility of previous results.

The Acqu framework is supplemented by the CaLib framework [104, 105] taking care of the various calibration tasks, for example time offsets or energy gains for the calorimeters. However, improvements of this system always require consistent changes in its stand-alone part and the corresponding Acqu part, which led to the integration into the Acqu framework in 2013. Furthermore, the calibration coefficients are stored in a MySQL database, whose design did not allow calibration coefficients to change run-by-run or reverting to a previous iteration without tediously restoring backups of the whole database, possibly affecting all beam-times.

In 2013, the GoAT framework [106] was developed to mitigate shortcomings of the Acqu framework for typical physics analyses, such as the incomplete filtering capabilities to improve performance and the unstable and confusing application programming interface (API). To this end, files in ROOT's TTree format are dumped from Acqu which contain events after the clustering algorithm and calibration has been applied, as well as information about the experimental setup to unpack the input data. Subsequently, those "GoAT trees" are processed with particle identification and filtering techniques for rapid development of physics analyses.

Eventually, after a few years of working with this complex tool-chain consisting of Acqu, CaLib and GoAT, the Ant analysis framework [107] was developed without any dependency on those existing frameworks within the scope of this thesis. Many already available code parts, such as the clustering algorithm, are re-used or suitably adapted. Moreover, techniques from modern C++11 software development are enforced, such as test-driven development and continuous integration [108], and documentation efforts are undertaken. The implementation of all components required for a complete analysis was rapidly achieved including the reconstruction of events from various data sources, as shown in figure 4.4. In particular, the proper integration of the ROOT framework within modern wrappers is crucial to prevent memory leaks or poor input/output performance. For example, the Acqu framework suffers from the

[3]The multi-threading in Acqu is only required if run in data-acquisition mode merging input from several sources, but still 4 threads are spawned if "off-line" analysis is carried out in Acqu. Ant, as a pure analysis framework, is deliberately designed single-threaded to avoid an overly complex design.

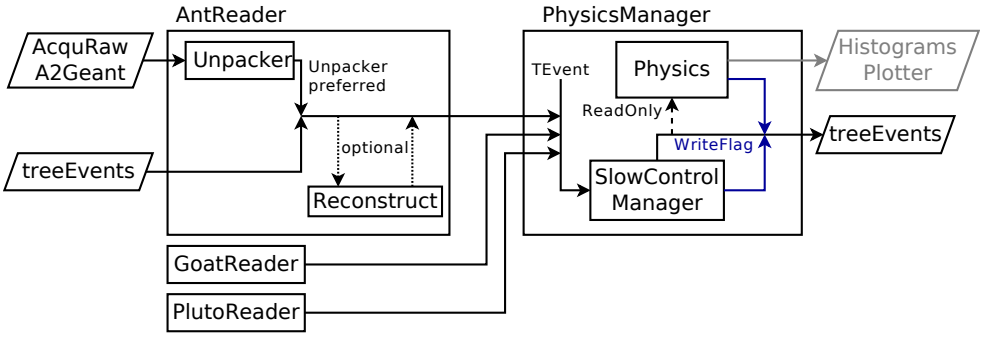

Figure 4.4.: The Ant analysis framework processing is shown as a flow chart. Data is processed from different sources, for example raw data in "Acqu Mk1/Mk2 format" or GEANT detector simulation output in ROOT's TTree format including true information from the event generator Pluto. The PhysicsManager takes care of processing the events including buffering for proper slow control information. Finally, the data flow can be re-used with "saved" events flagged by physics classes.

design decision that every class derives from ROOT's `TObject` class and does not properly take care of data encapsulation inside the multi-threaded environment.[3] Moreover, the calibration routines from CaLib are re-implemented in Ant and subsequently improved including a convenient GUI for the fitting of calibration spectra, see section 4.4. For example, the database is realized as git-tracked folder structure, where each iteration is represented as a set of files, which renders database changes into standard file operations. Additionally, each calibration iteration is properly documented by a corresponding git commit message.[4]

The reconstruction within the Ant framework has been successfully compared event-by-event against standard Acqu/GoAT system. The challenging implementation of the kinematic fitter has been carried out with the help of a modern C++11 wrapper [109, 110] around the well-tested APLCON Fortran code [111], which provides general routines for χ^2 minimization under constraints treating measured and unmeasured variables identically. Additionally, the GEANT-based detector simulation code a2geant [112] and the MC event generator Pluto [113] are supported with corresponding readers, see figure 4.4. In particular, a mixture of the main photo-production channels and their decays

[4]Note that each iteration of a time-dependent energy calibration, as described in section 4.4, has a size of around 50 MB compressed on disk, resulting in databases of a few GB in size.

has been developed as an extensible database containing realistic cross-sections and branching fractions, the so-called Pluto MC cocktail [92]. This allows for a quick and thorough check of background channels for any user-defined analysis, although the cocktail does not model differential cross-sections but assumes flat angular distributions instead. The Ant framework supports these detailed MC studies by providing various tools to manage a possibly large number of relevant backgrounds.

4.3. Event reconstruction

Within the Ant framework, the reconstruction of input into a representation suitable for physics analysis takes place in several stages, which are described in the context of the A2 experimental setup, although Ant uses concepts which are applicable beyond the scope of A2.

Unpacking This stage extracts the raw information from the input file into detector hits using the provided mapping from channel numbers as realized in the experiment to logical channels realizing an abstract representation of the detectors[5]. Furthermore, this stage figures out as much information as possible about the input file automatically, runs sanity checks and tries to handle incorrectly recorded raw data files.

Hit mapping As most detectors provide energy and timing information for each element, this stage groups this information according to logical channels. Furthermore, it decodes the raw information into physically meaningful values, such as the timing information of the CATCH TDC multiple hit buffer. The resulting object is called a cluster hit. At this stage, the tagger detector is treated separately and adds its information as so-called tagger hits to the event.

Clustering The cluster hits are aggregated into so-called clusters in this stage. This process is trivial for the PID detector, as every cluster hit is transformed into one cluster, but more involved for the electromagnetic showers detected in the calorimeters CB and TAPS, as described in more detail below.

Candidate matching A so-called candidate consists of one or more clusters, and the candidate matching stage builds those from the provided clusters.

[5] This mapping renders re-cabling detector elements, which would change its channel number used in the input file, transparent to subsequent analysis components using solely logical channel numbers.

For example, the PID clusters are matched to clusters in CB and the candidate is assigned a veto energy[6] determined from the PID. Furthermore, some clusters may be ignored and not turned into a candidate, for example unmatched PID clusters or calorimeter clusters below a user-defined threshold.

While the event is being reconstructed, it can be modified and observed at any intermediate stage using so-called hooks. For example, the conversion for the CATCH TDC needs to find a trigger reference timing for hit synchronization and calibration modules convert detector raw data into timings and energies. Furthermore, during the decoding of the event stream, the reconstruction may update the parameters of the calibration modules depending on the uniquely assigned identification number of each event. This flexible approach makes so-called time-dependent calibrations feasible, as detailed in section 4.4.

Clustering algorithm

A crucial part of the event reconstruction is the clustering for the calorimeters CB and TAPS. The goal is to recover the energy and position information of the incident initial particle which generated the recorded electro-magnetic shower typically spanning more than one crystal element of the clustering detector. To this end, the energy information of neighboring elements is aggregated and an average position is calculated. However, as higher energetic particles create laterally larger clusters, separate showers are more likely to merge into one. Furthermore, some scattering reactions inside the scintillation material of the detector create energy depositions sufficiently far away from the remaining shower leading to so-called split-off clusters. Both phenomena are handled by an appropriately designed algorithm, whose capability to do so is however limited by the ignorance of the underlying physics of the complete event.

As already mentioned, joint analysis efforts in A2 suffer from the use of many different clustering algorithms, each resulting in its own energy calibration, as discussed below. Thus, the clustering algorithm implemented in Ant provides a general solution with a minimum number of input parameters. It is inspired by concepts presented in [114, 115], but in particular the details of cluster splitting are novel. In principle, the algorithm consists of three phases:

Phase 1 Gather clusters by neighboring relation

Phase 2 Search local maxima inside cluster, called bumps

Phase 3 Split clusters according to stabilized bumps

[6] The term "veto energy" originates from the usage of the deposited ΔE PID energy to discriminate, or "veto", charged particles, such as protons or electrons, from photons.

The first phase is rather greedy because the neighbor relation is typically defined as sharing the same corner and not only the same edge. This already mitigates the generation of split-off clusters but inevitably deteriorates the capability to separate two close particle depositions, possibly only apart by one crystal and sharing the same corner. The greediness is compensated by the second and third phase.

The second phase consists of the following steps, applied to each aggregated cluster from the first phase consisting of N single crystal energy depositions denoted E_i, $i = 1, \ldots, N$.

1. Find seeds for local energy maxima by a robust gradient voting algorithm. At each crystal, a vote is initially placed. If one of its neighboring crystals has a higher energy, the vote is moved to that crystal, otherwise the vote counts for the current crystal. If only one crystal obtained all votes, the cluster is left unchanged and returned as a whole.

2. At each seed crystal from the previous step, a so-called bump with position $\vec{b}_k$ is defined, where k counts the bumps. Each bump has the energy

$$E^k_{\text{bump}} = \sum_{i=1}^{N} w^k_i E_i \tag{4.9}$$

with the weights calculated as

$$w^k_i = \frac{1}{N_k} E_i \exp\Big(-2.5 \frac{|\vec{r}_i - \vec{b}_k|}{r_{\text{M}}}\Big)\,, \tag{4.10}$$

where r_{M} is the material-dependent Molière radius, $\vec{r}_i$ the position of crystal i and N_k is such that $\sum_i w^k_i = 1$ for each bump k individually. The exponential decay factor of 2.5, essentially rescaling the parameter r_{M} in equation (4.10), is suitably chosen while varying the factor shows no dramatic influence on the performance of the clustering algorithm [103].

3. Using the weights from the previous step, the bump position is recalculated according to [116] as follows

$$\vec{b}_k = \frac{\sum_i \omega^k_i \vec{r}_i}{\sum_i \omega^k_i} \tag{4.11}$$

with the weights[7]

$$\omega_i^k = \max\Big(0, 4.0 + \ln\big(w_i^k E_i / E_{\text{bump}}^k\big)\Big) \,. \tag{4.12}$$

The max(...) statement in equation (4.12) assigns crystals with partial energies $w_i^k E_i$ below $e^{-4.0} \approx 1.8\,\%$ of E_{bump}^k a weight of 0, which improves the position average in equation (4.11) by ignoring crystals with low energy. As w_i^k are normalized to each bump individually according to equation (4.10), the sum of all bump energies is *not* equal to the total cluster energy. The "energy conservation" is eventually taken care of in the bump cluster building phase, as discussed below.

Step 3 is carried out iteratively until the bump positions $\vec{b}_k$ are do not change anymore or, in rare cases, a maximum number of iterations is reached. In this case of no convergence, the leftover unstable bumps are discarded. If no stable bumps are found at all, again a rare case, then the cluster is returned as is, which ensures that no energy information is discarded by the algorithm. If two or more bumps with the same crystal of largest weight $w_k^{i=i_{\max}}$ are found in one iteration, which is an overlap situation, then the corresponding bumps are merged by averaging over their weights element-wise.

The third and last phase uses the stabilized bumps to split the given cluster. To this end, each bump k iteratively builds a partial cluster with E_{split}^k starting at the crystal[8] $i_{\max}$ of its largest weight $w_k^{i=i_{\max}}$. One iteration step subsequently adds the energy of the neighboring crystals to E_{split}^k. Once a crystal at position $\vec{r}_j$ would be claimed by two or more bumps in the same iteration step, the energy of that crystal is shared among the clusters. To this end, a preliminary position $\tilde{\vec{b}}_k$ analogously to equation (4.11) of each bump claiming the crystal is calculated first with weights

$$\tilde{\omega}_i^k = \max\Big(0, 4.0 + \ln\big(E_i^k / E_{\text{split}}^k\big)\Big) \,, \tag{4.13}$$

where E_i are the crystal energies previously assigned to the claiming bump k and E_{split}^k is the sum of those energies.[9] Next, the percentage energy of a participating bump k at crystal j is calculated as

$$p_j^k = \frac{1}{N_j} E_{\text{split}}^k \exp\Big(-|\vec{r}_j - \tilde{\vec{b}}_k| / r_{\text{M}}\Big) \,, \tag{4.14}$$

[7] Note the different notation, ω_i^k versus w_i^k.

[8] By virtue of equations (4.10) and (4.12), this is the crystal element closest to the stabilized bump position $\vec{b}_k$.

[9] Note that the number of those energies E_i and thus E_{split}^k cannot be zero, as at least the starting crystal is uniquely assigned to a non-overlapping bump at the beginning of the phase.

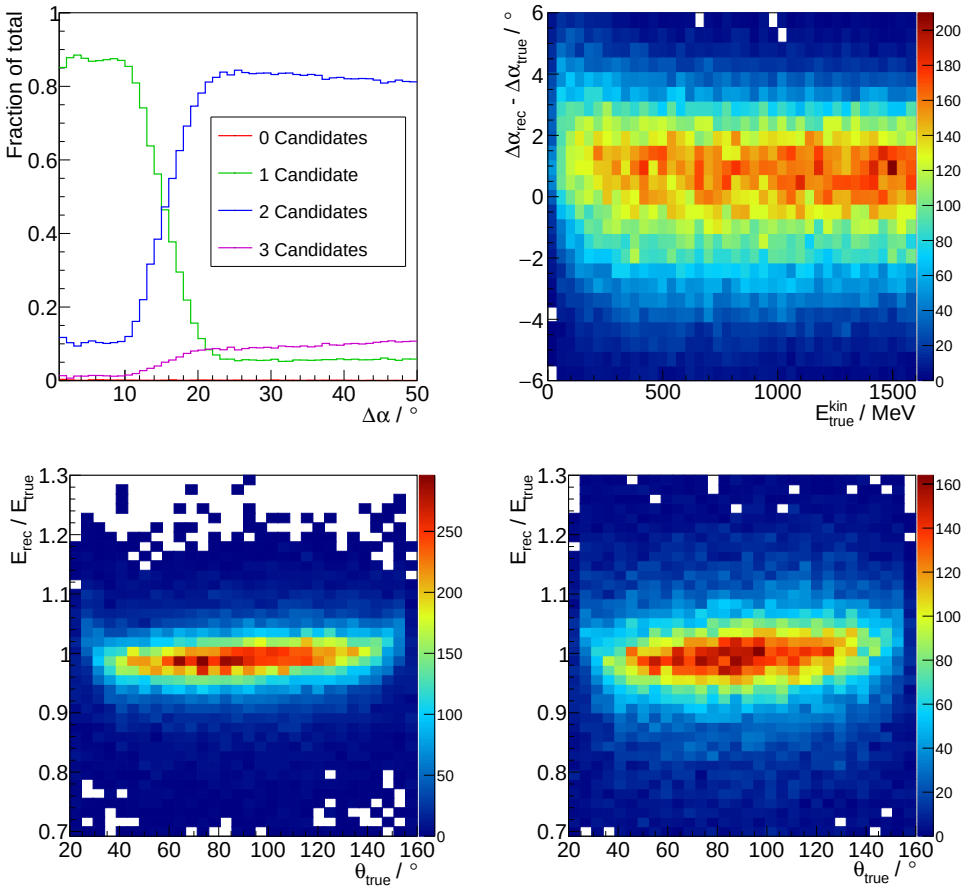

Figure 4.5.: Reconstructed properties of two spherically uniformly generated photons with an opening angle $\Delta\alpha$ from 0° to 50° and uniformly distributed kinetic energies from 0 MeV to 1600 MeV are shown. Ideally, the number of reconstructed candidates in CB should be 2, which is predominantly the case for $\Delta\alpha \gtrsim 20°$ as shown on the top left. For the critical region $15° < \Delta\alpha < 20°$, the difference of the opening angle of the reconstructed candidates, $\Delta\alpha_{\mathrm{rec}}$, to true opening angle $\Delta\alpha_{\mathrm{true}} = \Delta\alpha$ is shown in the top right panel. For the same $\Delta\alpha$ region, the cluster energy of the higher energetic (bottom left) and lower energetic (bottom right) reconstructed candidate relative to the true energy information is shown, which should ideally be 1, as a function of the true polar angle θ. See also section 4.4 discussing single photon energy scales in more detail.

where N_j such that $\sum_k p_j^k = 1$. This normalization ensures "energy conservation" in a sense that the total available energy defined as the sum of all input crystal energies is equal to the sum of cluster energies. In summary, the aggregated cluster from the first phase is split according to the stabilized bumps representing local energy maxima. Note that the number of crystals assigned to each cluster is not conserved, as crystals may be shared among partial clusters.

A good indicator for the performance of the clustering algorithm is the opening angle of two photons which are still reconstructed as two clusters. This is conveniently studied with the GEANT4-based MC detector simulation using suitably generated photons with well-known energies and relative angles, as shown in figure 4.5 and also carried out in [103]. The smallest angle at which two cluster events dominate is found to be around 15°, which is about two times the average angular distance of two crystals in CB as naively expected. In summary, the analysis of high beam energy data such as the EPT runs in 2014 benefits significantly from this improved clustering algorithm, as the two-photon invariant mass spectra show unprecedented narrow peak widths and proper alignment after careful calibration, see section 4.4. Furthermore, the algorithm needs only a small and well-motivated set of parameters without beam-time specific tuning, which makes it a first step towards a collaboration-wide common calibration routine.

4.4. Event calibration and quality checks

In general, calibration procedures adjust parameters to account for inhomogeneities of the experimental setup and thus serve as an input for the successful reconstruction of an event, as explained in section 4.3. There are various sources for those inhomogeneities, such as different cable lengths resulting in shifted positions of time coincidence peaks or varying conversion gains of PMTs, possibly caused by unstable HV supplies or temperature drifts, resulting in different scales for an energy determination. In order to obtain suitably calibrated events, various methods with complex interdependencies are employed, as shown in figure 4.6. The different calibration modules as implemented in Ant are explained in the following with a focus on the energy calibration of the CB calorimeter.

The timings of the detector channels are typically measured relative to a experiment-wide distributed timing reference derived from the trigger signal. The time offset calibrations, for example "PID Time" or "TAPS Time" in figure 4.6, align the resulting coincident timing peak for each detector channel

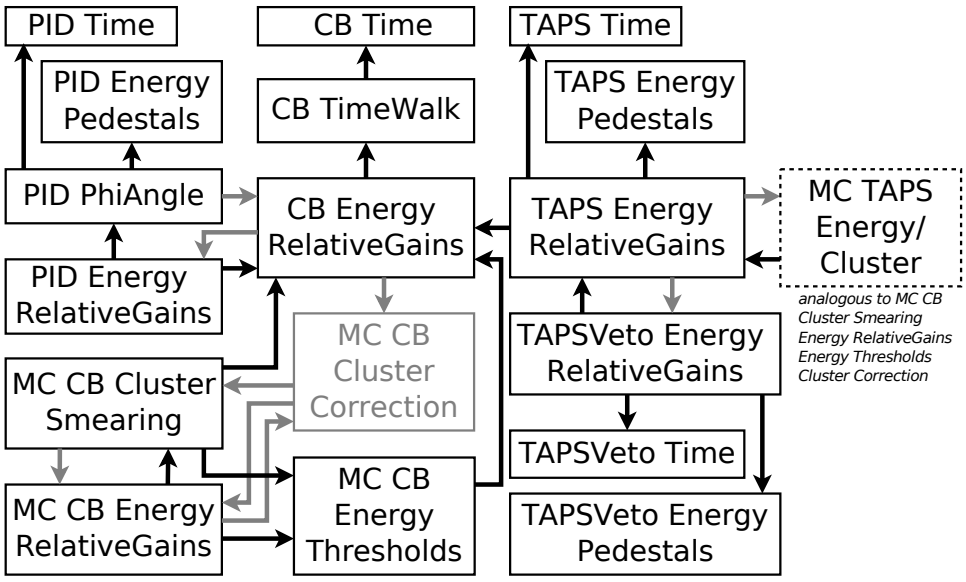

Figure 4.6.: The various calibration modules and their dependencies are shown. Arrows denote "depends on" in this chart. For example, to carry out the "PID PhiAngle" calibration, the "PID Energy Pedestals" and the "PID Time" calibrations must be carried out first. Gray items or arrows denote minor importance or dependence, respectively. See text for further details, in particular regarding the dependency loop for MC-driven energy calibrations.

at position zero, which simplifies the application of timing windows to suppress random hits. The conversion of a raw timing measurement ξ into a physically meaningful time t, by convention measured in ns, is calculated as

$$t = \kappa_i \cdot \xi - t_i^{\text{offset}} \,, \tag{4.15}$$

where i denotes the per-channel dependence of the parameters. For the widely used[10] CATCH TDCs, the conversion factor $\kappa_i \equiv \kappa$ is fixed to 0.1171 ns per raw unit. The calibration module determines the coincident timing peak position by a Gaussian fit and adjusts a previously set t_i^{offset} by a corresponding relative amount. This calibration needs to be carried out only once and applies globally to the whole beam-time and serves as an important data quality check as described below.

[10] The CATCH TDC conversion implemented in Ant properly handles the overflow at the magic number 62 054, see figure 2.13 on page 31.

For TAPS timings, which are recorded with NTEC VMEbus modules as shown in figure 2.10 on page 28, the TDC measurements are stopped instead of being started by the trigger reference timing. This is accounted for by using negative conversion factors $\kappa_i \equiv \kappa$ of $-0.1\,\mathrm{ns}$ per raw unit in equation (4.15).[11] This proper treatment is crucial if TAPS timings are subtracted from CB timings, which is typically the case to improve ToF measurements.[12]

The "PID PhiAngle" module determines the alignment of the PID elements with respect to the CB elements by ignoring the candidate matching and instead investigating events with exactly one CB and exactly one PID cluster. They exhibit a correlation peak in the azimuthal angle ϕ, as the PID is constructed as a detector with cylindrical symmetry. One global rotation angle around the z-axis is determined as the y-intercept parameter from a linear fit to all ϕ_i correlations per PID element i. In contrast, the CaLib/Acqu framework uses element-wise ϕ_i angles for candidate matching, which may be inconsistent with the geometrical constraints of the PID detector.[13]

The CB timings are corrected for their dependence on the input signal amplitude originating from the LEdD, similarly to [104, 117], for example. For the high-energy and high-rate EPT beam-times, it is crucial to properly account for multiple TDC hits per event and to use a logarithm of uncalibrated energies E_raw in raw ADC units, that is before conversion to the MeV scale, as shown in figure 4.7. The logarithm avoids an incorrect extrapolation of the fit function to higher energies. Choosing raw energies as a measure of the input amplitude renders the time-walk correction independent of the energy gain calibration discussed later. The amplitude dependence is sufficiently well described by[14]

$$\Delta t(x) = p_0 + p_1(x - p_2) + p_3 \exp\Big(-p_4(x - p_2) - p_5 \ln(x - p_2)\Big)\,, \qquad (4.16)$$

where $x = \log_{10}(E_\mathrm{raw})$ and p_i, $i = 1, \ldots, 5$, are fit parameters. The two-dimensional histogram of multiple TDC hits versus $\log_{10}(E_\mathrm{raw})$, as depicted in figure 4.7, is projected for each bin at position x_i and subsequently fitted with

[11] By virtue of a dedicated measurement, the TAPS TDC conversion factor is determined for each channel individually. However, the deviation from $-0.1\,\mathrm{ns}$ per raw unit is negligible and currently not included in the calibration database.

[12] It is also common practice in A2 to improve TAPS timings by subtracting tagger timings, which, however, leads to difficulties with respect to prompt-random subtraction.

[13] For an unknown reason, the PID are flipped around the z-axis in the A2 detector simulation geometry. The CaLib/Acqu framework accounts for this by using decreasing instead of increasing ϕ_i parameters. Ant fixes this already during the unpacking stage.

[14] To improve the numerical stability of the fit optimization, the factor $1/(x - p_2)$ is written as $\exp(-\ln(x - p_2))$.

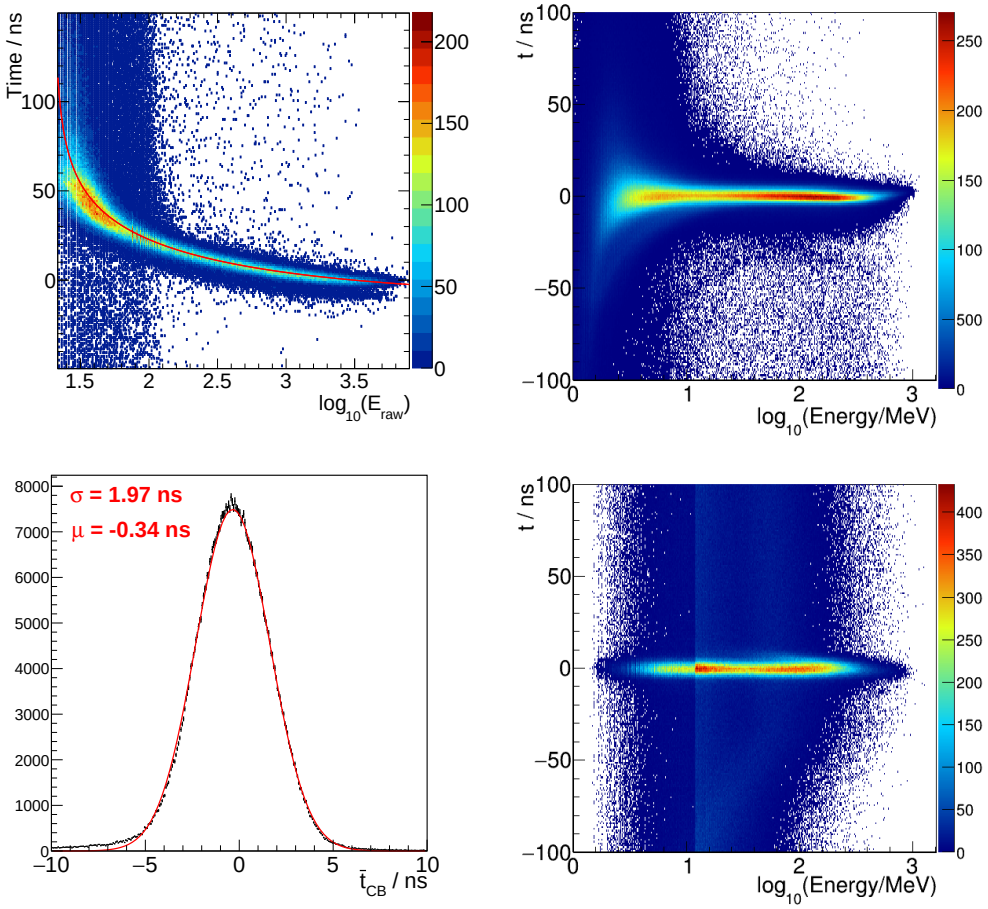

Figure 4.7.: The CB time-walk calibration removes the dependence of the timing on the signal amplitude (top left, with E_{raw} in ADC raw units) and leads to an Gaussian-shaped timing reference (bottom left) as defined in equation (4.4). After correction, the CB cluster hit timings (top right) show similar behavior as TAPS timings (bottom right) using a hardware CFD.

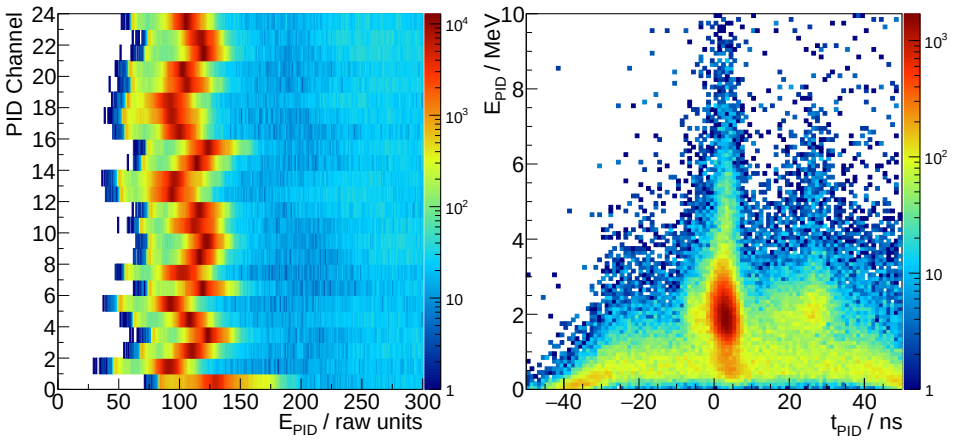

Figure 4.8.: The PID pedestal peaks for each channel are shown on the left and determined by fitting channel-wise projections, compare also figure 2.5 on page 21. On the right, events containing a proton are selected using a kinematic fit and the energy (roughly calibrated) and timing response is shown. The proton detection efficiency is significantly reduced if the timing window is narrower than −25 ns to 40 ns.

a Gaussian to obtain the peak position as the mean value y_i. The parameters p_i in equation (4.16) are then fitted to the points (x_i, y_i) after the removal of outliers. After the application of equation (4.16), CB timings are discarded outside a window of −25 ns to 25 ns. The proper implementation of this correction requires no additional CB leading-edge adjustment in contrast to [104] and derived timings such as the CB reference timing $\bar{t}_{\mathrm{CB}}$ in equation (4.4) stay aligned close to zero, again shown in figure 4.7.

In order to infer an energy information from an analog detector signal, the DAQ hardware carries out an integration over time of the input waveform. The result is provided as a digital raw value ξ, similar to a timing measurement. The single element energy E, by convention measured in MeV, is then determined as

$$E = g_i(\xi - \xi_i^{\mathrm{ped}})\,, \tag{4.17}$$

where g_i is usually called (energy) gain[15] for channel i and ξ_i^{ped} is the energy offset or pedestal.

[15] In Ant, the gain $g = \eta\tilde{g}$ is implemented as a product of a unit-less relative factor η and a usually constant conversion factor $\tilde{g}$. Hence the notation “RelativeGains”.

Pedestals are defined as the result of the measurement when no signal is present at the integrating ADC and thus the integration is carried out over the constant voltage baseline with a fixed integration gate length.[16] This should always result in the same raw value and thus a very pronounced peak in the ADC spectrum, see figure 4.8 for an example. Again, the position of this peak is determined by a fit and stored as ξ_i^{ped} with all other fit parameters for usage during reconstruction in the database.

The PID energy, denoted as "PID Energy RelativeGains" in figure 4.6, is calibrated such that neutral states can be clearly distinguished from charged particles given the rather broad pedestal peak of the PID analog signal integration. The PID timing window is chosen rather wide, as shown in figure 4.8, as some timings of identified proton candidates are seen about 25 ns later. Details of the PID energy calibration using the typical curved shape of the proton PID energy deposition[17] ΔE when plotted against the matched CB energy E are given in [93], as it is not crucial for the analysis presented later.

The energy gain calibration of the calorimeters CB and TAPS, denoted as "CB/TAPS Energy RelativeGains" in figure 4.6, uses the ubiquitous decay of the neutral pion into two photons with opening angle α and energies E_{γ_1} and E_{γ_2}, whose corresponding invariant mass is given by

$$m_{\gamma\gamma} = \sqrt{2E_{\gamma_1}E_{\gamma_2}(1-\cos\alpha)}\,. \tag{4.18}$$

As CB covers most of the solid angle, the whole procedure including the cluster energy correction as described in the following is carried out first for CB by using photons reconstructed in CB only. Subsequently, the procedure is applied to TAPS by using one candidate from CB and one from TAPS as the photon pair in equation (4.18), which improves the signal-to-background ratio in the invariant mass spectra for TAPS elements considerably. In general, the gains g_i in equation (4.17) of the two central elements in the corresponding clusters are tuned relatively such that the invariant mass peak m_{peak}, as shown in figure 4.9, matches the nominal value for the pion mass $m_{\pi^0} = 134.98\,\text{MeV}$,

$$g_i \to g_i + g_i k\Big(\frac{m_{\pi^0}}{m_{\text{peak}}} - 1\Big)\,, \tag{4.19}$$

where the factor k is chosen as $k = 1$ to increase convergence speed or $k = 0.5 < 1$ to suppress oscillations originating from the azimuthal correlation

[16] During the EPT beam-times the conventional photon-beam has been used instead of a random pulser to generate triggers for read-out. However, most of the time no signal is present and the pedestals are assumed to be undisturbed by additional noise or cross-talk by this non-optimal procedure.

[17] The PID energy measurement is multiplied by $\sin\theta$ to compensate for the flight length depending on the polar angle θ measured with CB.

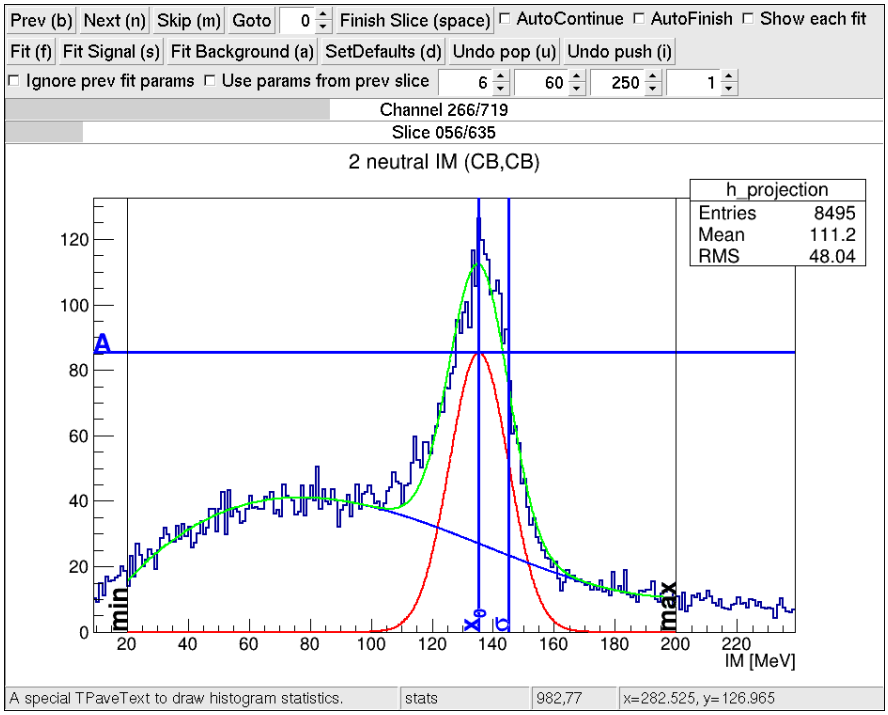

Figure 4.9.: The Ant-calib fit GUI for one channel in time-dependent calibration of CB relative gains. The π^0 peak position m_{peak} is determined using a Gaussian and separately controllable polynomial fit function of order 2. The fit is interactively controlled, for example moving the vertical blue line labeled with "x_0" directly influences the mean position of the Gaussian signal function (shown in red) and thus m_{peak}. Additionally, automatic fitting is supported in order to manage the about 10^4 separate fits for each time-dependent iteration.

of elements, in particular prominent in TAPS. Since $m_{\gamma\gamma}$ in equation (4.18) is calculated from two clusters with central crystals i and $j \neq i$ corresponding to two different gains g_i and g_j, the procedure must be carried out iteratively and converges after typically 10 iterations. It is first applied across some sufficiently large subset of a beam-time,[18] which averages over time-dependent gain drifts and is thus called time-*in*dependent in the following. The dependence depicted in figure 4.6 on the veto information, such as "PID Energy RelativeGains", stems from the discrimination of charged particles requiring no ΔE deposition in matched veto elements. However, as the π^0 invariant mass peak is clearly dominated by neutral photons, this dependence is assumed to be weak. In TAPS, the inner and outer elements do not show a discernible π^0 peak due to shower leakage and are thus flagged as "NoCalibFill", meaning that their gains are determined by an average of their neighbors. Furthermore, the inner $PbWO_4$ crystals are only calibrated with default gains for the whole beam-time, thus flagged as "NoCalibUseDefault", due to hardly identifiable π^0 peaks. The status of detector elements is shown in figure 4.14.

After the time-independent calibration has converged sufficiently, the energy gains are tuned separately for each run, or "slice" in Ant terminology[19], and thus the time-dependence of the π^0 peak position is compensated. Since one slice does not provide enough statistics to ensure a stable determination of the peak position over background, a Savitzky-Golay [118, 119] bin-by-bin averaging[20] along the slices is employed before the fit. The window size is chosen as 10 and 30 slices for CB and TAPS[21], respectively, and the polynomial order for the Savitzky-Golay filter is set to 4. After each time-dependent iteration, an additional averaging of the gains is performed with a width of 20 slices for CB and 30 slices for TAPS, both with polynomial order 6. It accounts for slow drifts of the gains on the time-scale of hours, while minimizing the influence of additional noise due to the fitting procedure. This compromise between smoothing and drift response is tested in detail using a MC toy simulation of the calibration tool-chain in figure 4.10 by mimicking a typical input of invariant mass spectra, see figure 4.9 for an example, with a priori known peak positions.

[18] A random but constant subset of the beam-time is chosen to carry out those iterations.

[19] Ant supports arbitrary slicing of beam-time data according to unique event numbers, which define validity ranges for arbitrary calibration data, but choosing a run-by-run segmentation is convenient.

[20] Different run lengths are respected by scaling with the number of events in each run.

[21] For the $PbWO_4$ crystals in TAPS, the default calibration gain determined from the full beam-time is used, as the π^0 peak position cannot be determined reliably due to low statistics and high background.

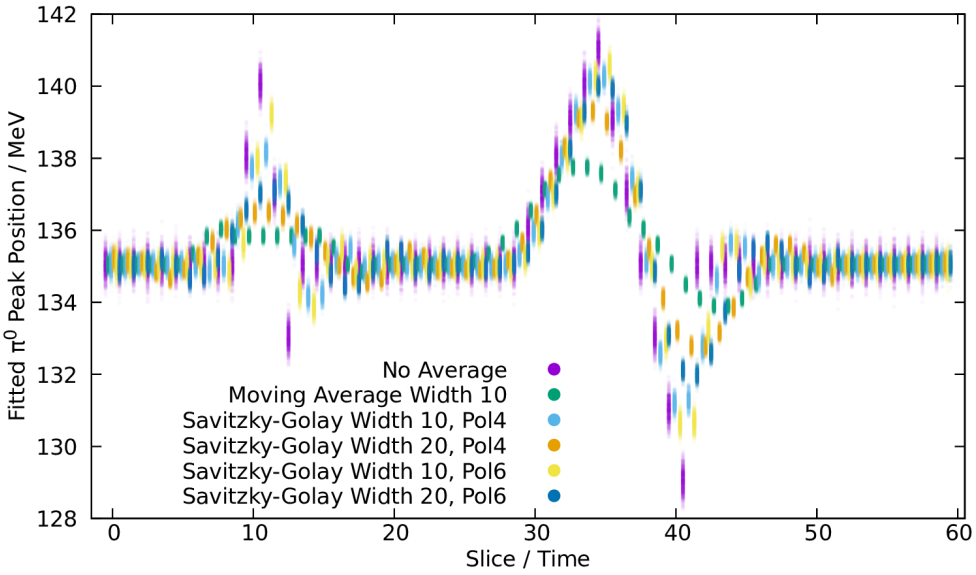

Figure 4.10.: MC toy model study for time-dependent energy calibration with different smoothing options. For all CB channels, invariant mass spectra with π^0 peaks at μ_i are identically generated for each slice i (counting from 0), mimicking a typical background shape and statistics, see for example figure 4.9. At slice $i = 10$, the peak position μ_i is quickly changed and at slice $i = 30$ a slower but larger change in μ_i is induced, which corresponds to changes on the time scale of hours. Fitted π^0 peak positions are subsequently determined with the standard Ant calibration tool-chain with different bin-by-bin averaging settings. For the case "No Average", the spread of the π^0 peaks for each slice is largest, but the systematic deviation of the mean from the true π^0 position vanishes as expected. Using a moving average window, the spread is reduced significantly, but the recovery of time-varying position is completely lost. A good compromise is found for a Savitzky-Golay filter with polynomial order 4 and width 10. See text for further details.

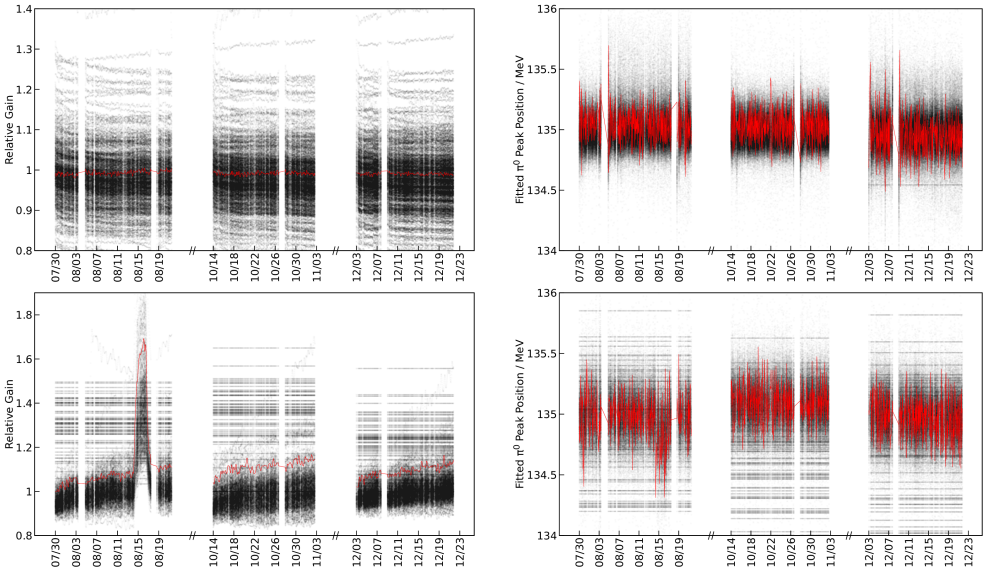

Figure 4.11.: The relative gains of all channels are shown over time on the top (bottom) left for CB (TAPS). On the right, the corresponding fitted π^0 peak positions are shown. For TAPS, the visible horizontal lines correspond to elements flagged as "NoCalibUseDefault", which are mostly $PbWO_4$ crystals, see figure 4.14. Around August 15, 2014, denoted as 08/15, the TAPS cooling fans stopped working due to a blown fuse resulting in a decreased scintillation light output. This is accounted for by a time-dependent increase of gains by roughly 40 % to keep the π^0 peak positions stable within less than 1 %. A typical channel is shown as an overlay in red.

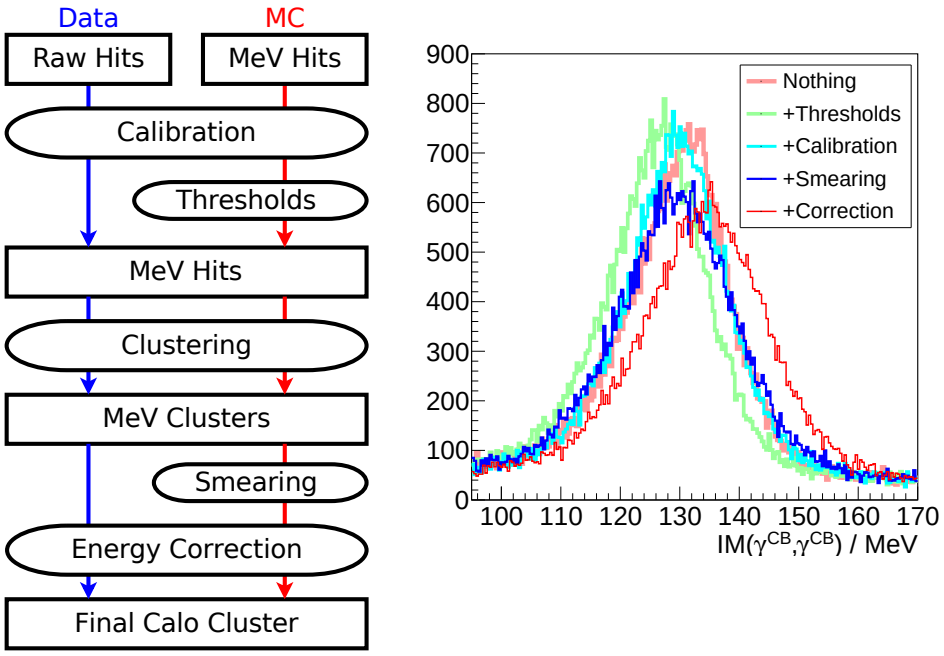

Figure 4.12.: For calorimeters CB and TAPS, the final cluster energy is determined similarly for data and MC input, as shown on the left. Besides the application of software thresholds on MC, an additional smearing is applied to clusters to correct the imperfect modeling of detector resolutions. The final energy correction of cluster energies accounts for the loss of energy due to single crystal thresholds, see text for further explanation. For each step, the effect on the invariant mass of two photons reconstructed in CB for generated $2\pi^0$ events is shown on the right.

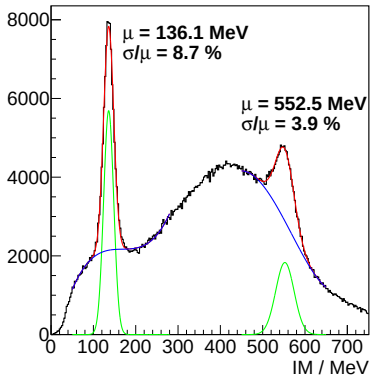

Figure 4.13.: Data events with two candidates in CB are selected from 4.6×10^6 total in one run file and assumed to be photons, whose invariant mass according to equation (4.18) is plotted (black line). The $\pi^0 \to 2\gamma$ and $\eta \to 2\gamma$ decays are visible with excellent resolution and within 1 % of the expected position, $m_{\pi^0} \approx 135.0\,\mathrm{MeV}$ and $m_\eta \approx 547.9\,\mathrm{MeV}$ [17]. Each signal peak is fitted with a Gaussian function (green line) with mean μ and width σ and fourth-order polynomial background (blue line).

Once the gains do not show relative fluctuations of more than $\pm 0.5\,\%$, the calibrated dataset is used to match the energy resolution of MC detector simulation to data. To this end, the cluster energies are additionally smeared on MC using a Gaussian distribution with $(E_k, \cos\theta)$-dependent widths on the order of $\sigma \approx 8\,\mathrm{MeV}$, as shown in figure 4.12. This procedure is carried out iteratively on the MC cocktail mimicking beam-time data [92] for CB and then, after CB has been finished completely, for TAPS. The π^0 peak widths are used to tune the $\sigma(E_\mathrm{kin}, \cos\theta)$ parameters of the Gaussian smearing dependent on the kinetic energy E_kin and the polar angle θ. Next, after the detector simulation matches the experimental resolutions well enough, the total cluster energies are corrected on data and MC for losses due to finite single crystal thresholds, which are in the order of 1 MeV. This correction is determined with simulated single photons, where the initial energy E_true is known, and the cluster energy correction factor is given by the average $\langle E_\mathrm{true}/E_\mathrm{rec}\rangle(E_\mathrm{rec}, n)$ dependent on the reconstructed energy E_rec and the

[22] The corrections are determined for the October 2014 beam-time, and then identically applied to the July/August and December beam-times. Minor differences in the experimental setup, such as differently flagged elements in figure 4.14, are neglected.

Name	Period	Total runs	"Good" runs
July/August	2014-07-30 – 2014-08-22	832	635, 76 %
October	2014-10-14 – 2014-11-03	819	640, 78 %
December	2014-12-03 – 2014-12-22	790	665, 84 %

Table 4.2.: The three data periods are usually referred to as the July/August, October and December EPT beam times, respectively. After several quality checks, only the "good" runs are subsequently analyzed, see text.

cluster size n. This compensates for the skewed mass scale of low-energy single photons, as the calorimeter is calibrated using two photon invariant masses given by equation (4.18). Details of the additional MC smearing and the single photon energy correction are given in [91].[22] After those two corrections are determined, a final energy gain calibration for data and MC is carried out, see figure 4.12. This assumes that those data-driven corrections are not strongly influencing the other calibrations and, thus, their dependence relation is indicated as weak in figure 4.6.

The energy calibration gains for all beam-times is shown in figure 4.11, and the resulting invariant mass spectrum of two candidates in CB, assumed to be photons, is shown in figure 4.13. Thanks to the improved clustering algorithm, no non-linear gain calibration, as proposed in [104, 120, 121], is necessary to match the η to the nominal mass position within less than a percent. Still, there is a systematic offset towards slightly higher peak positions compared to the nominal masses, which could be related to either the different analysis procedure,[23] to the time-dependent smoothing or to the single photon energy correction as discussed above. More detailed studies focusing on the photon energy dependence of π^0 peak position are carried out in [122], which finds a few percent rise of the peak position with increasing photon energy.

Data quality checks are important to ensure a homogeneous measurement and are carried out in parallel with calibration procedures, which involve rather basic detector information. To this end, runs exhibiting strange or unexpected behavior are discarded. The potential loss of statistics is typically compensated by smaller systematic errors. Some examples for such experimental deficiencies are given in the following.

[23] For example, the number of clusters in CB is fixed to 2 to reduce combinatorial background in figure 4.11 whereas for the calibration all pairs of clusters in CB are taken into account to obtain sufficient statistics in each detector channel.

- The DAQ is triggered from the analog sum of the signals in CB, the so-called energy sum trigger, and has been set to roughly 550 MeV. After the July/August beam-time it has been discovered [123] that crystals with element numbers 352 to 415 did not contribute to this sum due to a bad electrical connection within the analog sum chain, which has been fixed for the October and December beam-times. This trigger inefficiency is reflected in the MC simulation by ignoring the corresponding elements in the summation of the energy in CB.

- During the timing calibration, some of the runs exhibited sudden shifts of the coincident peaks for detectors using CATCH TDCs. The data is not easily recoverable as those shifts cannot be interpreted as single bit flips in the binary representation of the raw value ξ in equation (4.15). It is attributed to a still unresolved bug in the COMPASS read-out system and has been mitigated during data taking by restarting the run immediately if such a shift appeared. The affected runs are excluded from the analysis and comprise the largest part of discarded runs in table 4.2.

- The CB time-walk calibration tests if the timing and energy measurement of elements are properly correlated. For some channels, only the TDC measurement appeared to be broken. Those elements are not ignored completely but flagged as "BadTDC", such that energy measurements larger than 7 MeV are still taken into account during reconstruction, ignoring timing information. On MC, such elements are treated as normally working.

- During time-dependent calibration of the calorimeters, few channels are found not working over the full beam-time or an automatic stable fit becomes impossible and needs permanent user intervention, see figure 4.9. Those elements are accordingly either flagged as "Broken", if becoming dead completely, or as "NoCalibFill" or "NoCalibUseDefault" otherwise. The choice "NoCalibFill" excludes them from further energy gain tuning and their gain is set to an average of the neighbors, relying on the homogeneous detector response due to the separately carried out HV tuning. The preferable choice "NoCalibUseDefault" uses the gain from the time-independent calibration.

In total, the runs used for analysis are summarized in table 4.2, where also the calibration efforts from [91, 92] for the October and December beam-times are included. The status of CB and TAPS detector elements are given in figure 4.14 and parameters relevant for reconstruction and calibration are listed in table 4.3.

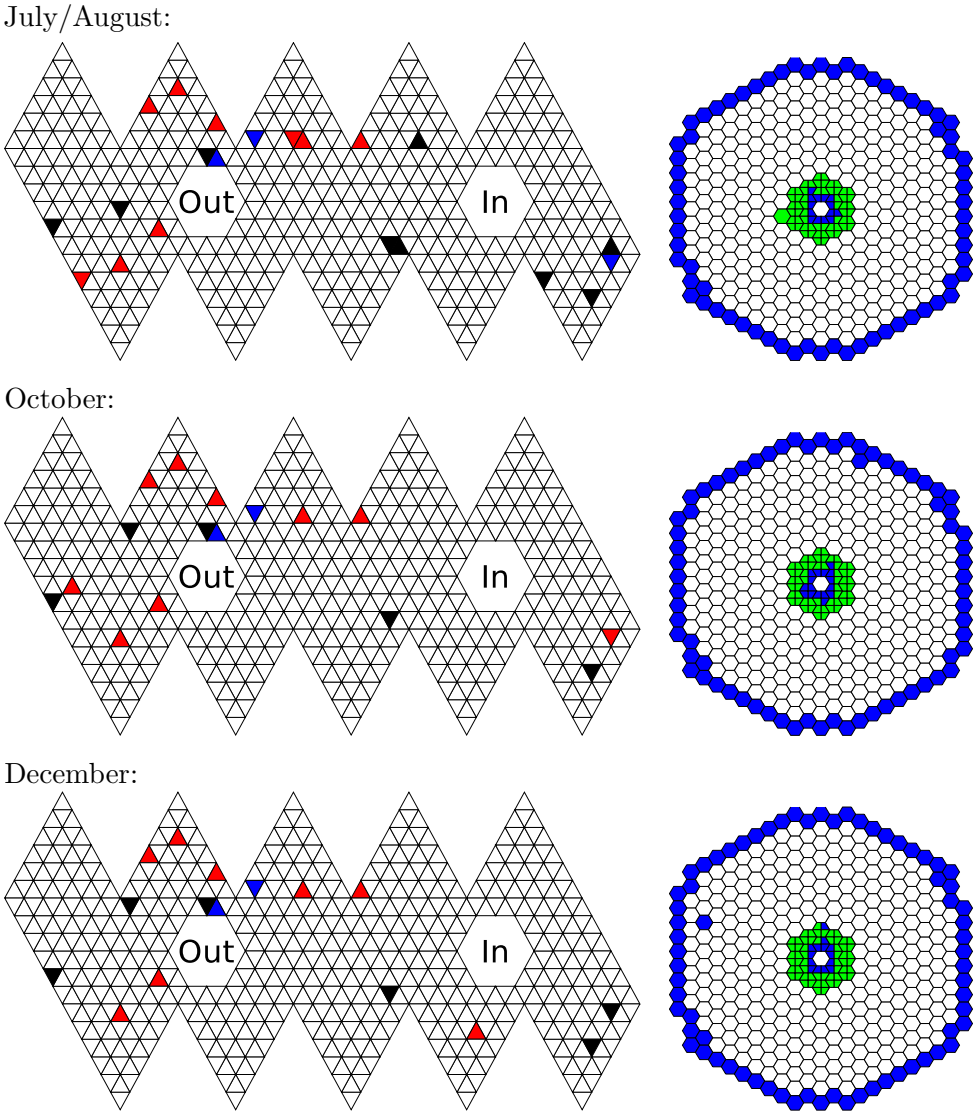

Figure 4.14.: Status of detector elements in CB and TAPS, shown for each of the three beam time periods defined in table 4.2. Filled black elements are flagged as "Broken" (dead elements), red means "BadTDC" (no timing but energy information in figure 4.7), blue means "NoCalibFill" (relative energy gain averaged from neighbors) and green means "NoCalibUseDefault" (time-*in*dependent gain used). See text for details.

Timing windows	EPT	$-125\,\text{ns}$ to $125\,\text{ns}$	see eq. (4.3)
	CB[a]	$-25\,\text{ns}$ to $25\,\text{ns}$	see eq. (4.7)
	PID	$-25\,\text{ns}$ to $40\,\text{ns}$	see fig. 4.8
	TAPS BaF_2	$-15\,\text{ns}$ to $15\,\text{ns}$	
	TAPS $PbWO_4$	$-25\,\text{ns}$ to $25\,\text{ns}$	
	TAPS Veto	$-12\,\text{ns}$ to $12\,\text{ns}$	
Thresholds	CB MC[b]	$> 1.2\,\text{MeV}$	
	TAPS MC[b]	$> 3.4\,\text{MeV}$	
	PID Raw	> 15	see fig. 4.8
	TAPS BaF_2 Raw	> 5	
	CB Broken TDC[c]	$> 7\,\text{MeV}$	
	CB Cluster	$> 12\,\text{MeV}$	
	TAPS Cluster	$> 12\,\text{MeV}$	

[a] For elements with working TDC and after time-walk correction.
[b] Mimics the hardware thresholds for single elements on MC.
[c] On Data, single crystal energy deposition reaching this threshold is not discarded if marked as broken TDC in CB. Not mimicked on MC.

Table 4.3.: Overview of setup parameters relevant for event reconstruction and calibration. Timing windows are chosen as tight as possible without risking to cut into coincidence peaks taking into account slightly drifting timing offsets. Thresholds are for example applied to mimic data behavior on MC due to hardware thresholds originating from discriminators, or to discard unphysical pedestal contributions. The settings are identically specified in Ant for all EPT beam-times.

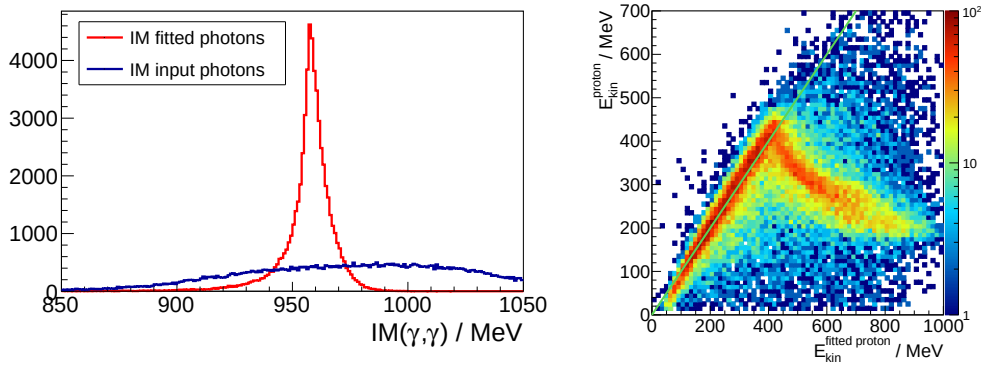

Figure 4.15.: The kinematic fitting procedure tremendously narrows the peak width of the invariant mass of two photons generated from $\eta' \to \gamma\gamma$ with EPT photon energies and reconstructed according to the detector simulation. Similarly, shown on the right for direct $2\pi^0$ production events, the kinetic energy of the proton is restored from punch-through by the kinematic fit.

4.5. Kinematic fitting

In comparison to typical analyses in A2 investigating π^0 or η production and their decays, the EPT beam-times targeted at η' production require the kinematic fitting technique to obtain a sufficient resolution in invariant mass spectra, as exemplary shown in figure 4.15. To this end, for each electron hit in the EPT TDCs corresponding to an incident photon energy E_γ, a kinematic fit with the energy-momentum conservation constraint is carried out, imposing

$$\begin{pmatrix} E_\gamma \\ 0 \\ 0 \\ E_\gamma \end{pmatrix}^\mu + \begin{pmatrix} m_{\text{proton}} \\ 0 \\ 0 \\ 0 \end{pmatrix}^\mu = p^\mu_{\text{proton}} + \sum_{\text{photons}} p^\mu \,, \quad \mu = 0,1,2,3\,. \tag{4.20}$$

The initial state represents a photon traveling along the z-axis with energy E_γ and a proton at rest. The parametrization of the final state proton and the final state photons depends on the calorimeter as depicted in figure 4.16. For CB, the quadruple $(1/E_{\text{kin}}, \theta, \phi, R)$ is used, where R is the radius of the cluster position in spherical coordinates including the shower depth s, so

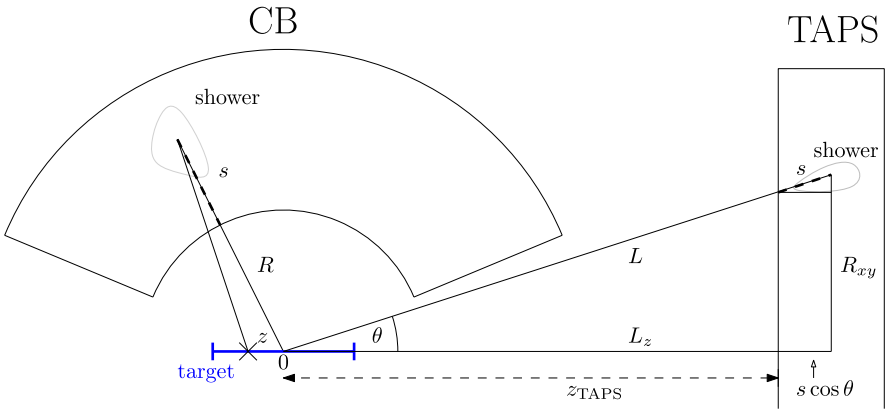

Figure 4.16.: The kinematic fitter uses four degrees of freedom to describe each candidate depending if the electromagnetic shower is reconstructed in either in CB or in TAPS to account for the spherical and forward-wall geometry, respectively. The target length of 10 cm is not negligible compared to the inner radius of CB, $R_{\mathrm{CB}} = 25.4\,\mathrm{cm}$ (sketch not to scale). The distance of the front-face of TAPS to the target center is $z_{\mathrm{TAPS}} = 145.7\,\mathrm{cm}$.

$R = R_{\mathrm{CB}} + s$. For TAPS, the quadruple $(1/E_{\mathrm{kin}}, R_{xy}, \phi, L)$ is used, where[24] $R_{xy} = L\sin\theta$, $L = \sqrt{x^2 + y^2 + L_z^2}$ and L_z is the distance of the cluster from the target center in z-direction including the shower depth. Choosing the inverse kinetic energy $1/E_{\mathrm{kin}}$ as a parameter avoids unphysical negative kinetic energies during optimization.[25] The shower depth $s(E_{\mathrm{kin}})$ is determined from GEANT-based single-particle simulations as a function of the cluster energy E_{kin} [123] as used in [125–127]. This parametrization allows for a calculation of the Lorentz four momenta $p^\mu = (E = E_{\mathrm{kin}} + m, \vec{p} = p\vec{x}/\,|\vec{x}|)$ required for the constraint in equation (4.20) of a final state particle with rest mass m, momentum $p = \sqrt{E^2 - m^2}$ and cluster position $\vec{x}$. Taking into account a production vertex at $\vec{v} = (0, 0, z_{\mathrm{v}})$, where z_{v} is an additional parameter in the kinematic fit, the cluster position is calculated from the parametrization as

$$\vec{x} = -\vec{v} + \begin{cases} \Big(R\cos\phi\sin\theta, R\sin\phi\sin\theta, R\cos\theta\Big) & \text{for CB}\,, \\ \Big(R_{xy}\cos\phi, R_{xy}\sin\phi, L_z = \sqrt{L^2 - R_{xy}}\Big) & \text{for TAPS}\,. \end{cases} \tag{4.21}$$

[24] The input cluster position $\vec{x} = (x, y, z = z_{\mathrm{TAPS}})$ in TAPS is already corrected in x and y for the shower depth skew due to the forward wall geometry [104, 124], see also figure 4.16.

[25] The uncertainty for the inverse kinetic $\sigma(1/E_{\mathrm{kin}})$ energy is propagated from the given uncertainty for E_{kin} as $\sigma(1/E_{\mathrm{kin}}) = \sigma(E_{\mathrm{kin}})/E_{\mathrm{kin}}^2$.

The proton kinetic energy in TAPS or CB is not correctly measured for energies above 400 MeV since the hadronic shower of the proton is not entirely contained within the crystals, an effect called "punch-through", see also figure 4.15. Thus, the kinematic fit treats the proton kinetic energy as unmeasured, that means it sets its uncertainty to $\sigma = 0$, and its initial value $E_{\mathrm{kin}}^{\mathrm{init}}$ is set by means of the missing momentum $\vec{p}_{\mathrm{miss}} = (0, 0, E_\gamma) - \sum_{\mathrm{photons}} \vec{p}$ for the proton, see equation (4.20), so $E_{\mathrm{kin}}^{\mathrm{init}} = \sqrt{m_{\mathrm{p}}^2 + \vec{p}_{\mathrm{miss}}^{\,2}} - m_{\mathrm{p}}$ with the proton rest mass m_{p}. This prevents the fit procedure from converging to an unphysical local minimum.

Furthermore, the z position of the interaction varies between ± 5 cm due to the finite target length of 10 cm, which is not negligible compared to the inner radius of CB, $R_{\mathrm{CB}} = 25.4$ cm.[26] Taking this into account in the fitter improves the invariant mass resolution as the systematic error in the determination of the polar angle θ is compensated. The fitting procedure shows slightly better convergence rate when the z-vertex position at $z_{\mathrm{v}} = 0$ is assumed as "measured" with an uncertainty of 3 cm $\approx 10\,\mathrm{cm}/\sqrt{12}$, in comparison to choosing the z-vertex to be unmeasured.[27]

Determining the uncertainties for the proton and the photons in the two calorimeters CB and TAPS, given the already discussed parametrization, is far from being trivial. If one assumes a sufficient description of the detector resolutions within the MC simulation, a single particle gun with subsequent comparison to the generated information could potentially provide those uncertainties. Even in this ideal situation, the non-Gaussian tail towards lower energies of the measured kinetic energy distribution is difficult to account for,[28] see also figure 4.5 on page 72. Within this thesis, a data-driven approach to study and iteratively tune the uncertainties based on events identified as $2\pi^0$ production[29] was developed. To this end, for each parameter denoted as x, such as $1/E_{\mathrm{kin}}$ for photons in CB or R_{xy} for protons in TAPS, the distribution

[26] The lateral extent of the photon beam spot with a diameter of roughly 1.3 cm is neglected.

[27] The more "natural" parametrization $(E_{\mathrm{kin}}, \theta, \phi)$ suffers from the projective geometry of crystals in CB pointing towards the origin and *not* to the interaction vertex. Despite correcting for this systematic error in $\theta(z_{\mathrm{v}})$ with single photon detector simulations, this simple parametrization remains inferior to the currently employed one for an unknown reason, in particular for lower photon multiplicities such as 2 or 4.

[28] Additionally, the simulation needs to extract a shower depth, as the fourth parameter is a measured input to the kinematic fitter. The shower depth is currently implemented as a polynomial parametrization depending on the kinetic energy [123].

[29] According to equation (4.8) on page 63 with the replacement $m_{\eta'} \to m_{\pi^0}$, single π^0 production does not cover the proton phase space sufficiently for EPT photon energies, and $3\pi^0$ production suffers from a comparatively small cross-section. Thus, the choice of $2\pi^0$ represents a compromise between phase space coverage and statistics.

of the pull p_x defined as follows [111, 128] is investigated,

$$p_x = \frac{x^{\mathrm{f}} - x^{\mathrm{i}}}{\sqrt{(\sigma_x^{\mathrm{i}})^2 - (\sigma_x^{\mathrm{f}})^2}}\,, \tag{4.22}$$

where x^{i} and x^{f} are the values of parameter x before and after the fit, respectively, and $(\sigma_x^{\mathrm{i/f}})^2$ are the corresponding squared uncertainties given as the diagonal elements of the covariance matrix. The starting uncertainty model, which only depends on the input cluster energy E_{kin} for photons and is constant for protons, is taken from [123, 125]. For each iteration, the mean value of the uncertainty $\langle\sigma_x\rangle$ is relatively increased (decreased) if the RMS of the pull distribution[30] is larger (smaller) than the target value of 1. The mean value of the uncertainty $\langle\sigma_x\rangle$ is determined in bins of $(E_{\mathrm{kin}}, \cos\theta)$ for photons, as shown figure 4.17 for CB, and in bins of $(\cos\theta)$ for protons, as their kinetic energy is unknown due to the punch-through effect. The bin sizes are chosen small enough such that the average $\langle\ldots\rangle$ is meaningful and chosen large enough to avoid statistical fluctuations in the RMS determination, which is additionally mitigated by a bi-cubic interpolation over the binning and by the removal of fluctuating bins at the edge of the $2\pi^0$ production phase space. For the parameters R in CB and L in TAPS, which depend on the shower depth s as explained, the offset of the pull distribution with target value 0 is ensured by adjusting the mean value $\langle s\rangle$ iteratively. Despite the careful adjustment of additional MC smearing parameters as described in section 4.4, the pull distributions for simulated input do not show unit RMS and zero offset if the uncertainties determined from data are used. Thus, the identical procedure is applied to determine a separate set of uncertainties for MC input as shown in figure 4.18, again using the MC cocktail. The final χ^2-probability distribution returned by the kinematic fitter for protons and photons in both calorimeters is shown in figure 4.19, which is expected to be uniformly distributed. The technical implementation of this tuning in Ant is similar to the iterative improvement of the additional MC smearing, as mentioned in section 4.4.

Besides the four kinematic constraints in equation (4.20), which coin the name 4C fit[31], additional conditions on the final state particles can be imposed. For example, if two photons with Lorentz vectors $p_1^\mu = (E_1, \vec{p}_1)$ and $p_2^\mu =$

[30] Data is prompt-random subtracted by weighting it according to equation (4.3). The fit probability must be larger than 1 % to suppress background and the z-Vertex is set to unmeasured to avoid skewing the uncertainties in θ.

[31] Although the proton kinetic energy and the z-Vertex are free parameters, the number of constraints associated with Lagrange multipliers is used here.

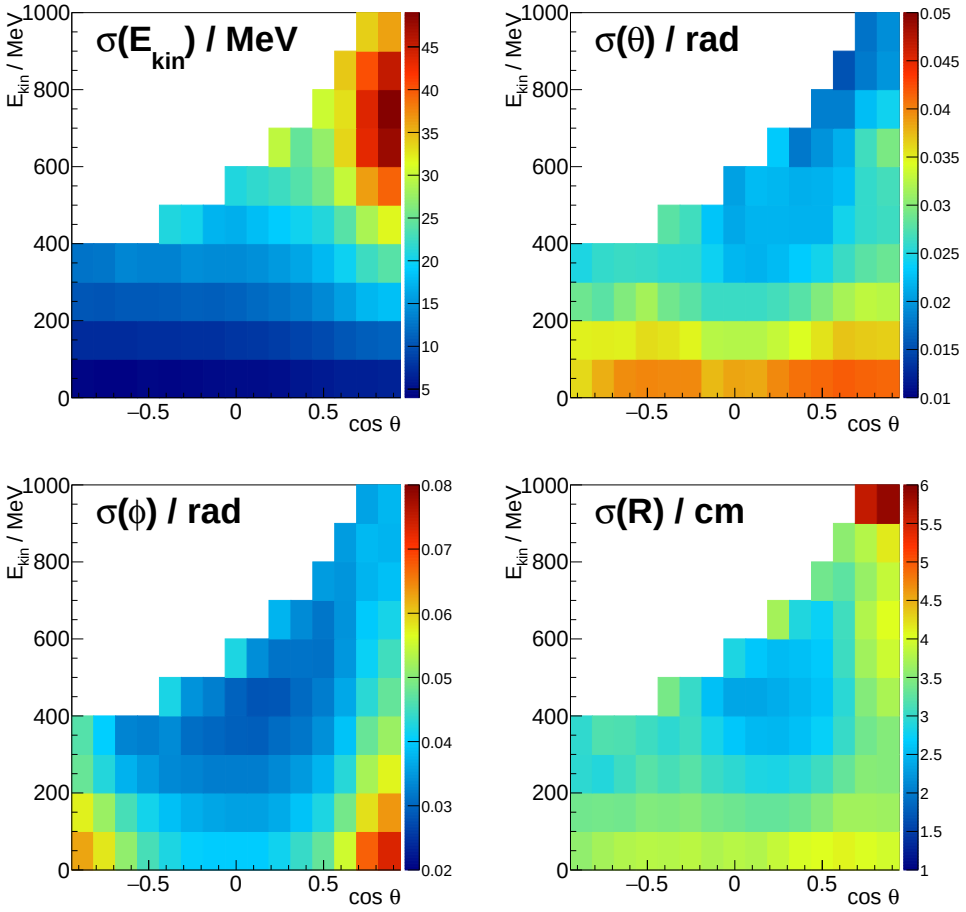

Figure 4.17.: The final fitter uncertainties of the four parameters $(E_{\mathrm{kin}}, \theta, \phi, R)$ are shown for photons reconstructed in CB, for measured data. Regions with insufficient statistics are not filled and the rather coarse binning is mitigated with a two-dimensional cubic interpolation over $(E_{\mathrm{kin}}, \cos\theta)$. Compare also figure 4.18 for MC.

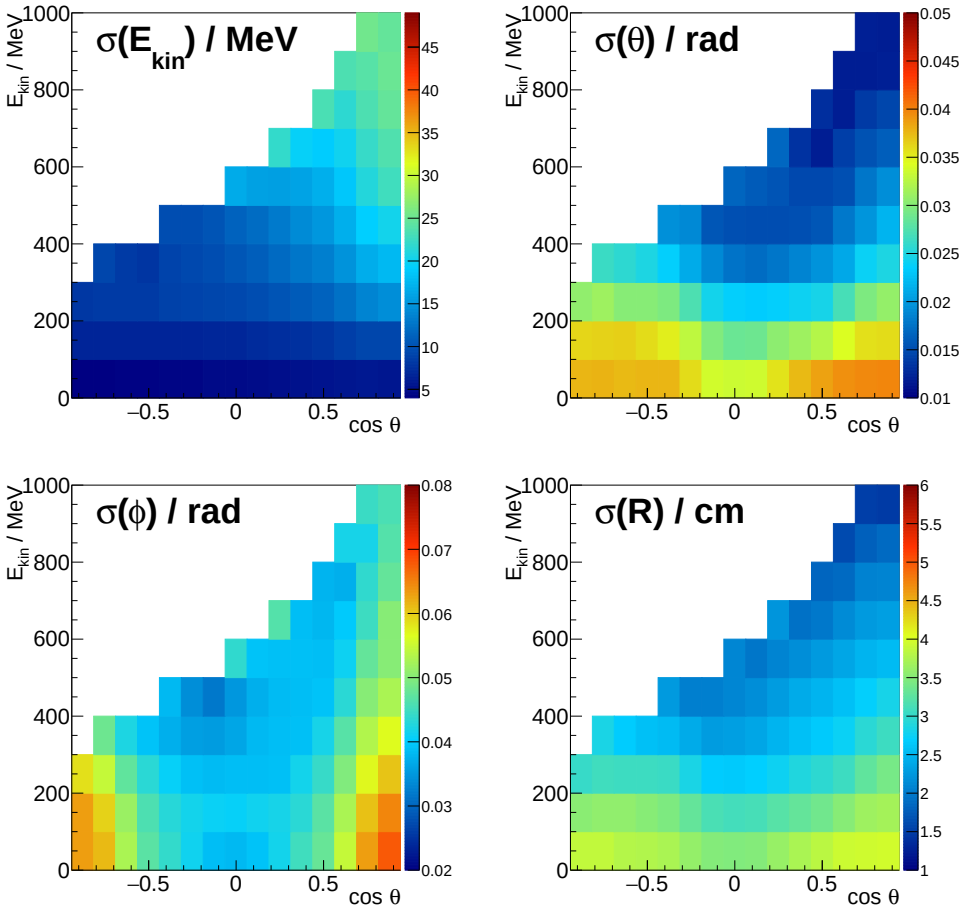

Figure 4.18.: The final fitter uncertainties are shown for photons reconstructed in CB, for MC. See figure 4.17 on the previous page for data.

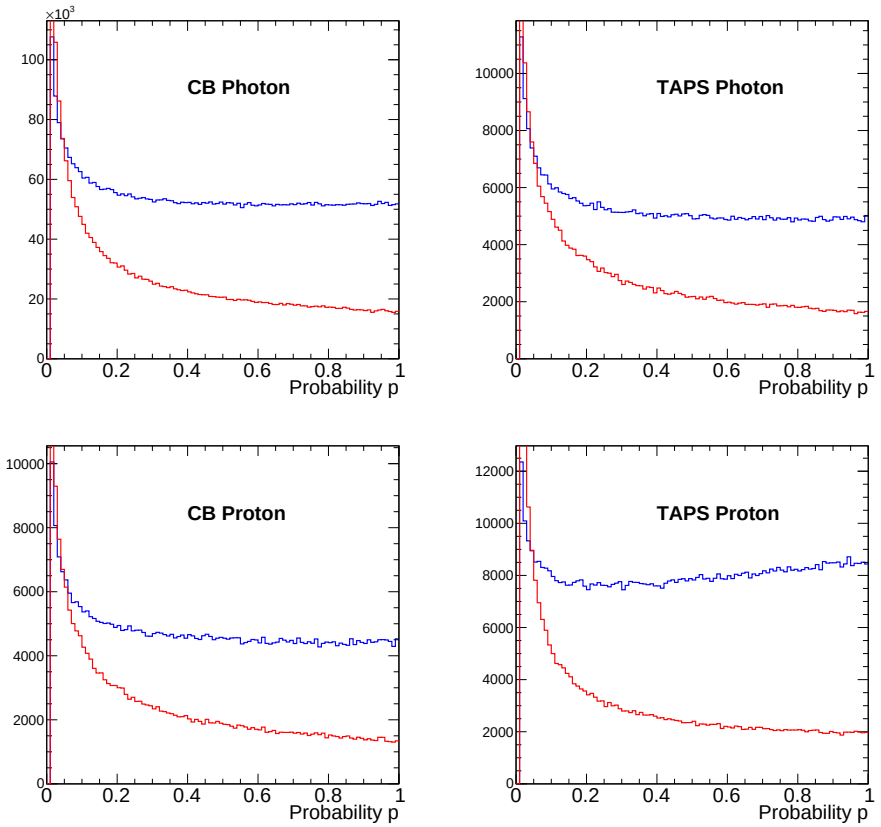

Figure 4.19.: For protons and photons reconstructed in CB and TAPS, the kinematic fit probability is shown for data (red line) and MC (blue line). If the uncertainties are correctly modeled to obtain pull distributions with unit variance and zero mean, a uniform distribution is expected for the probability, assuming the parameters have indeed Gaussian uncertainties. MC is scaled such to have the same integral in $0.01 < p < 0.1$. The rise towards lower p is due to backgrounds not fulfilling the kinematic fit constraint.

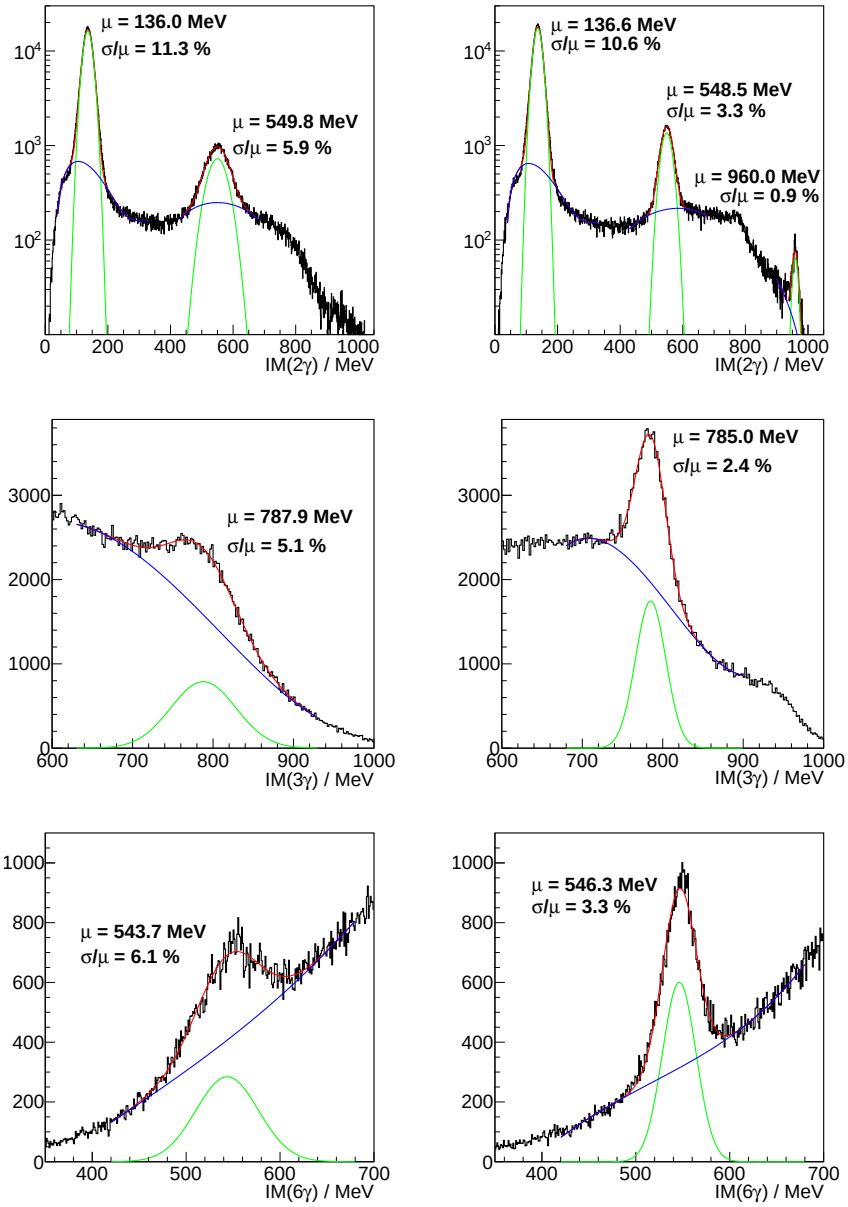

Figure 4.20.: Prompt-random subtracted invariant mass plots on 7 % of all 2014 EPT beam-time data. Left column before kinematic fit, right after. Top row shows the 2γ decays of pseudo-scalars with nominal masses $m_{\pi^0} \approx 135.0\,\text{MeV}$, $m_\eta \approx 547.9\,\text{MeV}$, $m_{\eta'} \approx 957.8\,\text{MeV}$ [17]. Middle shows the $\omega \to \pi^0\gamma \to 3\gamma$ decay with nominal mass $m_\omega \approx 782.7\,\text{MeV}$ [17]. Bottom shows the $\eta \to 3\pi^0 \to 6\gamma$ decay. See also figure 4.13 on page 84.

$(E_2, \vec{p}_2)$, respectively, are required to originate from a π^0 decay, the constraint

$$(p_1 + p_2)^2 = (E_1 - E_2)^2 - (\vec{p}_1 - \vec{p}_2)^2 \stackrel{!}{=} m_{\pi^0}^2 \tag{4.23}$$

is added to the 4C fit, making it a 5C fit. As a specific reaction with decays of intermediate particles can be represented as a tree, or directed acyclic graph, a kinematic fit including n invariant mass constraints is called a $(4+n)$C tree fit in the following. As there are typically additional photons not belonging to the π^0 in the example above, the fit is carried out for all possible permutations of all leaf photons, as discussed in detail in section 4.7. This significantly increases the computational cost of decay tree fitting compared to simple kinematic fitting. Additionally, the optimization becomes harder as invariant mass constraints such as equation (4.23) are non-linear in terms of the parametrization.

A comprehensive study of the kinematic fitter is depicted in figure 4.20. A sufficiently large part of the EPT beam-time data is analyzed and invariant masses of the photons for the event multiplicities $2+1$, $3+1$ and $6+1$ are investigated. The proton is selected as the best kinematic fit out of all candidate permutations, see section 4.6 for details. For example, events with $2+1=3$ candidates have 2 photons and thus show the prominent 2γ decay of pseudo-scalar neutral mesons, $\pi^0, \eta, \eta' \to 2\gamma$. All fitted peak positions are within less than 1 % before and after the kinematic owing to the careful calibration presented in section 4.4. As discussed in more detail in section 4.7, the correct positions are important for the invariant mass constraints as given in equation (4.23), where the nominal masses are used.

4.6. Selection of $\eta' \to \gamma\gamma$ events

As already outlined in section 4.1, the decay $\eta' \to \gamma\gamma$ is used as a reference channel for the analysis of the $\eta' \to \omega\gamma$ channel. This section presents the selection of $\eta' \to \gamma\gamma$ events and also covers the basic event selection common to both decay channels. In principle, the analysis strategy identifies two photons and one proton in the final state, and extracts the number of events $N(\eta' \to \gamma\gamma)$, see equation (4.6) on page 63, by fitting the η' peak in the invariant mass spectrum of the two photons above possible background. Correspondingly, the reconstruction efficiency $\varepsilon(\eta' \to \gamma\gamma)$ is determined by MC simulation as the number of reconstructed events divided by the number of generated $\eta' \to \gamma\gamma$ events. The latter is chosen sufficiently large to minimize the statistical uncertainty of the efficiency, which is neglected in the following.

The kinematic fit, without any additional invariant mass constraints, serves two purposes. First, it increases the resolution of the invariant mass peak

```
if not at least one candidate in TAPS then next
foreach tagger hit do
    foreach candidate as proton do
        use remaining candidates as photons if θ > 7°
        if discarded energy more than 70 MeV then next
        if photon invariant mass less than 600 MeV then next
        if missing mass outside 350 MeV proton window then next
        run kinematic fit for γp → p 2γ
        if larger fit probablity found then
            compute and store values, such as invariant mass of 2γ after
             fit
    if best fit probablity greater than 0.005 then
        write out values to file
```

Figure 4.21.: Processing of an event consisting of candidates and tagger electron hits for the reference channel $\eta' \to \gamma\gamma$. Statements with trailing "then next" are wide pre-filtering cuts to increase analysis speed and limit output file sizes. The first statement accounts for the proton of η' production always being reconstructed in TAPS, see figure 4.3.

significantly as shown in figure 4.15, and second it is used to identify the proton. This choice of particle identification is robust against ΔE detector inefficiencies, such as the PID, and badly modeled detector responses in MC, which is in particular problematic for the TAPS Veto detector. Furthermore, ToF and PSA in TAPS are also insufficiently modeled. The identification with the kinematic fitter is accomplished by testing all candidates of an event as the proton while the remaining candidates are interpreted as photons, comprising a list of proton-photons combinations. At this step, the photons are sorted by decreasing kinetic energy and only the first two are taken into account in order to match the reference channel signature having two photons in the final state. The kinetic energy of the remaining photons is summed up, which is denoted as `DiscardedEk`, see also the summary in table 4.4. Eventually, the kinematic fit is carried out for each of the proton-photons combination and the one with the highest probability is selected. The complete procedure yielding the output for the reference channel analysis is shown in figure 4.21.

As the η' production close to threshold is significantly influenced by the kinematic fit, it is important to model the production mechanism as well as possible on MC to obtain a correct reconstruction efficiency. To this end, the

`DiscardedEk`	Sum of kinetic energy of discarded photons to obtain desired multiplicity (2γ for reference, 4γ for signal)
`KinFitProb`	Best kinematic fit probability over proton-photons combinations, see figures 4.21 and 4.27
`CBSumVetoE`	Sum of veto energies for photons reconstructed in CB
`AntiPi0FitProb`	Best tree fit probability for $\pi^0\pi^0$ background hypothesis
`AntiEtaFitProb`	Best tree fit probability for $\pi^0\eta$ background hypothesis
`TreeFitProb`	Best tree fit probability for $\eta' \to \omega\gamma$ hypothesis, see text for specific invariant mass constraints
`gNonPi0_1/2`	Kinematic (E_{kin}, θ) cut on photons *not* originating from π^0 for $\eta' \to \omega\gamma$ hypothesis, variant 1/2 (see text)
`IM_Pi0g[1]`	The higher invariant mass combination of the two bachelor photons with the fitted π^0 four-vector (see text)

Table 4.4.: The various cut variables are summarized as used in sections 4.6 and 4.7. Variables below the separator are solely used in section 4.7 and explained there.

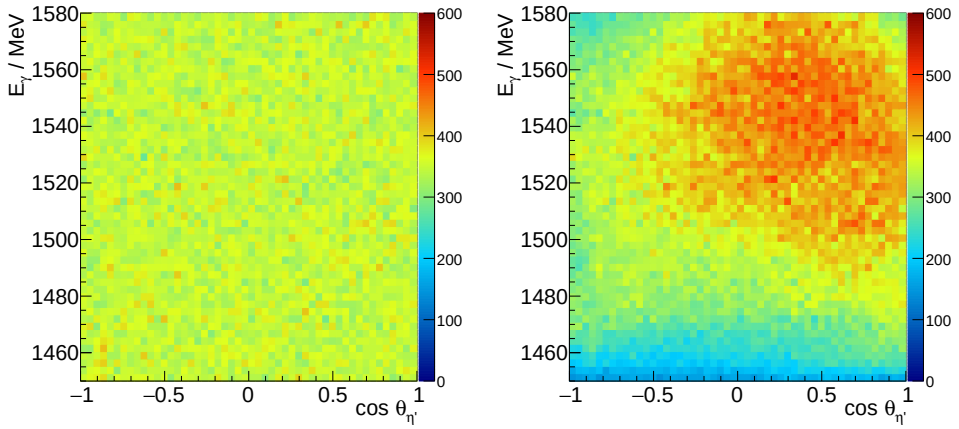

Figure 4.22.: The MC generated events are uniformly distributed (left panel) and then weighted to account for the $(E_\gamma, \cos\theta_{\eta'})$-dependent production of the η' close to threshold (right panel). The shape is taken from [127] as fitted Legendre polynomials [129]. The integral in *both* plots equals the number of generated events, 9×10^5.

efficiency corrected numbers for $\gamma p \to p\eta'$ on the 2014 EPT beam-times from [127] are fitted to Legendre polynomials [129]. The shape in $(E_\gamma, \cos\theta_{\eta'})$, where E_γ is the incoming photon energy and $\theta_{\eta'}$ is the η' polar angle in the center-of-mass frame, is reproduced by properly weighting with a two-dimensional probability density function. Accordingly, the generated events are uniformly distributed in $(E_\gamma, \cos\theta_{\eta'})$, see figure 4.22, and the weights are normalized such that the total number of input events is conserved. The experiment trigger is mimicked on MC generated events by choosing a Gaussian-distributed CB energy sum threshold with $\mu = 540\,\text{MeV}$ and $\sigma = 52\,\text{MeV}$ [123, 130], compare also table 4.1. Those parameters do not influence the reconstruction efficiency significantly since both the reactions $\eta' \to \gamma\gamma$ and $\eta' \to \omega\gamma$ deposit kinetic energies well above the trigger threshold.[32]

In order to reduce background and obtain a clearly visible η' peak in the invariant mass spectrum, the discarded kinetic energy is required to vanish, denoted as `DiscardedEk=0`, and the kinematic fit probability for the best proton-photon combination must exceed 2 %, denoted as `KinFitProb>0.02`. The effect of those cuts on the full dataset is shown in figure 4.23 and compared to the MC cocktail. Although the cocktail is based on known production cross-sections and branching fractions of the decays [92], the two main background channels, direct $2\pi^0$ and direct $\eta\pi^0$ production, $\gamma p \to p\pi^0\pi^0 \to p4\gamma$ and $\gamma p \to p\pi^0\eta \to p4\gamma$, respectively, are scaled by a factor of 20 to match the signal-to-background ratio as given by data. Currently, the reason for this large scaling factor is not known but hints at an insufficient understanding of the cluster multiplicities or the kinematic fitter, as discussed further in section 4.8.

The number of $\eta' \to \gamma\gamma$ events is determined by fitting the peak close to the rest mass of the η' in the invariant mass spectrum of two photons, denoted as IM(2γ) or short IM if the photon multiplicity is obvious from the context. The binned extended likelihood fits are carried out per EPT detector channel, which corresponds to fixed incident photon energies E_γ. This enables modeling of the phase-space background close to threshold by the ARGUS probability density function (PDF),

$$f(x) = N \cdot \begin{cases} x\Big(1-(x/x_0)^2\Big)^p \exp\Big(\chi(1-(x/x_0)^2)\Big) & \text{if } 0 \le x \le x_0 \\ 0 & \text{otherwise} \end{cases}, \quad (4.24)$$

where $\chi < 0$ and $p = 1/2$ control the shape, x_0 is a cut-off parameter and

[32] The analog sum signal used to trigger the read-out is not directly measured in the experimental setup, see figure 2.11 on page 29. This inhibits a more careful investigation at this point.

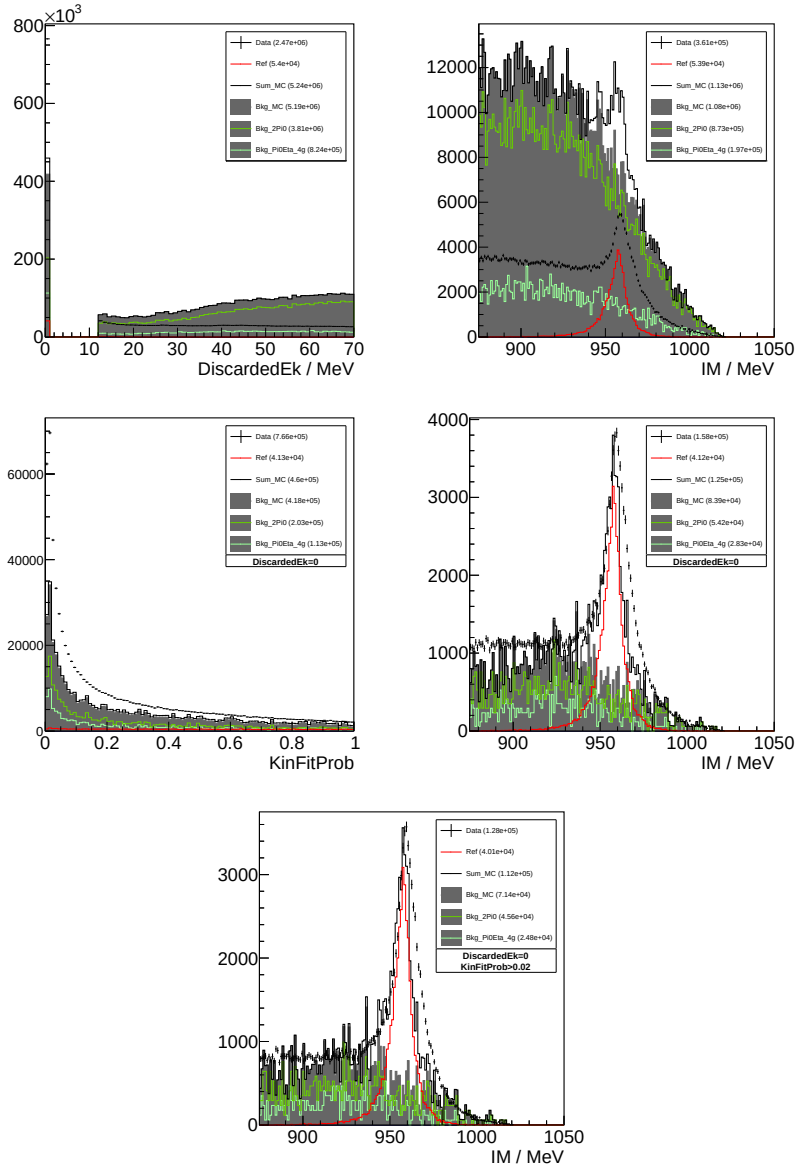

Figure 4.23.: The applied cuts are shown in each row for the reference channel $\eta' \to \gamma\gamma$. Below the legend, the cut conditions are specified according to table 4.4. The sum of all MC channels (black line `Sum_MC`) are scaled to match the data points in the bottom row panel with the final cut choice applied. `Ref` denotes the channel $\eta' \to \gamma\gamma$, `Bkg_2Pi0` the channel $\gamma p \to p\pi^0\pi^0 \to p4\gamma$ and `Bkg_Pi0Eta_4g` the channel $\gamma p \to p\pi^0\eta \to p4\gamma$. Note the implicitly applied cuts as described in figure 4.21.

the normalization N ensures $\int_{-\infty}^{\infty} f(x)dx = 1$. Choosing $p \neq 1/2$ generalizes the originally proposed ARGUS PDF in [131], which is exploited later in section 4.7. The parameter x_0 is fixed during the fit to the maximum invariant mass given by

$$x_0(E_\gamma) = \sqrt{m_\mathrm{p}^2 + 2m_\mathrm{p}E_\gamma} - m_\mathrm{p}\,, \tag{4.25}$$

where $m_\mathrm{p} \approx 938\,\mathrm{MeV}$ is the rest mass of the target proton. The signal shape PDF to extract the number of $\eta' \to \gamma\gamma$ events is determined from MC[33], shifted with the parameter δ and convoluted with a Gaussian with width σ to account for remaining differences between data and MC.[34] The signal, background and total PDFs are summed separately over the EPT channels. The result for the chosen cut `DiscardedEk=0`, `KinFitProb>0.02` is shown in figure 4.24 including the input MC signal shape and prompt-random subtracted data. The corresponding fit parameters are shown in figure 4.25 and the fits per EPT channel are given in appendix A.

The final result for the number $\eta' \to \gamma\gamma$ events corrected for reconstruction efficiency reads

$$\#(\eta' \to \gamma\gamma) = N(\eta' \to \gamma\gamma)/\varepsilon(\eta' \to \gamma\gamma) = 112652 \pm 976_\mathrm{stat}\,. \tag{4.26}$$

This value is used as the reference for the $\eta' \to \omega\gamma$ branching ratio in section 4.7, according to equation (4.6). The selected cut choice is studied in figure 4.26. It shows that allowing surplus candidates in the events by non-vanishing `DiscardedEk` or changing the kinematic fit probability cut does not influence the resulting efficiency-corrected number of $\eta' \to \gamma\gamma$ events significantly. Additional cuts, such as `CBSumVetoE` using the PID information matched to CB clusters, have been studied to test the correctness of the MC detector response. A similar quantity, the `PIDSumE`, which is the energy sum of all PID elements ignoring CB cluster information, is not well-modeled in MC. This is attributed to the non-optimal handling of the PID signals leading to largely varying and broad pedestals, which are difficult to reproduce in the detector simulation, see also figure 4.8 on page 77.

4.7. Selection of $\eta' \to \omega\gamma$ events

The experimental setup of A2, in particular the calorimeters, is ideally suited for the detection of photons. Thus, the signal channel $\eta' \to \omega\gamma$ is investigated

[33] One third each of the 10^7 generated events is analyzed for the three beam-times to account for possible changes in the experimental setup, such as ignored elements, see figure 4.14.
[34] The package RooFit 3.60 is used to carry out those fits [132].

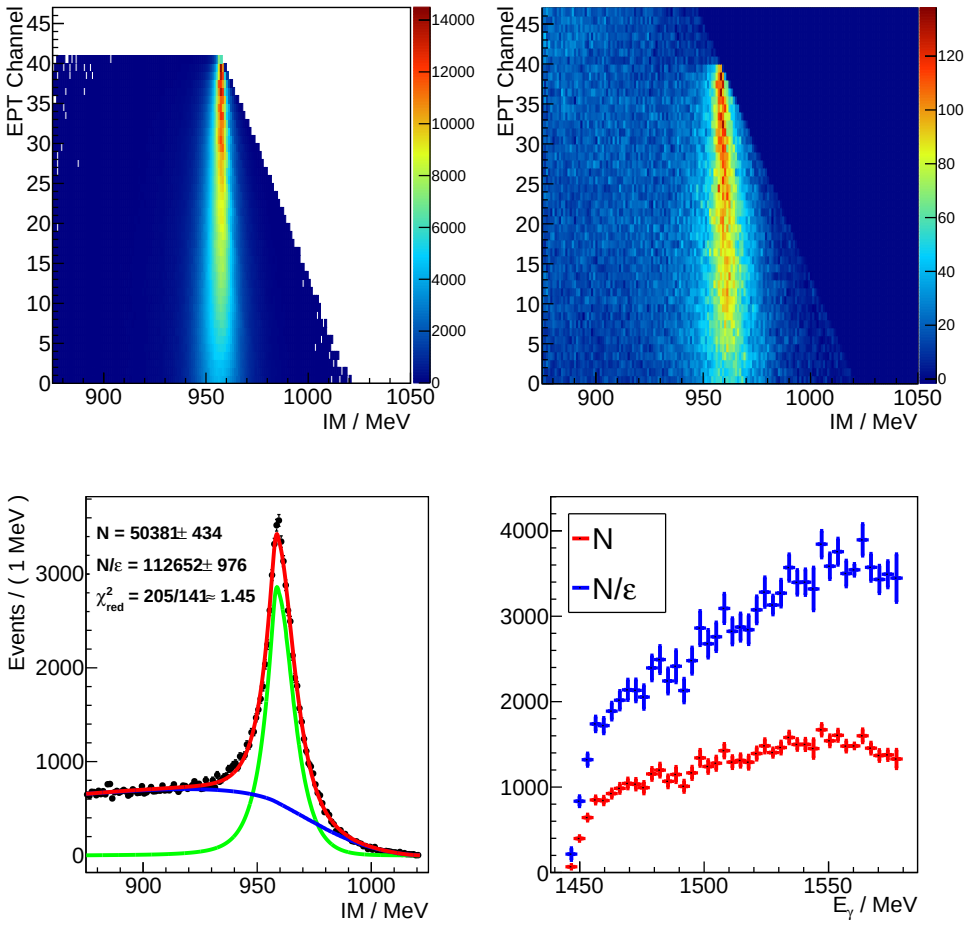

Figure 4.24.: The invariant mass of the kinematically fitted photons is used to extract the number of measured $\eta' \to \gamma\gamma$ events N and the efficiency-corrected value N/ε, as shown on the bottom right. The fits are carried out for each EPT channel with the corresponding MC signal shape, as given in the top row. The sum of all fits is displayed in the bottom left panel. The cut choice requires `DiscardedEk=0` and `KinFitProb>0.02`, see figure 4.23. The determined fit parameters are given in figure 4.25.

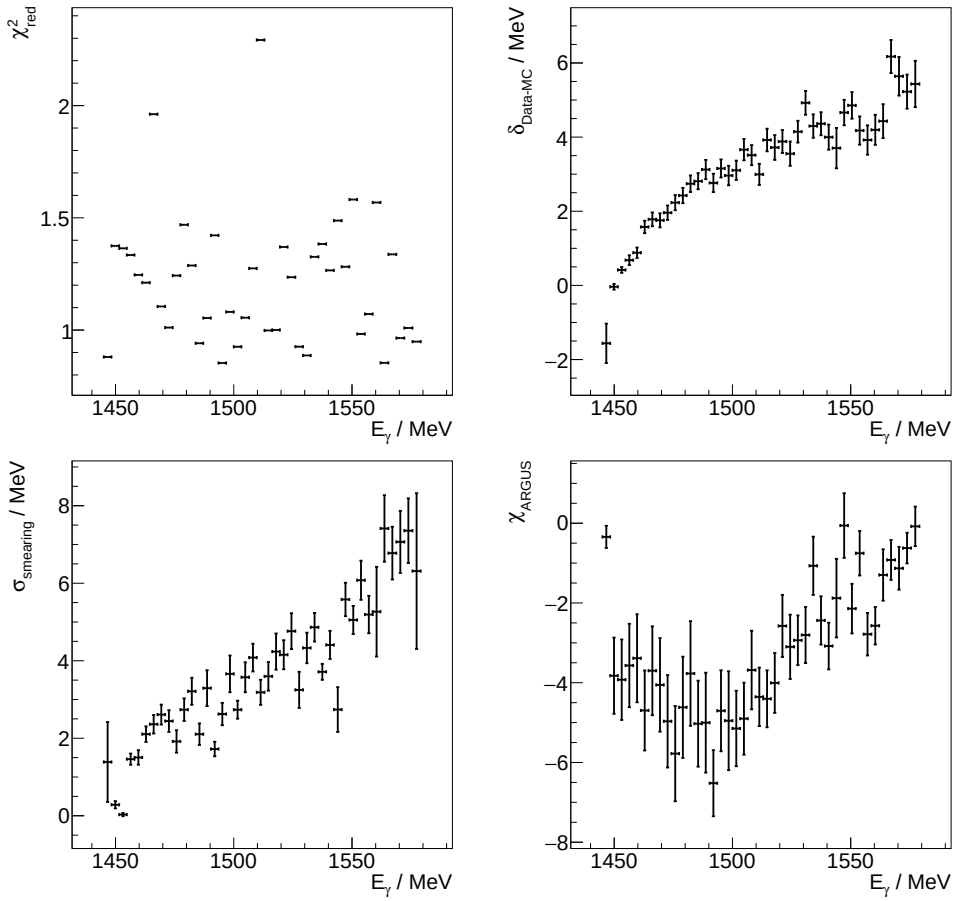

Figure 4.25.: Fit parameters including $\chi^2_{\text{red}} = \chi^2/\#(\text{d.o.f.})$ for each tagger channel corresponding to a certain incident photon energy range E_γ. See text for details.

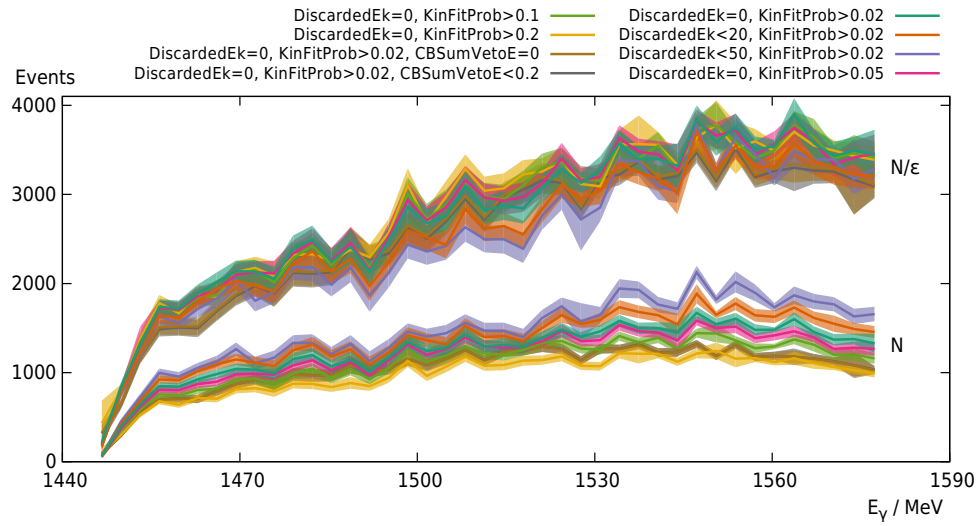

Figure 4.26.: For each cut choice color-coded by the legend on the top, the number of $\eta' \to \gamma\gamma$ events N extracted from the fit and the efficiency-corrected value N/ε are shown with 1σ error bands for each EPT channel corresponding to the incident photon energy E_γ. The cut variables are explained in table 4.4.

in the decay chain

$$\eta' \to \omega\gamma \to \pi^0\gamma\gamma \to 4\gamma\,, \tag{4.27}$$

where the expected candidate multiplicity is five including the proton. To calculate the number of signal events $N(\eta' \to \omega\gamma)$ in equation (4.6), the known branching fractions of the intermediate decays $\omega \to \pi^0\gamma$ and $\pi^0 \to \gamma\gamma$ are used [17],

$$\begin{aligned} \mathrm{BR}(\omega \to \pi^0\gamma) &= (8.28 \pm 0.28) \times 10^{-2}\,, \\ \mathrm{BR}(\pi^0 \to \gamma\gamma) &= (99.823 \pm 0.034) \times 10^{-2}\,, \end{aligned} \tag{4.28}$$

where the former contributes predominantly to the systematic uncertainty of the final result. The primary analysis strategy to extract the number of signal events is similar to section 4.6 as it searches for the η' peak in the invariant mass of the four photons, where two of them are subject to the π^0 constraint. This invariant mass is denoted as $\mathrm{IM}(\pi^0\gamma\gamma)$. Due to the higher photon multiplicity leading to larger background contributions and the at least 10 times lower number of expected signal events, the analysis contains various cuts to increase the signal-to-background ratio, as explained in the following.

```
if not at least one candidate in TAPS then next
foreach tagger hit do
    foreach candidate as proton do
        use remaining candidates as photons if θ > 7°
        if discarded energy more than 70 MeV then next
        if missing mass outside 350 MeV proton window then next
        store proton-photons combination
    foreach proton-photons combination do
        run kinematic fit for γp → p 4γ
    if best KinFit probability smaller than 0.005 then next
    foreach proton-photons combination do
        run 6C tree fit for γp → pπ⁰π⁰ → p 4γ
    if best AntiPi0Fit probability greater than 0.001 then next
    foreach proton-photons combination do
        run 6C tree fit for γp → pπ⁰η → p 4γ
    if best AntiEtaFit probability greater than 0.02 then next
    foreach proton-photons combination do
        run 5C tree fit for η' → ωγ with π⁰ constraint
        if larger TreeFit probablity found then
            compute and store values, such as invariant mass of 4γ after
             fit
    foreach proton-photons combination do
        run 6C tree fit for η' → ωγ with π⁰, ω constraint
        if larger TreeFit probablity found then
            compute and store values, such as η' bachelor photon energy
    if at least one tree fit successful then
        write out values to file
```

Figure 4.27.: Processing of an event consisting of candidates and tagger electron hits for the signal channel $\eta' \to \omega\gamma$. The various tree fits implicitly permute all photons assigned to the leaves, but skip permutations outside a window of 90 MeV for π^0 constraints and 200 MeV for η constraints to increase performance.

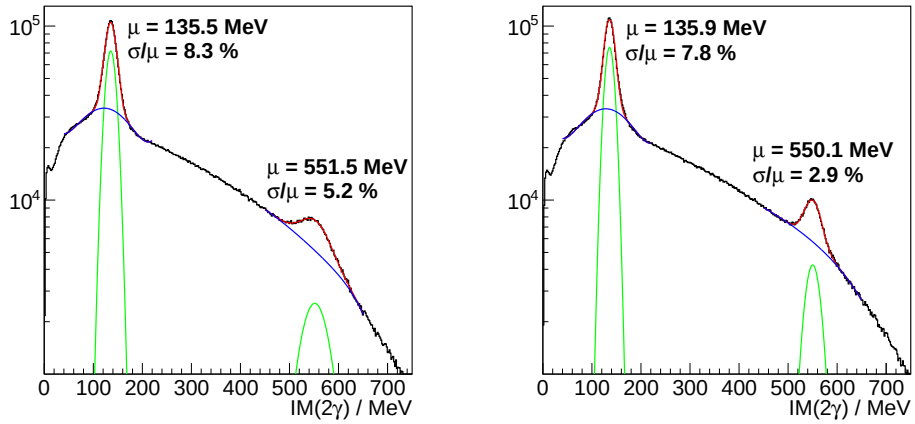

Figure 4.28.: Prompt-random subtracted 2γ out of 4γ invariant mass combinations on data, where the proton is identified with the best kinematic fit. Left panel shows before kinematic fit, right after the fit. The subsequent tree fits require that the π^0 and η peaks are close to the nominal masses. See also figure 4.13 on page 84.

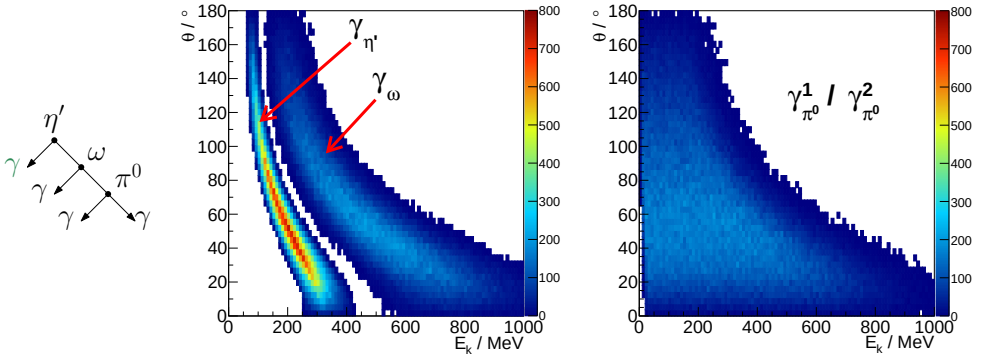

Figure 4.29.: The phase space distribution in kinetic energy E_k and polar angle θ of the final state photons for generated signal events is shown. γ_X indicates the photon originating from the meson $X = \eta', \omega, \pi^0$. $\gamma_{\eta'}$ and γ_ω are bachelor photons of the η' and ω, respectively.

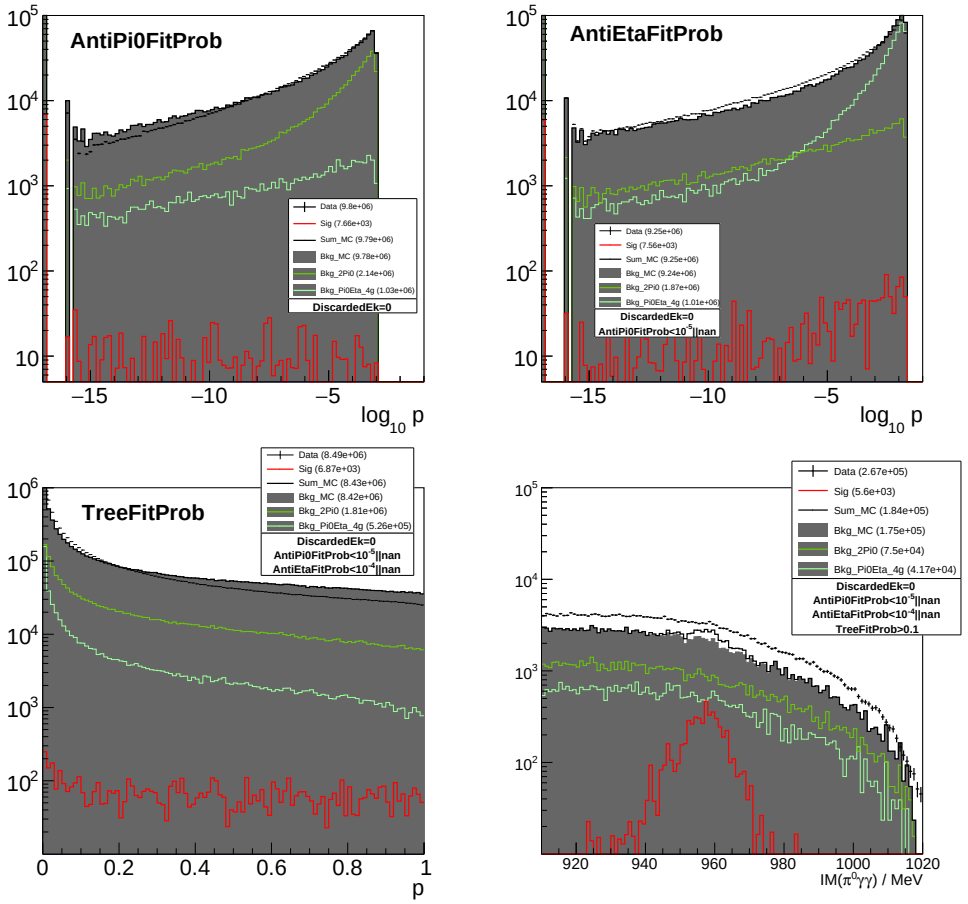

Figure 4.30.: The probability distribution for the two background-suppression fits and the 5C tree fit, constraining the π^0, are shown. On the bottom right, the resulting invariant mass spectrum after applying all probability cuts is displayed. More cuts are obviously needed to obtain a visible signal peak. The MC cocktail is scaled by a factor of 7.8 to roughly match the black data points, see also figure 4.23.

In order to discriminate direct $2\pi^0$ and direct $\eta\pi^0$ production, which are the dominant background contributions, the event is subjected to a 6C kinematic fit with the invariant mass constraints matching those background channel hypotheses. As shown in figure 4.28, the invariant mass constraints can be applied with the nominal masses without introducing a fit bias. The corresponding best fit probabilities, denoted as `AntiPi0FitProb` and `AntiEtaFitProb`, are required to be less than 10^{-5} and 10^{-4}, respectively. The event is also accepted if the fit has not converged, which is indicated by the trailing `||nan`. The signal decay tree, as depicted in figure 4.29, is primarily tested by requiring a single π^0 invariant mass constraint of two photon leaves as a 5C tree fit. As an alternative signal identification, the ω invariant mass of three photons is additionally constrained as a 6C tree fit. In addition to the proton selection, the leaves are correspondingly permuted over the photons and the tree fit with the highest probability is selected. The full analysis procedure is given in figure 4.27. The 6C tree fit should be handled with care due to the comparatively large decay width of the ω of about $\Gamma_\omega \approx 8\,\mathrm{MeV}$ [17] and is only used to cross-check aspects of the analysis chain. The 5C tree fit suffers from the remaining ambiguity of the bachelor photons not originating from the π^0 decay. This is resolved by choosing the photon with the higher invariant mass when added to the π^0 four-vector, denoted as $\mathrm{IM}(\pi^0\gamma)$, as the bachelor of the ω, which is well-motivated by MC generated signal events, see figure 4.33. The signal hypothesis is ensured by requiring the best fit probability to be larger than 10 %, denoted as `TreeFitProb>0.1`. Figure 4.30 shows that $2\pi^0$ and $\eta\pi^0$ are significantly suppressed by the corresponding anti tree fits, and the signal hypothesis shows a flat probability distribution for the MC signal channel. Assuming a proper detector simulation and kinematic fit procedure, the probability cuts can be optimized to increase the signal-to-background ratio, but the discussed choice is sufficient to extract the result.

After those selection cuts related to kinematic fitting, which at least ensure the proper assignment of photons to the π^0 meson, additional kinematic cuts regarding the η' and ω bachelor photons *not* belonging to the π^0 are employed. The first variant, denoted as `gNonPi0_1`, discards the event if the condition

$$E_\mathrm{k} > 230\,\mathrm{MeV} \cdot \left(1 - \theta/160^\circ\right) \tag{4.29}$$

is not fulfilled for both bachelor photons, where E_k and θ are their reconstructed kinetic energy and polar angle, respectively. Similarly, the second variant `gNonPi0_2` is given by

$$E_\mathrm{k} > \begin{cases} 140\,\mathrm{MeV} & \text{if } \theta < 22^\circ \text{ (TAPS)} \\ 60\,\mathrm{MeV} & \text{otherwise (CB)} \end{cases} \tag{4.30}$$

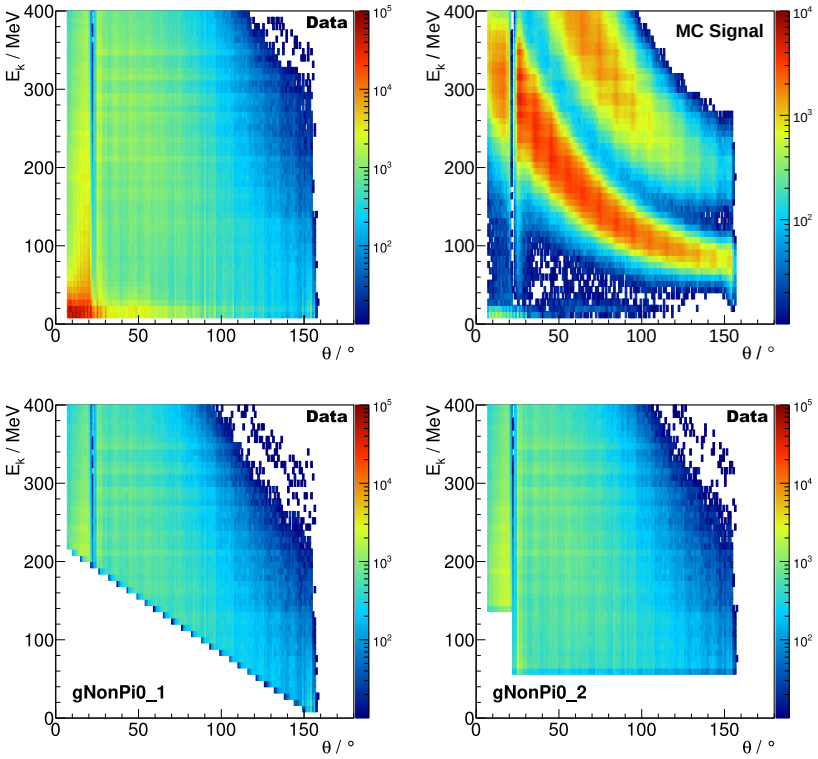

Figure 4.31.: In the top row, the kinetic energy E_k and polar angle θ distribution of the two bachelor photons for prompt-random subtracted data and MC signal $\eta' \to \omega\gamma$ is shown after applying the `AntiPi0/EtaFitProb` and `TreeFitProb` cuts, see text. The bottom row shows the same data histogram after the `gNonPi0_1/2` cuts defined in equations (4.29) and (4.30), as indicated.

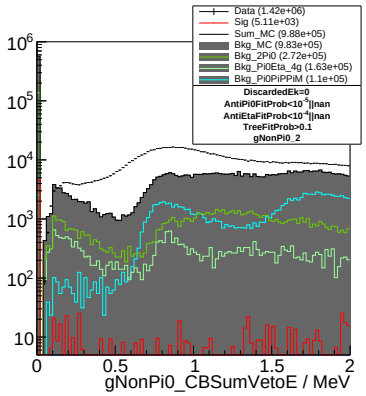

Figure 4.32.: Backgrounds such as $\gamma p \to p\pi^0\pi^+\pi^-$ is reduced by requiring the sum of veto energies of the two bachelor photons, denoted as `gNonPi0_CBSumVetoE`, to be less than 0.2 MeV.

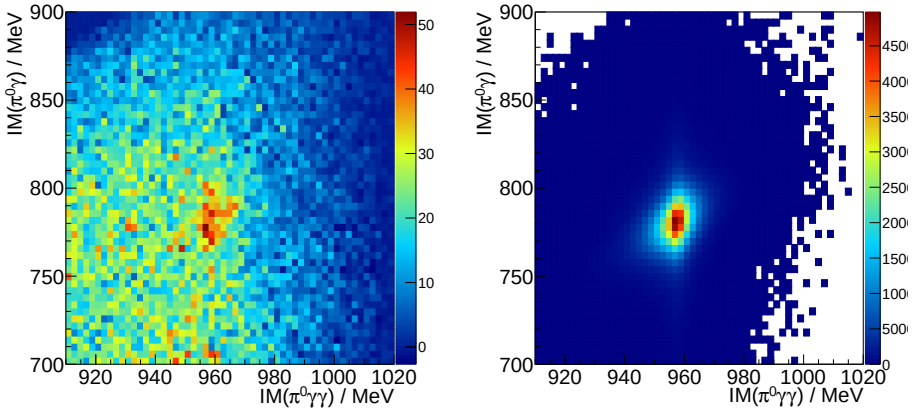

Figure 4.33.: Prompt-random subtracted data is shown on the left, and MC signal on the right. The signal events are visible as a peak around the nominal ω and η' mass values for IM($\pi^0\gamma$) and IM($\pi^0\gamma\gamma$), respectively. Using the 5C tree fit constraining the π^0 only, the bachelor photon of the ω is selected as the one with the *higher* invariant mass combination with the fitted π^0 four-vector, here denoted as IM($\pi^0\gamma$) or `IM_Pi0g[1]`.

ε / %		see
100	Generated events	
45.9	Pre-processing of events	figure 4.27
33.8	`DiscardedEk=0`	section 4.6
33.4	`AntiPi0FitProb<`10^{-5}`||nan`	figure 4.30
30.9	`AntiEtaFitProb<`10^{-4}`||nan`	figure 4.30
28.2	`TreeFitProb>0.1`	figure 4.30
28.0	`gNonPi0_2`	figure 4.31
23.3	`CBSumVetoE_gNonPi0<0.2`	figure 4.32
17.3	`IM_Pi0g[1]`	figure 4.33

Table 4.5.: Overview of the cuts for the extraction of the $\eta' \to \omega\gamma$ signal events, which are applied from top to bottom. In each row, the reconstruction efficiency ε determined from generated MC signal events is given after applying the corresponding cut. See also table 4.4.

where the choice $\theta = 22\,°\mathrm{C}$ is the interface between the calorimeters CB and TAPS, as indicated. Both variants are depicted in figure 4.31 and the second variant representing a looser cut is selected henceforth.

Next, the sum of the matched PID energy information of the two bachelor photons is required to be less than 0.2 MeV, denoted as `CBSumVetoE_gNonPi0<0.2`, which has been cross-checked for the reference channel in figure 4.26. This primarily suppresses the background channel $\gamma p \to \pi^0\pi^+\pi^-$, as shown in figure 4.32. The last cut resolves the bachelor photon ambiguity in case of the 5C signal tree fit. It limits the higher photon invariant mass combination out of the two bachelor photons to be within 40 MeV of the ω rest mass,

$$762.65\,\mathrm{MeV} \leq \mathrm{IM}(\pi^0\gamma) \leq 802.65\,\mathrm{MeV}\,, \tag{4.31}$$

which is denoted as `IM_Pi0g[1]` and depicted in figure 4.33.

All cuts, as given in table 4.5 including their impact on the reconstruction efficiency, are applied to obtain the final spectrum of the invariant mass of all four photons after the 5C kinematic fit constraining the π^0, denoted as $\mathrm{IM}(\pi^0\gamma\gamma)$. Different than the extraction $\eta' \to \gamma\gamma$ events in section 4.6, the fit for the $\eta' \to \omega\gamma$ decay must be carried out on data summed over all EPT channels, since the signal-to-background ratio is not sufficient for a reliable fit in each single channel. In this case, a specific threshold cannot be used similar to equation (4.25) and thus the generalized ARGUS background PDF

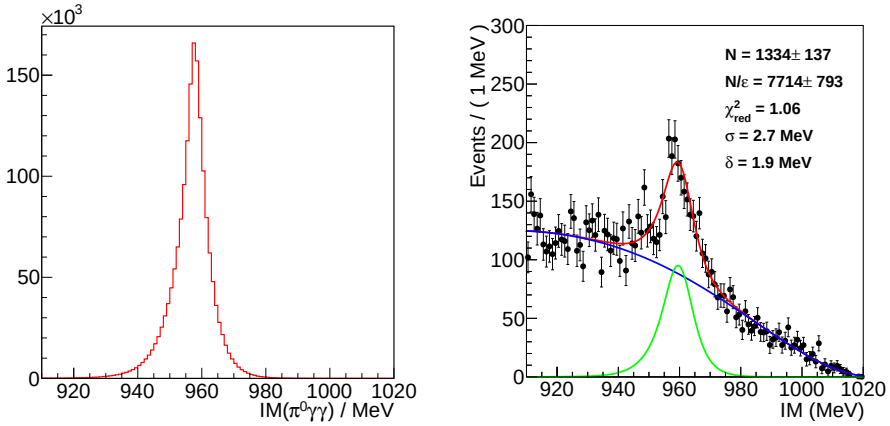

Figure 4.34.: The MC signal shape on the left is fitted to prompt-random subtracted data on the right, which is the sum over all EPT channels. The signal shape is weighted according to figure 4.22 and additionally shifted and Gaussian-smeared with fit parameters δ and σ, respectively. See text and also figure 4.24.

Parameter	Fitted value
N	1334 ± 137
$\delta_{\text{Data-MC}}$	$(1.91 \pm 0.34)\,\text{MeV}$
σ_{smearing}	$(2.74 \pm 0.48)\,\text{MeV}$
N_{bkg}	7940 ± 179
χ_{ARGUS}	-9.91 ± 3.1
p_{ARGUS}	2.37 ± 0.35

Table 4.6.: The fit parameters as determined in figure 4.34, using the MC line shape shifted by δ and smeared by σ with a generalized ARGUS PDF as background. The cut-off parameters x_0 is fixed to 1025 MeV.

Cut	Variations
`DiscardedEk`	$\mathbf{= 0}$, < 20, < 50 MeV
`AntiPi0FitProb`	$< 10^{-7}$, $\mathbf{< 10^{-5}}$, $< 10^{-3}$
`AntiEtaFitProb`	$< 10^{-6}$, $\mathbf{< 10^{-4}}$, $< 10^{-2}$
`TreeFitProb`	> 0.05, $\mathbf{> 0.1}$, > 0.2
`gNonPi0`	Variant 1, **2** and 2 with half the limits in equation (4.30)
`CBSumVetoE_gNonPi0`	$= 0$, < 0.1, $\mathbf{< 0.2}$, < 0.4 MeV
`IM_Pi0g[1]`	Widths 30, **40**, 50 MeV in equation (4.31)

Table 4.7.: The variations of the cut choice in table 4.5, marked bold, are summarized to obtain figure 4.35, yielding in total $4 \cdot 3^6 = 2916$ permutations. See also table 4.4.

with $p \neq 1/2$ in equation (4.24) is used to allow for a more flexible description of the background shape. The final extended likelihood fit, again utilizing a shifted and Gaussian-smeared MC signal line shape, is shown in figure 4.34 and the number of $\eta' \to \omega\gamma$ events in the decay chain (4.27) corrected for reconstruction efficiency reads

$$\#(\eta' \to \omega\gamma) = N(\eta' \to \omega\gamma)/\varepsilon(\eta' \to \omega\gamma) = 7714 \pm 793_{\text{stat}} \,. \tag{4.32}$$

The complete list of fit parameters is given in table 4.6 and the result is discussed further in section 4.8. Similar to the shown main backgrounds, in total 20 photo-production channels have been identified and tested if they contribute significantly to this signal extraction using the MC cocktail. In particular, peaking background contributions such as $\eta' \to \eta\pi^0\pi^0 \to 6\gamma$ have been investigated as well as the interfering decay $\eta' \to \rho^0\gamma \to \pi^0\gamma\gamma \to 4\gamma$. As all those decays are present in the MC with their appropriate branching ratios, it is found that all backgrounds are well under control or can be neglected. This conclusion relies on the correctness of the MC detector simulation and the correct modeling of the generated decays. This assumption is fundamentally challenged by the results presented in section 4.8.

4.8. Results

Combining the findings from sections 4.6 and 4.7, the result according to equation (4.6) for the relative branching fraction reads

$$\text{BR}(\eta' \to \omega\gamma) = (1.82 \pm 0.19_{\text{stat}}) \times 10^{-2} \,, \tag{4.33}$$

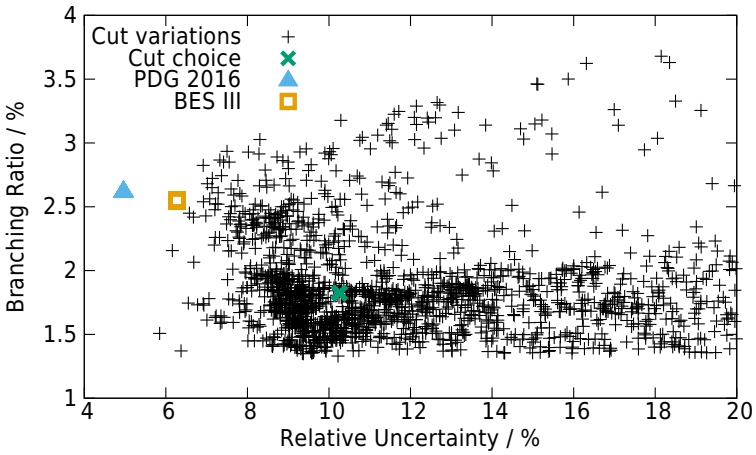

Figure 4.35.: The relative branching ratio $\mathrm{BR}(\eta' \to \omega\gamma)$ is plotted for the cut variations of the signal channel in table 4.7 while the reference analysis is fixed to equation (4.26). The relative uncertainty is solely determined from the fit, see figure 4.34. They are compared to the PDG world average and the BESIII result, the latter plotted with its dominating systematic uncertainty [17, 30]. More detailed figures are given in appendix B.

where the statistical uncertainty is propagated from the fit result in equation (4.32). A lower bound for the systematic uncertainty in equation (4.33) reads 0.092×10^{-2}, which is the statistical uncertainty of the reference channel in equation (4.26), neglecting systematics as given by figure 4.26, and the uncertainties of the branching ratios given in equations (4.7) and (4.28) added in quadrature. The result is about 30 % or $4.3\sigma_{\mathrm{stat}}$ lower than and thus inconsistent with the current world average and the latest measurement, given in equations (1.26) and (1.27), respectively. To investigate this further, the cut choice for the signal analysis is varied according to table 4.7 and the obtained relative branching ratio with its statistical uncertainty is plotted in figure 4.35. It shows that the efficiency correction does not compensate the rather moderate changes in the choice of cuts. As shown in appendix B, no single cut is solely responsible for the wide spread of values, but the cut on the bachelor photon kinematics, `gNonPi0`, and with lesser extent the `DiscardedEk` cut are more strongly partitioning the distribution. Eventually, a conservative estimation of the relative systematic uncertainty is at least 100 %, which is far from rendering the presented result reliable.

Many parts of the analysis have been developed from scratch, such as the clustering algorithm, the kinematic fitter and the calibration routines. To this end, the GEANT4-based detector simulation as provided by the collaboration is a crucial tool to debug and tune the reconstruction process. In particular, the kinematic fitting procedure is sensitive to the correct implementation of the uncertainty model, which is initially determined from single photon detector simulation. It is surprising that investigating the kinematic fit procedure with a comparatively simple $2\pi^0$ analysis, as discussed in section 4.5, requires the introduction of separate uncertainty models for beam-time data and MC input, compare figures 4.17 and 4.18. This either hints at an incorrectly modeled detector simulation or at an error in the kinematic fitter implementation. Both possibilities have been scrutinized, which again relies on MC simulation, and although subtle errors have been found and fixed, some apparently remain unresolved.

Despite those shortcomings, the whole extraction procedure is cross-checked with the MC cocktail instead of data, which contains about one quarter of the total number of η' mesons and uses the branching fractions from [17] as input. The result in this case reads

$$\mathrm{BR}(\eta' \to \omega\gamma) = (3.02 \pm 0.23) \times 10^{-2}\,, \tag{4.34}$$

with statistical and systematical uncertainties added in quadrature, again the systematical contribution should be regarded as a lower bound. Although the backgrounds are typically underestimated in the cocktail and all angular distributions are generated flat, this cross-check shows that the extraction procedure can potentially yield competitive results and is consistent with the input. The slight tendency to higher values is still to be investigated but does not explain the systematically lower values determined on data.

Eventually, using the result from the reliable $\eta' \to \gamma\gamma$ analysis given in equations (4.7) and (4.26), the total number of η' mesons produced in the EPT 2014 beam-time is calculated as

$$\#(\eta') = (5.12 \pm 0.19) \times 10^6\,. \tag{4.35}$$

This number is consistent with the cross-sections published in [127] taking into account the more conservative selection of "good" run files given in table 4.2. Furthermore, the reconstruction efficiency appears to be reasonably well-modeled according to figure 4.26 despite the comparatively large additional MC smearing of cluster energies as explained in section 4.4. This result is encouraging and should be the basis of further work.

Although the treatment of data and MC input within Ant is kept as transparent as possible to analysis algorithm, it is suspected that not the reconstruction

efficiency, as detailed in table 4.5, is the cause for the deviation, but rather yet undiscovered mistake in the reconstruction of beam-time data leading to too small number of signal events N in figure 4.34, somehow not appropriately taken into account by ε. Many event-by-event comparisons, in particular regarding the existing analysis code used in [125, 127], have been carried out and no apparent differences are left uncorrected. However, this statement is speculative and future work should concentrate on obtaining a better understanding of the detector system, including properly simulated energy- and timing measurement resolutions.

5. Conclusion

The A2 collaboration probes the theory of the strong interaction in the low-energy regime using its unique experimental setup for photo-production experiments. Despite tremendous progress in the last decades, many challenging questions remain in this field, for example how an effective description of QCD can consistently be established in the energy regime below 1 GeV, where the conventional perturbative treatment with quarks and gluons as the degrees of freedom fails. This thesis as part of a collaborative effort contributes to this endeavor from an experimental point of view in various aspects. The data acquisition has been improved, future hardware upgrade possibilities have been assessed, a beam-time with unprecedented statistics has been carried out and the $PV\gamma$ decay $\eta' \to \omega\gamma$ has been analyzed. Future work is outlined for each of those contributions in the following.

The detector system as used for the η' production runs in 2014 consists primarily of the CB calorimeter and the photon-tagging device EPT, ideally suited to study the photo-production of η' mesons close to threshold. As the production cross-section off the proton is more than two orders of magnitude lower than the total photo-production cross-section, the data-acquisition must cope with high event rates while the detector system should provide complete coverage of the solid angle in the center-of-mass frame. To this end, the TAPS calorimeter is additionally installed as a forward-wall detector, which coincidentally covers the complete proton polar angle for η' production. The two calorimeters are supplemented by particle identification detectors, but only the barrel scintillator detector PID within CB has proven useful for analysis. As the limiting factor for beam-times before 2013 was the performance and reliability of the data acquisition system, bottlenecks and various shortcomings have been removed within the scope of this thesis. The improvements include the introduction of modern software engineering techniques such as a version control system and a common documentation platform. These improvements have proven crucial for the success of the EPT beam-time in the second half of 2014 by increasing the recorded event rate by a factor of 3 and by enabling rapid error detection during data-taking.

The hardware upgrade feasibility studies focus on the TRB3 multi-purpose FPGA board, as it fulfills all requirements of future A2 experiments. The

applicability of this platform has been successfully shown in test measurements and several conversion front-ends are shown to be suitable for the components of the A2 detector system. The TRB3 collaboration, primarily consisting of future experiments such as PANDA at the GSI in Darmstadt, provides support to overcome the lack of manpower in A2 needed for a major overhaul of the data acquisition system, which should be planned carefully to avoid creating an overly complex system. Within the scope of this thesis, a feature extraction firmware has been developed for the read-out of timing and energy information with sufficient accuracy for the CB detector and front-end electronics for other parts of the detector system have been evaluated. Improvements of the development tool-chain and firmware have been shared among the TRB3 community during this work.

The subsequent analysis of the 2014 EPT beam-time data led to the development of a new analysis framework, of which major parts have been designed and implemented as part of this thesis. During this effort, many technical improvements such as decent calibration and tuning tools have been provided to the A2 collaboration. For example, a new clustering algorithm has been successfully developed, which is a key component to provide calibrations as a service to all collaboration members in the future. The initial goal of a measurement of the relative branching fraction of the $\eta' \to \omega\gamma$ decay, which is competitive with the current world data, has not been achieved. Nevertheless, the new software framework enabled thorough tests of the various analysis components and their systematic influence on the final result. Although an acceptable agreement with already published results of the same dataset using an independent analysis framework has been found for the $\eta' \to \gamma\gamma$ reference channel, the more challenging extraction of $\eta' \to \omega\gamma$ events eventually revealed major shortcomings of the current detector simulation resulting in huge and not fully quantified systematic uncertainties. Despite tremendous effort re-implementing and re-designing analysis concepts to make them generally applicable, those shortcomings could not be resolved. The presented findings serve as a starting point for future analysis efforts.

A. Supplementary figures for $\eta' \to \gamma\gamma$

For each tagger channel corresponding to the given incoming photon energy E_γ, the fit to the signal peak of the reference channel $\eta' \to \gamma\gamma$ is shown in the following. N is the number of signal events, ε the reconstruction efficiency determined from MC, δ the applied shift of the MC line shape in MeV, σ the additional Gaussian detector resolution.

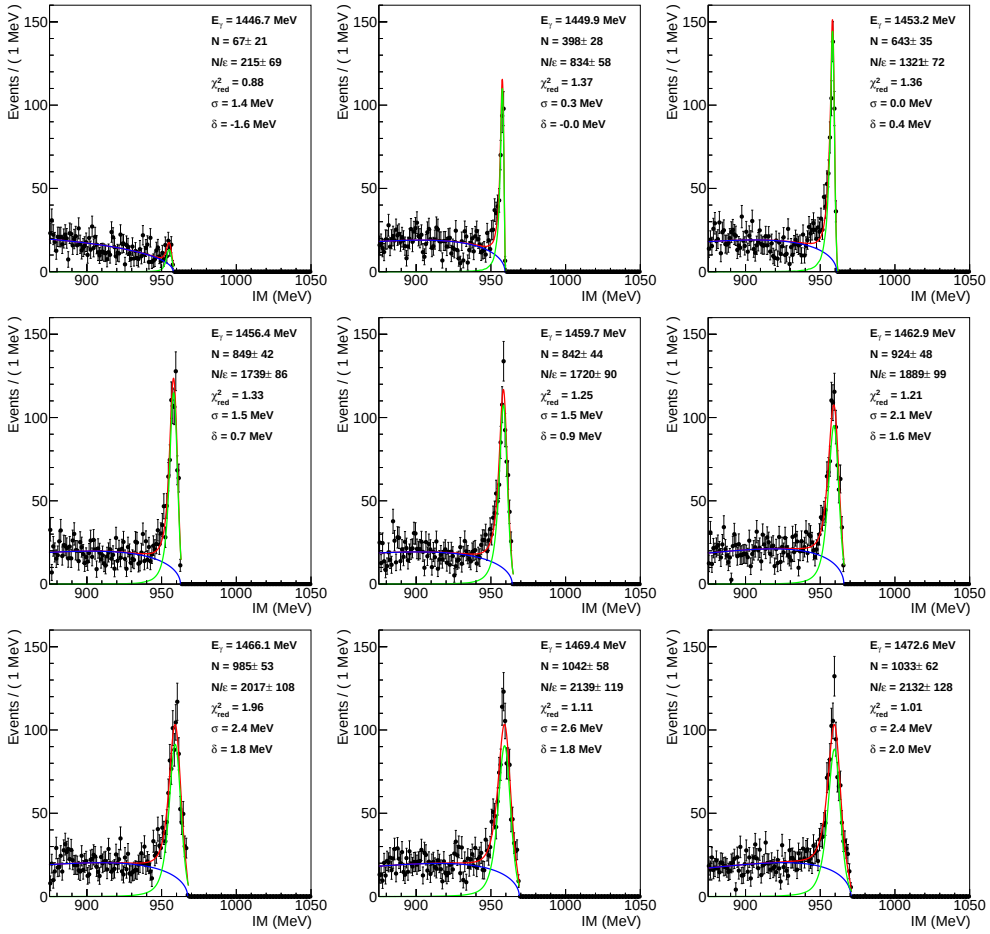

A. Supplementary figures for $\eta' \to \gamma\gamma$

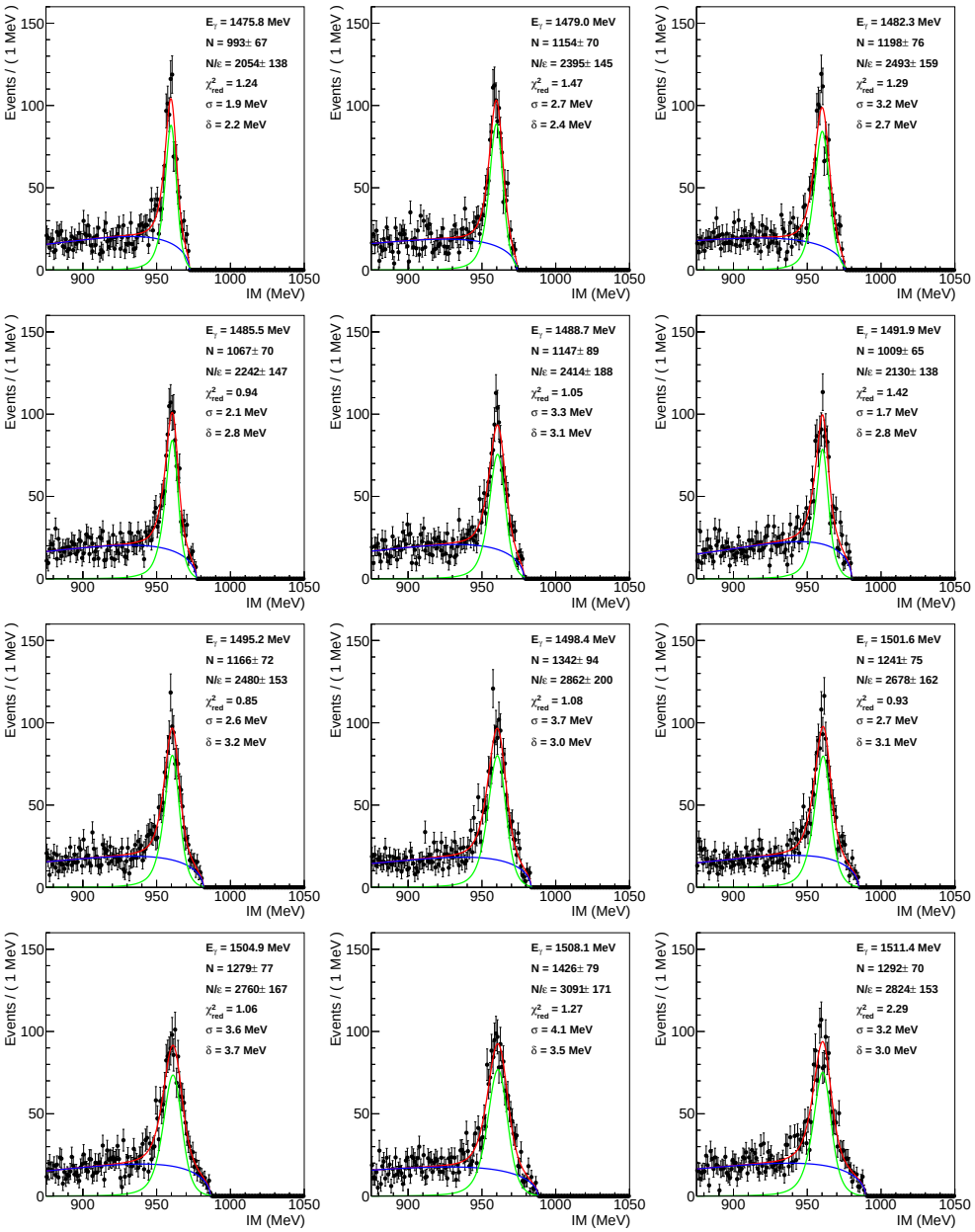

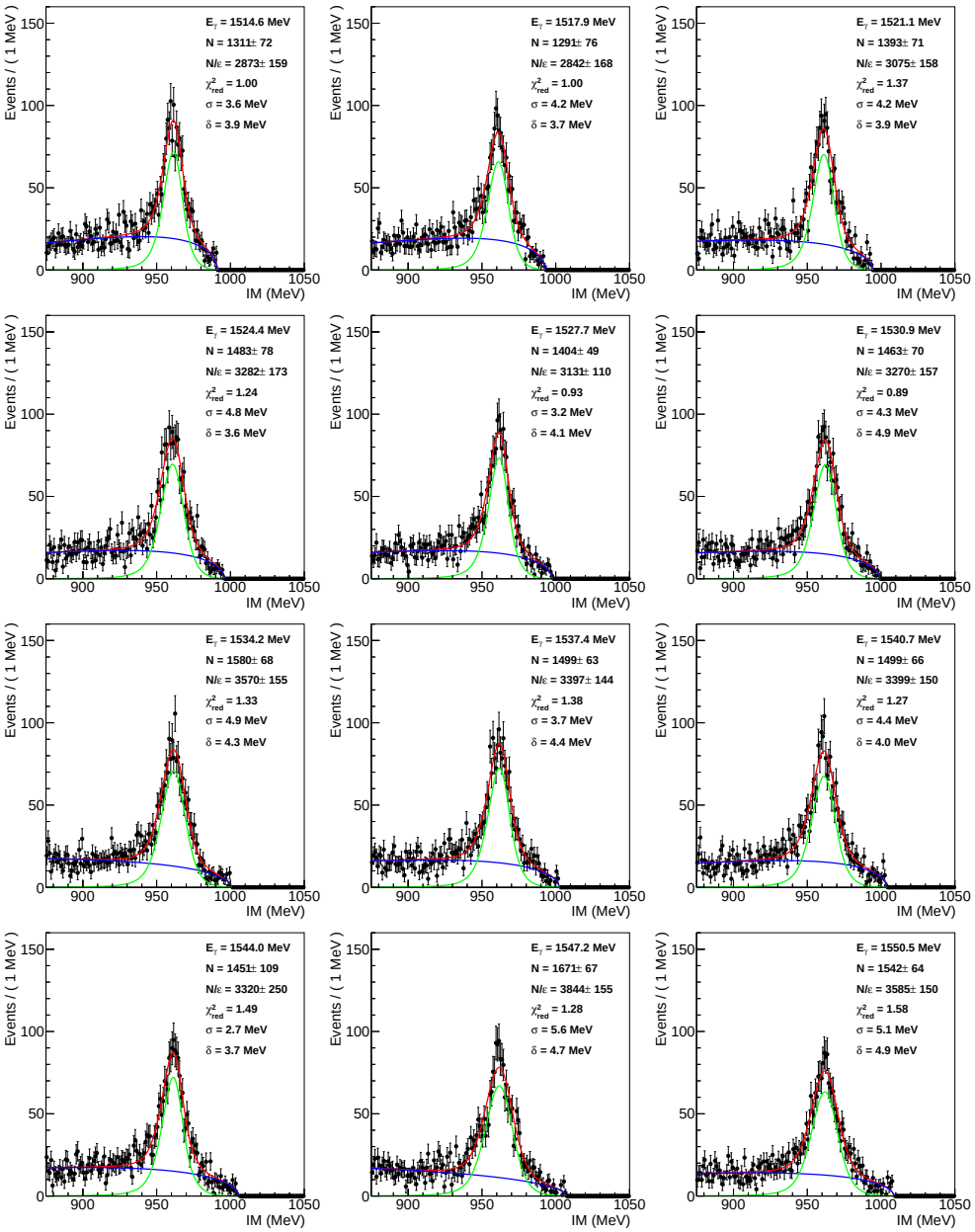
Eγ = 1514.6 MeV
N = 1311± 72
N/ε = 2873± 159
χ²red = 1.00
σ = 3.6 MeV
δ = 3.9 MeV
Eγ = 1517.9 MeV
N = 1291± 76
N/ε = 2842± 168
χ²red = 1.00
σ = 4.2 MeV
δ = 3.7 MeV
Eγ = 1521.1 MeV
N = 1393± 71
N/ε = 3075± 158
χ²red = 1.37
σ = 4.2 MeV
δ = 3.9 MeV
Eγ = 1524.4 MeV
N = 1483± 78
N/ε = 3282± 173
χ²red = 1.24
σ = 4.8 MeV
δ = 3.6 MeV
Eγ = 1527.7 MeV
N = 1404± 49
N/ε = 3131± 110
χ²red = 0.93
σ = 3.2 MeV
δ = 4.1 MeV
Eγ = 1530.9 MeV
N = 1463± 70
N/ε = 3270± 157
χ²red = 0.89
σ = 4.3 MeV
δ = 4.9 MeV
Eγ = 1534.2 MeV
N = 1580± 68
N/ε = 3570± 155
χ²red = 1.33
σ = 4.9 MeV
δ = 4.3 MeV
Eγ = 1537.4 MeV
N = 1499± 63
N/ε = 3397± 144
χ²red = 1.38
σ = 3.7 MeV
δ = 4.4 MeV
Eγ = 1540.7 MeV
N = 1499± 66
N/ε = 3399± 150
χ²red = 1.27
σ = 4.4 MeV
δ = 4.0 MeV
Eγ = 1544.0 MeV
N = 1451± 109
N/ε = 3320± 250
χ²red = 1.49
σ = 2.7 MeV
δ = 3.7 MeV
Eγ = 1547.2 MeV
N = 1671± 67
N/ε = 3844± 155
χ²red = 1.28
σ = 5.6 MeV
δ = 4.7 MeV
Eγ = 1550.5 MeV
N = 1542± 64
N/ε = 3585± 150
χ²red = 1.58
σ = 5.1 MeV
δ = 4.9 MeV
Events / (1 MeV)
IM (MeV)

A. Supplementary figures for $\eta' \to \gamma\gamma$

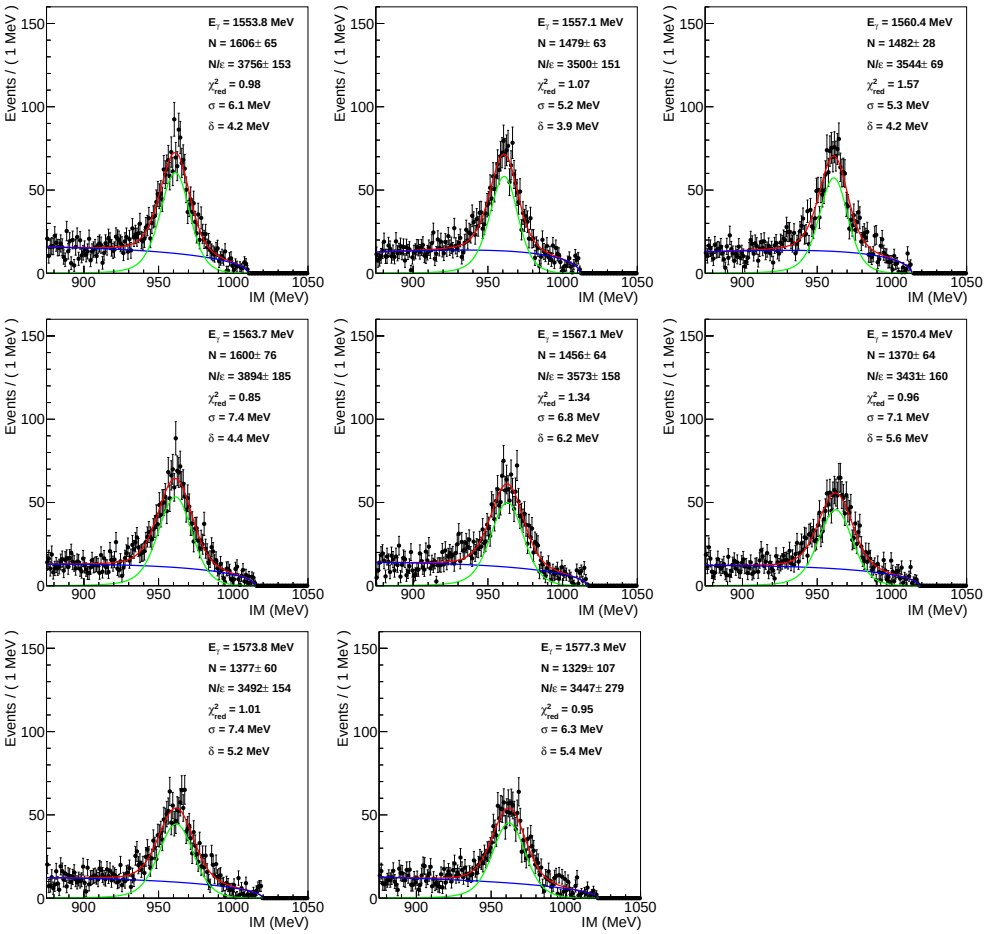

B. Supplementary figures for $\eta' \to \omega\gamma$

Figure 4.35 on page 115 is shown for fixed cuts as specified in the legend, see also table 4.7 on page 114.

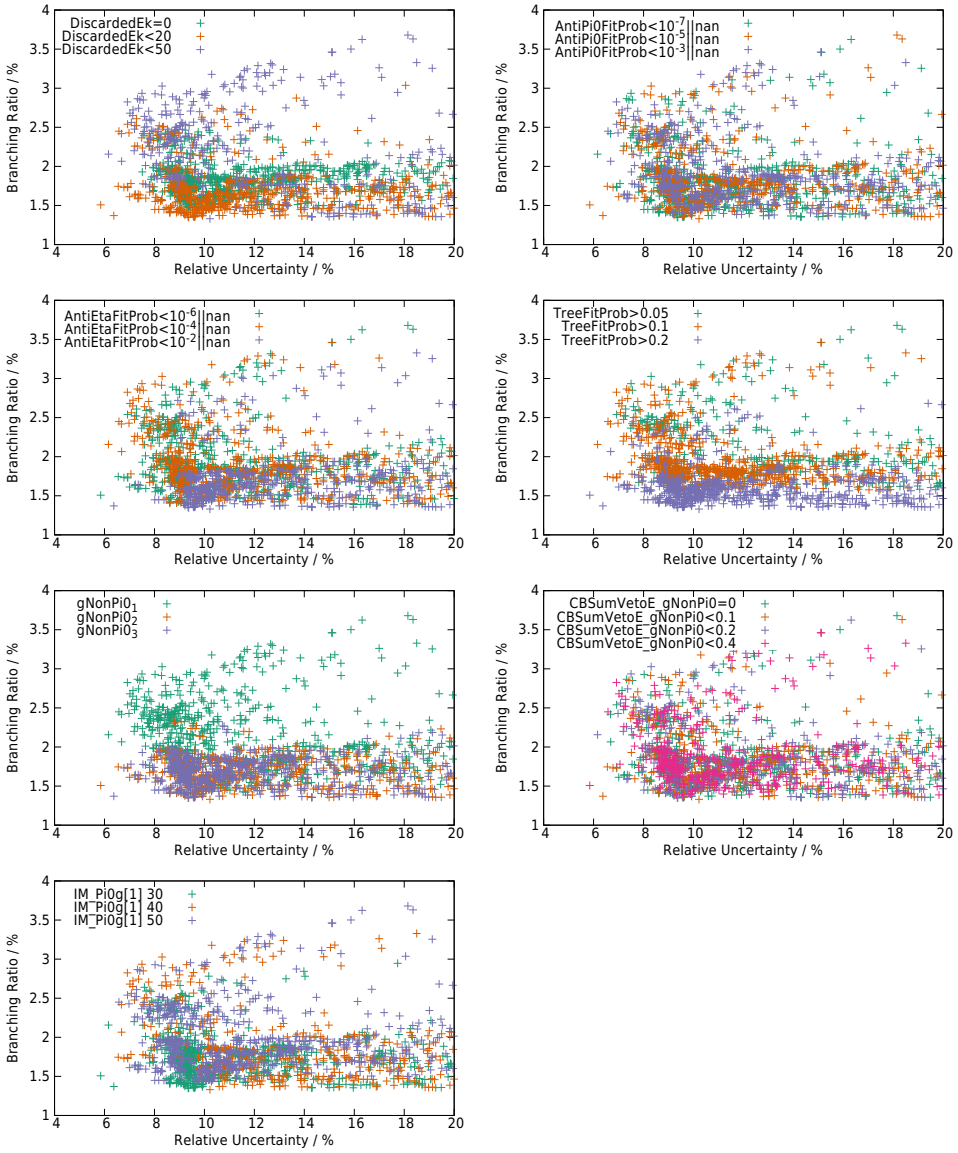

Glossary

PVγ pseudoscalar-vector-gamma.

χEFT chiral effective field theory.

ADC analog-to-digital converter.

API application programming interface.

ASIC Application-Specific Integrated Circuit.

CAMAC Computer Automated Measurement and Control.

CATCH COMPASS Accumulate Transfer and Cache Hardware.

CB Crystal Ball.

CDC clock domain crossing.

CFD constant fraction discriminator.

COMPASS Common Muon Proton Apparatus for Structure and Spectroscopy.

CPLD complex programmable logic device.

CTS Central Trigger System.

DABC Data-Acquisition Backbone Core.

DAQ data acquisition system.

DDR double-data-rate.

DHCP Dynamic Host Configuration Protocol.

ECL Emitter-coupled logic.

EPICS Experimental Physics and Industrial Control System.

EPT end-point tagger.

FEE front-end electronics.

FIFO first-in first-out buffer.

FPGA field-programmable gate array.

GeSiCa GEM Silicon Control and Acquisition.

GSI GSI Helmholtzzentrum für Schwerionenforschung GmbH.

GUI graphical user interface.

HADES high-acceptance dielectron spectrometer.

HDSM harmonic double-sided microtron.

HLD HADES list mode data.

HV high voltage.

IC integrated circuit.

IDE integrated development environment.

IP Internet Protocol.

JTAG Joint Test Action Group.

LN_cChPT large-N_c chiral perturbation theory.

LEC low-energy constant.

LEdD leading-edge discriminator.

LINAC linear accelerator.

LVDS low-voltage differential signal.

MAMI Mainzer Mikrotron.

MC Monte Carlo.

MCP microchannel plate.

MWPC multi-wire proportional chamber.

NIM Nuclear Instrumentation Module.

NTEC New TAPS Electronics Card.

PaDiWa PANDA DIRC WASA.

PANDA anti-proton annihilations at Darmstadt.

PCB printed circuit board.

PCI Peripheral Component Interconnect.

PDF probability density function.

PID particle identification detector.

PLL phase-locked loop.

PMT photomultiplier tube.

PSA pulse shape analysis.

PWM pulse-width modulation.

QCD quantum chromodynamics.

QED quantum electrodynamics.

RMS root mean square.

RPC resistive plate chamber.

RTM race track microtron.

SBC single board computer.

SERDES serializer-deserializer.

SFP small form-factor pluggable transceiver.

SPI Serial Peripheral Interface.

TAPS Two-arm Photon Spectrometer.

TCP Transmission Control Protocol.

TCS trigger control system.

TDC time-to-digital converter.

ToF time-of-flight.

ToT time-over-threshold.

TRB3 TDC readout board revision 3.

UDP Uniform Datagram Protocol.

VHDL VHSIC hardware description language.

VMEbus Versa Module Europa bus.

VUPROM VME Universal Processing Module.

XML extensible markup language.

Bibliography

[1] D. A. Glaser, "Some Effects of Ionizing Radiation on the Formation of Bubbles in Liquids", *Phys. Rev.* 87 (4 August 1952), pages 665–665, DOI: 10.1103/PhysRev.87.665 (cited on page 1).

[2] G. Aad et al., "Observation of a new particle in the search for the Standard Model Higgs boson with the ATLAS detector at the LHC", *Physics Letters B* 716.1 (2012), pages 1–29, ISSN: 0370-2693, DOI: 10.1016/j.physletb.2012.08.020 (cited on page 1).

[3] S. Chatrchyan et al., "Observation of a new boson at a mass of 125 GeV with the CMS experiment at the LHC", *Physics Letters B* 716.1 (2012), pages 30–61, ISSN: 0370-2693, DOI: 10.1016/j.physletb.2012.08.021 (cited on page 1).

[4] J. W. Weil and B. D. McDaniel, "The Production of Protons from Carbon by Monoenergetic Gamma Rays", *Phys. Rev.* 92 (2 October 1953), pages 391–400, DOI: 10.1103/PhysRev.92.391 (cited on page 2).

[5] P. A. M. Dirac, "The Quantum Theory of the Electron", *Proceedings of the Royal Society of London A: Mathematical, Physical and Engineering Sciences* 117.778 (1928), pages 610–624, ISSN: 0950-1207, DOI: 10.1098/rspa.1928.0023 (cited on page 3).

[6] S. Scherer and M. R. Schindler, *A Primer for Chiral Perturbation Theory*, Springer Verlag, 2011 (cited on page 3).

[7] S. Scherer and M. R. Schindler, *A Chiral perturbation theory primer*, 2005 (cited on pages 3, 9, 11).

[8] S. Scherer, "Introduction to chiral perturbation theory", *Adv. Nucl. Phys.* 27 (2003), page 277 (cited on page 3).

[9] A. Neiser, "Effective Field Theories for Vector Particles and Constraint Analysis", Diploma thesis, Universität Mainz, September 2011 (cited on pages 3, 13).

[10] M. Nakahara, *Geometry, topology and physics*, 2. ed., [Reprint.], Graduate student series in physics, Boca Raton [u.a.]: Taylor & Francis, 2003, ISBN: 0750306068 (cited on page 3).

[11] W. J. Marciano and H. Pagels, "Quantum Chromodynamics: A Review", *Phys. Rept.* 36 (1978), page 137, DOI: 10.1016/0370-1573(78)90208-9 (cited on page 6).

[12] G. Altarelli, "Partons in Quantum Chromodynamics", *Phys. Rept.* 81 (1982), page 1, DOI: 10.1016/0370-1573(82)90127-2 (cited on page 6).

[13] D. J. Gross and F. Wilczek, "Asymptotically Free Gauge Theories. I", *Phys. Rev. D* 8 (10 November 1973), pages 3633–3652, DOI: 10.1103/PhysRevD.8.3633 (cited on page 7).

[14] D. J. Gross and F. Wilczek, "Ultraviolet Behavior of Non-Abelian Gauge Theories", *Phys. Rev. Lett.* 30 (26 June 1973), pages 1343–1346, DOI: 10.1103/PhysRevLett.30.1343 (cited on page 7).

[15] K. G. Wilson, "Confinement of quarks", *Phys. Rev. D* 10 (8 October 1974), pages 2445–2459, DOI: 10.1103/PhysRevD.10.2445 (cited on page 8).

[16] M. Creutz, *Quarks, gluons and lattices*, repr., Cambridge monographs on mathematical physics, Cambridge [u.a.]: Cambridge Univ. Press, 1990, ISBN: 0521315352 (cited on page 8).

[17] C. Patrignani et al., "Review of Particle Physics", *Chin. Phys.* C40.10 (2016), page 100001, DOI: 10.1088/1674-1137/40/10/100001 (cited on pages 8, 9, 11–13, 63, 84, 96, 105, 109, 115, 116).

[18] E. Noether, "Invariante Variationsprobleme", *Gött. Nachr.* (1918), pages 235–257 (cited on page 8).

[19] J. Bell and R. Jackiw, "A PCAC puzzle: $\pi_0 \to \gamma\gamma$ in the sigma model", *Nuovo Cim. A* 60 (1969), pages 47–61, DOI: 10.1007/BF02823296 (cited on page 9).

[20] S. L. Adler, "Axial vector vertex in spinor electrodynamics", *Phys. Rev.* 177 (1969), pages 2426–2438, DOI: 10.1103/PhysRev.177.2426 (cited on page 9).

[21] S. L. Adler and W. A. Bardeen, "Absence of higher order corrections in the anomalous axial vector divergence equation", *Phys. Rev.* 182 (1969), pages 1517–1536, DOI: 10.1103/PhysRev.182.1517 (cited on page 9).

[22] S. Weinberg, "Phenomenological Lagrangians", *Physica A* 96 (1979), page 327 (cited on pages 10, 11).

[23] J. Gasser and H. Leutwyler, "Chiral Perturbation Theory to One Loop", *Annals Phys.* 158 (1984), page 142, DOI: 10.1016/0003-4916(84)90242-2 (cited on page 11).

[24] M. C. Birse, "Effective chiral Lagrangians for spin 1 mesons", *Z. Phys. A* 355 (1996), pages 231–246, DOI: 10.1007/s002180050105 (cited on page 11).

[25] R. F. Lebed, "Phenomenology of large N_c QCD", *Czech. J. Phys.* 49 (1999), pages 1273–1306, DOI: 10.1023/A:1022820227262 (cited on page 12).

[26] T. Feldmann, "Quark Structure of Pseudoscalar Mesons", *International Journal of Modern Physics A* 15.02 (2000), pages 159–207, DOI: 10.1142/S0217751X00000082 (cited on page 12).

[27] P. Bickert, "The η-η' system in large-N_c chiral perturbation theory", PhD thesis, Universität Mainz, October 2016 (cited on page 12).

[28] D. Djukanovic, J. Gegelia, and S. Scherer, "Path integral quantization for massive vector bosons", *Int. J. Mod. Phys. A* 25 (2010), pages 3603–3619, DOI: 10.1142/S0217751X10049736 (cited on page 13).

[29] Y.-H. Chen, Z.-H. Guo, and H.-Q. Zheng, "Study of η-η' mixing from radiative decay processes", *Phys. Rev.* D85 (2012), page 054018, DOI: 10.1103/PhysRevD.85.054018 (cited on page 13).

[30] M. Ablikim et al., "Observation of $\eta' \to \omega e^+ e^-$", *Phys. Rev. D* 92 (5 September 2015), page 051101, DOI: 10.1103/PhysRevD.92.051101 (cited on pages 13, 115).

[31] A. Thomas, "Hand-drawn hall overview", February 28, 2012 (cited on page 16).

[32] M. Dehn et al., "The MAMI C accelerator", *The European Physical Journal Special Topics* 198.1 (2011), pages 19–47, ISSN: 1951-6401, DOI: 10.1140/epjst/e2011-01481-4 (cited on pages 15, 17, 18).

[33] A. Jankowiak, "The Mainz Microtron MAMI – Past and future", *The European Physical Journal A - Hadrons and Nuclei* 28.1 (May 2006), pages 149–160, DOI: 10.1140/epja/i2006-09-016-3 (cited on page 17).

[34] L. I. Schiff, "Energy-Angle Distribution of Thin Target Bremsstrahlung", *Phys. Rev.* 83 (2 July 1951), pages 252–253, DOI: 10.1103/PhysRev.83.252 (cited on page 19).

[35] H. W. Koch and J. W. Motz, "Bremsstrahlung Cross-Section Formulas and Related Data", *Rev. Mod. Phys.* 31 (4 October 1959), pages 920–955, DOI: 10.1103/RevModPhys.31.920 (cited on page 19).

[36] S. Schumann, "Strahlungsbegleitete π^0-Photoproduktion am Proton", PhD thesis, Universität Bonn, October 15, 2006 (cited on pages 19, 31).

[37] J. Ahrens, "Physics with Real Photons", Internal A2 manual, July 21, 2015 (cited on pages 19, 20).

[38] T. Mahmoud, "Inbetriebnahme und Test des DAPHNE-Kryo-Targetsystems zur Mes- sung der η-Photoproduktion an flüssigem Helium-3", Diploma thesis, Universität Mainz, September 1999 (cited on page 22).

[39] A. Thomas, "Crystal Ball Hydrogen (Deuterium) Target manual", Internal A2 manual, May 28, 2013 (cited on pages 22, 23).

[40] P.-B. Otte, "Erste Messung der π^0-Photoproduktion an transversal polarisierten Protonen nahe der Schwelle", PhD thesis, Universität Mainz, January 2015 (cited on pages 22, 23, 26, 31, 32, 42).

[41] E. J. Downie, "Radiative π^0 photoproduction in the region of the $\Delta(1232)$ resonance", PhD thesis, University of Glasgow, December 2006 (cited on page 22).

[42] P. P. Martel, "Measuring proton spin polarizabilities with polarized compton scattering", PhD thesis, University of Massachusetts Amherst, February 2013 (cited on page 22).

[43] M. J. Oreglia, "A Study of the Reactions $\Psi' \to \gamma\gamma\Psi$", PhD thesis, Stanford University, December 1980 (cited on page 23).

[44] A. Neiser et al., "Current Status and Performance of the Crystal Ball and TAPS Calorimeter", *Journal of Physics: Conference Series* 587.1 (2015), page 012041 (cited on page 23).

[45] F. Weber, "HV-Kalibrierung des Crystal Balls mit einer ^{241}Am/^{9}Be-Quelle", Bachelor thesis, Universität Mainz, July 15, 2016 (cited on page 26).

[46] J. Wettig, "Aufbau und Inbetriebnahme einer neuen HV-Versorgung für den Crystal Ball Detektor am MAMI", Diploma thesis, Universität Mainz, December 2013 (cited on page 26).

[47] M. Unverzagt, "Energie-Eichung des Crystal Ball-Detektors am MAMI", Diploma thesis, Universität Mainz, October 2004 (cited on page 26).

[48] R. Novotny, "The BaF_2 photon spectrometer TAPS", *IEEE Transactions on Nuclear Science* 38.2 (April 1991), pages 379–385, ISSN: 0018-9499, DOI: 10.1109/23.289329 (cited on page 26).

[49] R. Novotny, "Performance of the BaF2-calorimeter TAPS", *Nuclear Physics B - Proceedings Supplements* 61.3 (1998), Proceedings of the Fifth International Conference on Advanced Technology and Particle Physics, pages 137–142, ISSN: 0920-5632, DOI: 10.1016/S0920-5632(97)00552-5 (cited on page 26).

[50] S. Bender, "Aufbau und Test eines Bleiwolframat-Kalorimeters für das Crystal Ball/TAPS-Experiment an MAMI", Diploma thesis, Universität Mainz, 2009 (cited on page 26).

[51] S. Lugert, "In-Medium Modification of Pion-Pairs on Deuterium", PhD thesis, Universität Gießen, October 2007 (cited on page 26).

[52] P. Martel et al., *The A2 Wiki*, June 2015, URL: https://wwwa2.kph.uni-mainz.de/intern/daqwiki/ (cited on pages 27, 34, 36).

[53] D. Krambrich, "Aufbau des Crystal Ball-Detektorsystems und Untersuchung der Helizitätsasymmetrie in $\gamma p \to p\pi^0\pi^0$", PhD thesis, Universität Mainz, January 2007 (cited on pages 27, 31, 37).

[54] J. Wettig, *Status of the Crystal Ball Detector*, Talk at the CB Collaboration Meeting, March 13, 2014 (cited on page 30).

[55] B. Grube, "The Trigger Control System and the Common GEM and Silicon Readout for the COMPASS Experiment", Diploma thesis, Technische Universität München, December 2001 (cited on page 30).

[56] P. Drexler, "Entwicklung und Aufbau der neuen TAPS-Elektronik", PhD thesis, Universität Gießen, January 2004 (cited on page 32).

[57] P.-B. Otte, *Einsatz von FPGAs in DAQ-Systemen und Triggerlogik am A2-Photonenstrahl*, Talk at the KPH Institute Seminar, 2011 (cited on page 32).

[58] A. Neiser, *A2 VITEC VHDL source code*, 2013, URL: https://github.com/A2-Collaboration/a2vitec (visited on 05/02/2016) (cited on page 33).

[59] J. Michel et al., "The upgraded HADES trigger and data acquisition system", *Journal of Instrumentation* 6.12 (2011), page C12056, DOI: 10.1088/1748-0221/6/12/C12056 (cited on page 38).

[60] G. Korcyl et al., *A Users Guide to the TRB3 and FPGA-TDC Based Platforms*, Automatically generated from version-controlled LaTeX sources,

June 2015, URL: http://jspc29.x-matter.uni-frankfurt.de/docu/trb3docu.pdf (cited on page 40).

[61] A. Neiser et al., "TRB3: a 264 channel high precision TDC platform and its applications", *Journal of Instrumentation* 8.12 (2013), page C12043 (cited on pages 40, 41).

[62] M. Traxler et al., "Applications of the TRB3 and associated front end electronics in recent beam times", in: *Scientific Report 2014*, volume 2015-1, GSI Report, Darmstadt: GSI Helmholtzzentrum für Schwerionenforschung, 2015, 514 p. DOI: 10.15120/GR-2015-1-FG-CS-07 (cited on page 40).

[63] M. Cardinali, "Fast frontend electronics for high rate particle detectors", PhD thesis, Universität Mainz, July 2015 (cited on page 40).

[64] J. Michel, "Development of a Realtime Network Protocol for HADES and FAIR Experiments", Diploma thesis, Universität Frankfurt, August 2008 (cited on page 40).

[65] J. Michel, "Development and Implementation of a New Trigger and Data Acquisition System for the HADES Detector", PhD thesis, Universität Frankfurt, August 2012 (cited on page 40).

[66] J. Michel et al., "In-beam experience with a highly granular DAQ and control network: TrbNet", *Journal of Instrumentation* 8.02 (2013), page C02034 (cited on page 40).

[67] M. Penschuck, "Development and Implementation of a Central Trigger System for TrbNet-based systems", Bachelor thesis, Universität Frankfurt, December 10, 2012 (cited on page 41).

[68] J. Kalisz, "Review of methods for time interval measurements with picosecond resolution", *Metrologia* 41.1 (2004), page 17 (cited on page 41).

[69] C. Ugur, "Multi channel high resolution time-to-digital converter implementation on field programmable gate array", Master thesis, Technische Universität Darmstadt, June 30, 2010 (cited on page 41).

[70] C. Ugur et al., "FPGA based multi-channel TDC development", in: *Scientific Report 2014*, volume 2015-1, GSI Report, psp 1.4.1.5, 1.1.2.4 CBM, PANDA, Darmstadt: GSI Helmholtzzentrum für Schwerionenforschung, 2015, 212 p. DOI: 10.15120/GR-2015-1-MU-NUSTAR-NR-17 (cited on page 41).

[71] J. Adamczewski et al., "Data Acquisition Backbone Core DABC", *IEEE Transactions on Nuclear Science* 55.1 (February 2008), pages 251–255, ISSN: 0018-9499, DOI: 10.1109/TNS.2007.913938 (cited on page 41).

[72] J. Adamczewski-Musch et al., "Data acquisition and online monitoring software for CBM test beams", *Journal of Physics: Conference Series* 396.1 (2012), page 012001 (cited on page 41).

[73] J. Adamczewski-Musch, N. Kurz, and S. Linev, "Developments and applications of DAQ framework DABC v2", *Journal of Physics: Conference Series* 664.8 (2015), page 082027 (cited on page 41).

[74] J. Adamczewski-Musch and S. Linev, *The DABC home page*, 2016, URL: `http://dabc.gsi.de` (visited on 04/20/2016) (cited on page 41).

[75] J. Adamczewski-Musch et al., *The Go4 home page*, 2016, URL: `http://go4.gsi.de` (visited on 04/20/2016) (cited on page 41).

[76] J. Adamczewski-Musch et al., "HADES trbnet data formats for DABC and Go4", in: *Scientific Report 2012*, volume 2013-1, GSI Report, Darmstadt: GSI Helmholtzzentrum für Schwerionenforschung, 2013, 297 p. (Cited on page 42).

[77] M. Traxler et al., *HADES raw data format*, 2006, URL: `https://hades-wiki.gsi.de/cgi-bin/view/DaqSlowControl/HadesRawDataFormat` (visited on 04/20/2016) (cited on page 42).

[78] A. Neiser and M. Hoek, *The Mainz HLD unpacker to ROOT files*, 2013, URL: `https://github.com/neiser/mz-unpacker/` (visited on 04/20/2016) (cited on page 42).

[79] A. Neiser, *GitHub repositories*, 2016, URL: `https://github.com/neiser/` (visited on 04/21/2016) (cited on pages 42, 46).

[80] M. Traxler, J. Michel, et al., *The TRB website*, 2016, URL: `http://trb.gsi.de` (cited on page 42).

[81] M. Traxler, "TRB Developments", Presentation at DIRC 2015 in Gießen, November 13, 2015 (cited on page 44).

[82] C. Ugur, J. Michel, and M. Traxler, "Field-Programmable-Gate-Array Based Signal Discrimination and Time Digitisation", in: *Scientific Report 2012*, volume 2013-1, GSI Report, Darmstadt: GSI Helmholtzzentrum für Schwerionenforschung, 2013, 299 p. (Cited on page 44).

[83] M. Traxler et al., "A Precise Multi-Channel QDC FEE utilizing FPGAs as Discriminators and Delay Elements Based on the TRB3 as TDC and Readout Platform", in: *Scientific Report 2013*, volume 2014-1, GSI Report, Darmstadt: GSI Helmholtzzentrum für Schwerionenforschung, 2014, 13–14 p. DOI: `10.15120/GR-2014-1-NQM-HADES-13` (cited on pages 44–46).

[84] A. Rost, "Optimising the KISS readout concept for calorimeter type detectors", Bachelor thesis, Technische Universität Darmstadt, September 2013 (cited on page 44).

[85] Rodríguez-Ramos, P. et al., "Electromagnetic Calorimeter for HADES Experiment", *EPJ Web of Conferences* 81 (2014), page 06009, DOI: 10.1051/epjconf/20148106009 (cited on pages 44, 46).

[86] P. Horowitz and W. Hill, *The Art of Electronics*, 3rd edition, Cambridge Univ. Press, 2015, ISBN: 978-0-521-80926-9 (cited on page 44).

[87] *LTSpice IV design software homepage*, Linear Technology, 2016, URL: http://www.linear.com/designtools/software/ (visited on 04/22/2016) (cited on page 46).

[88] A. Blanco et al., "TOFtracker: gaseous detector with bidimensional tracking and time-of-flight capabilities", *Journal of Instrumentation* 7.11 (2012), P11012, DOI: 10.1088/1748-0221/7/11/P11012 (cited on page 48).

[89] P. Martins et al., "Towards very high resolution RPC-PET for small animals", *Journal of Instrumentation* 9.10 (2014), page C10012, DOI: 10.1088/1748-0221/9/10/C10012 (cited on page 48).

[90] E. Guliyev et al., "VHDL implementation of feature-extraction algorithm for the PANDA electromagnetic calorimeter", *Nuclear Instruments and Methods in Physics Research Section A: Accelerators, Spectrometers, Detectors and Associated Equipment* 664.1 (2012), pages 22–28, ISSN: 0168-9002, DOI: 10.1016/j.nima.2011.10.016 (cited on page 49).

[91] O. Steffen, "TPC prototype development and measurement of $\omega \to \eta\gamma$ branching fraction", in preparation, PhD thesis, Universität Mainz, 2017 (cited on pages 59, 85, 86).

[92] M. Wolfes, "TPC prototype development and measurement of $3\pi^0$ cross section", in preparation, PhD thesis, Universität Mainz, 2017 (cited on pages 59, 63, 64, 68, 84, 86, 100).

[93] S. Wagner, "Measurement of the Dalitz decay $\eta' \to e^+e^-\gamma$", in preparation, PhD thesis, Universität Mainz, 2018 (cited on pages 59, 78).

[94] J. Wettig, "Measurement of the $\omega \to e^+e^-$ decay", in preparation, PhD thesis, Universität Mainz, 2018 (cited on page 59).

[95] P. Adlarson et al., "Measurement of the $\eta' \to \eta\pi^0\pi^0$ Dalitz decay at the Mainz Microtron" (2017), in preparation (cited on page 59).

[96] S. Wagner, "Studien der Untergrundsituation zum Zerfall $\eta' \to e^+e^-\gamma$ bei A2/MAMI", Master thesis, Universität Mainz, October 2013 (cited on page 60).

[97] R. Owens, "Statistical treatment of tagged photon experiments", *Nuclear Instruments and Methods in Physics Research Section A: Accelerators, Spectrometers, Detectors and Associated Equipment* 288.2 (1990), pages 574–584, ISSN: 0168-9002, DOI: 10.1016/0168-9002(90)90154-X (cited on page 61).

[98] R. Brun and F. Rademakers, "ROOT - An Object Oriented Data Analysis Framework", *Nucl. Inst. & Meth. in Phys. Res. A* 389 (1997), Proceedings AIHENP'96 Workshop, Lausanne, Sep. 1996, pages 81–86 (cited on page 65).

[99] J. Annand et al., *Acqu acquisition and analysis framework*, 2013, URL: https://github.com/A2-Collaboration/acqu (visited on 05/11/2016) (cited on page 65).

[100] L. Torvalds et al., *git – distributed version control system*, 2016, URL: https://git-scm.com/ (visited on 05/11/2016) (cited on page 65).

[101] *cmake – build environment*, Kitware, 2016, URL: https://cmake.org/ (visited on 05/11/2016) (cited on page 65).

[102] *Qt Creator Integrated Development Environment*, The Qt Company, 2016, URL: https://www.qt.io/ide/ (visited on 05/11/2016) (cited on page 65).

[103] S. Lohse, "Vergleichsstudie von Clustering Algorithmen und Untersuchung von HPC Performance Engpässen in der KPH", Diploma thesis, Universität Mainz, August 10, 2015 (cited on pages 66, 70, 73).

[104] D. Werthmüller, "Experimental study of nucleon resonance contributions to η-photoproduction on the neutron", PhD thesis, Universität Basel, 2014 (cited on pages 66, 75, 77, 85, 90).

[105] D. Werthmüller, *CaLib calibration database system*, 2014, URL: https://github.com/werthm/CaLib (visited on 05/11/2016) (cited on page 66).

[106] P. Ott, C. Collicott, P. Martel, et al., *a2GoAT – Generation of Analysis Trees*, 2015, URL: https://github.com/A2-Collaboration-dev/a2GoAT (visited on 05/11/2016) (cited on page 66).

[107] A. Neiser, O. Steffen, M. Wolfes, et al., *Ant – Just another analysis toolkit*, 2015, URL: https://github.com/A2-Collaboration-dev/ant (visited on 05/11/2016) (cited on page 66).

[108] W. G et al., "Best Practices for Scientific Computing", *PLoS Biol* 12 (1 2014), e1001745, DOI: 10.1371/journal.pbio.1001745 (cited on page 66).

[109] A. Neiser and V. Blobel, *APLCON C++11 wrapper*, 2015, DOI: 10.5281/zenodo.51382 (cited on page 67).

[110] A. Neiser and V. Blobel, *APLCON C++11 wrapper – zero-overhead implementation*, 2017, URL: https://github.com/A2-Collaboration-dev/APLCONpp (visited on 04/30/2017) (cited on page 67).

[111] V. Blobel and E. Lohrmann, *Statistische Methoden der Datenanalyse*, Teubner Studienbücher, Teubner, 1998 (cited on pages 67, 92).

[112] D. Glazier, L. Zana, et al., *a2geant detector simulation code*, 2014, URL: https://github.com/A2-Collaboration/a2geant (visited on 05/13/2016) (cited on page 67).

[113] I. Fröhlich et al., "Pluto: A Monte Carlo Simulation Tool for Hadronic Physics", *PoS* ACAT2007 (2007), page 076 (cited on page 67).

[114] W. Lampl et al., *Calorimeter Clustering Algorithms: Description and Performance*, technical report ATL-LARG-PUB-2008-002. ATL-COM-LARG-2008-003, Geneva: CERN, April 2008 (cited on page 69).

[115] R. Müller-Pfefferkorn, "Die Kalibration des elektromagnetischen CsI(Tl)-Kalorimeters des BaBar-Detektors mit Ereignissen der Bhabha-Streuung", PhD thesis, Technische Universität Dresden, November 2001 (cited on page 69).

[116] T. C. Awes et al., "A Simple method of shower localization and identification in laterally segmented calorimeters", *Nucl. Instrum. Meth.* A311 (1992), pages 130–138, DOI: 10.1016/0168-9002(92)90858-2 (cited on page 70).

[117] M. Unverzagt, "Bestimmung des Dalitz-Plot-Parameters α für den Zerfall $\eta \to 3\pi^0$ mit dem Crystal Ball am MAMI", PhD thesis, Universität Mainz, May 26, 2008 (cited on page 75).

[118] W. H. Press et al., *Numerical Recipes: The Art of Scientific Computing*, 3rd edition, New York, NY, USA: Cambridge University Press, 2007, ISBN: 0521880688 (cited on page 80).

[119] M. U. A. Bromba and H. Ziegler, "Application hints for Savitzky-Golay digital smoothing filters", *Analytical Chemistry* 53.11 (1981), pages 1583–1586, DOI: 10.1021/ac00234a011 (cited on page 80).

[120] B. Lemmer, "Measurement of the Excitation Function of ω Photoproduction on Carbon and Niobium", Diploma thesis, Universität Gießen, 2009 (cited on page 85).

[121] M. Pfeiffer, "Photoproduction of η mesons from ^{3}He", PhD thesis, Universität Gießen, November 2002 (cited on page 85).

[122] M. Sobotzik, "Systematische Studien zur π^0 Kalibrierung des Crystal-Ball Detektors", Bachelor thesis, Universität Mainz, May 10, 2017 (cited on page 85).

[123] S. Prakhov, private communication, 2016 (cited on pages 86, 90–92, 100).

[124] V. Hejny, "Photoproduktion von η-Mesonen an Helium 4", PhD thesis, Universität Gießen, 1998 (cited on page 90).

[125] S. Prakhov et al., "Measurement of the slope parameter α for the $\eta \to 3\pi^0$ decay with the Crystal Ball detector at the Mainz Microtron (MAMI-C)", *Phys. Rev. C* 79 (3 March 2009), page 035204, DOI: 10.1103/PhysRevC.79.035204 (cited on pages 90, 92, 117).

[126] P. Adlarson et al., "Measurement of the $\pi^0 \to e^+e^-\gamma$ Dalitz decay at the Mainz Microtron", *Phys. Rev. C* 95 (2 February 2017), page 025202, DOI: 10.1103/PhysRevC.95.025202 (cited on page 90).

[127] V. L. Kashevarov et al., "Study of η and η' Photoproduction at MAMI", *Phys. Rev. Lett.* 118 (21 May 2017), page 212001, DOI: 10.1103/PhysRevLett.118.212001 (cited on pages 90, 99, 100, 116, 117).

[128] L. Demortier and L. Lyons, *Everything you always wanted to know about pulls*, Internal CDF note CDF/ANAL/PUBLIC/5776, version 3.00, April 8, 2008, URL: http://lucdemortier.github.io/assets/papers/cdf5776_pulls.pdf (visited on 04/30/2017) (cited on page 92).

[129] V. Kashevarov, private communication, 2016 (cited on pages 99, 100).

[130] P. Adlarson, private communication, 2016 (cited on page 100).

[131] H. Albrecht et al., "Search for hadronic b→u decays", *Physics Letters B* 241.2 (1990), pages 278–282, ISSN: 0370-2693, DOI: 10.1016/0370-2693(90)91293-K (cited on page 102).

[132] W. Verkerke and D. Kirkby, "The Roofit Toolkit for Data Modeling" (2006), Proceedings of PHYSTAT05, pages 186–189, DOI: 10.1142/9781860948985_0039 (cited on page 102).